Astronomy
&
Astrophysics

The chemical make-up of the Sun: A 2020 vision

M. Asplund[1] , A. M. Amarsi[2] , and N. Grevesse[3,4]

[1] Australian Academy of Science, Box 783, Canberra ACT 2601, Australia
  e-mail: martin.b.asplund@gmail.com
[2] Theoretical Astrophysics, Department of Physics and Astronomy, Uppsala University, Box 516, 751 20 Uppsala, Sweden
[3] Centre Spatial de Liège, Université de Liège, avenue Pré Aily, 4031 Angleur-Liège, Belgium
[4] Space Sciences, Technologies and Astrophysics Research (STAR) Institute, Université de Liège, Allée du 6 août, 17, B5C, 4000 Liège, Belgium

ABSTRACT

Context. The chemical composition of the Sun is a fundamental yardstick in astronomy, relative to which essentially all cosmic objects are referenced. As such, having accurate knowledge of the solar elemental abundances is crucial for an extremely broad range of topics.

Aims. We reassess the solar abundances of all 83 long-lived elements, using highly realistic solar modelling and state-of-the-art spectroscopic analysis techniques coupled with the best available atomic data and observations.

Methods. The basis for our solar spectroscopic analysis is a three-dimensional (3D) radiative-hydrodynamical model of the solar surface convection and atmosphere, which reproduces the full arsenal of key observational diagnostics. New complete and comprehensive 3D spectral line formation calculations taking into account of departures from local thermodynamic equilibrium (non-LTE) are presented for Na, Mg, K, Ca, and Fe using comprehensive model atoms with reliable radiative and collisional data. Our newly derived abundances for C, N, and O are based on a 3D non-LTE analysis of permitted and forbidden atomic lines as well as 3D LTE calculations for a total of 879 molecular transitions of CH, C_2, CO, NH, CN, and OH. Previous 3D-based calculations for another 50 elements are re-evaluated based on updated atomic data, a stringent selection of lines, improved consideration of blends, and new non-LTE calculations available in the literature. For elements where spectroscopic determinations of the quiet Sun are not possible, the recommended solar abundances are revisited based on complementary methods, including helioseismology (He), solar wind data from the Genesis sample return mission (noble gases), sunspot observations (four elements), and measurements of the most primitive meteorites (15 elements).

Results. Our new improved analysis confirms the relatively low solar abundances of C, N, and O obtained in our previous 3D-based studies: $\log \epsilon_C = 8.46 \pm 0.04$, $\log \epsilon_N = 7.83 \pm 0.07$, and $\log \epsilon_O = 8.69 \pm 0.04$. Excellent agreement between all available atomic and molecular indicators is achieved for C and O, but for N the atomic lines imply a lower abundance than for the molecular transitions for unknown reasons. The revised solar abundances for the other elements also typically agree well with our previously recommended values, with only Li, F, Ne, Mg, Cl, Kr, Rb, Rh, Ba, W, Ir, and Pb differing by more than 0.05 dex. The here-advocated present-day photospheric metal mass fraction is only slightly higher than our previous value, mainly due to the revised Ne abundance from Genesis solar wind measurements: $X_{surface} = 0.7438 \pm 0.0054$, $Y_{surface} = 0.2423 \pm 0.0054$, $Z_{surface} = 0.0139 \pm 0.0006$, and $Z_{surface}/X_{surface} = 0.0187 \pm 0.0009$. Overall, the solar abundances agree well with those of CI chondritic meteorites, but we identify a correlation with condensation temperature such that moderately volatile elements are enhanced by ≈ 0.04 dex in the CI chondrites and refractory elements possibly depleted by ≈ 0.02 dex, conflicting with conventional wisdom of the past half-century. Instead, the solar chemical composition more closely resembles that of the fine-grained matrix of CM chondrites with the expected exception of the highly volatile elements.

Conclusions. Updated present-day solar photospheric and proto-solar abundances are presented for 83 elements, including for all long-lived isotopes. The so-called solar modelling problem – a persistent discrepancy between helioseismology and solar interior models constructed with a low solar metallicity similar to that advocated here – remains intact with our revised solar abundances, suggesting shortcomings with the computed opacities and/or treatment of mixing below the convection zone in existing standard solar models. The uncovered trend between the solar and CI chondritic abundances with condensation temperature is not yet understood but is likely imprinted by planet formation, especially since a similar trend of opposite sign is observed between the Sun and solar twins.

Key words. Sun: abundances – Sun: photosphere – Sun: atmosphere – line: formation – meteorites, meteors, meteoroids – Sun: helioseismology

1. Introduction

The pursuit of detailed knowledge of the elemental abundances in the Solar System has played a critical role in the development of modern astronomy. Since the chemical make-up of the planets is not expected to precisely reflect the composition of the nebula from which the Sun and planets formed, there are two methods to determine the proto-solar abundances, both of which were initiated a century ago: solar spectroscopy (Payne 1925; Russell 1929) and mass spectroscopy of primitive meteorites (Goldschmidt 1922, 1938). The two techniques each have their advantages and are thus highly complementary. Indeed a common approach is to combine the meteoritic and photospheric measurements to estimate the Solar System's composition, starting from the early influential works by Unsöld (1948) and Suess & Urey (1956), who provided

a large amount of abundance data for the seminal papers on the origin of the elements by Burbidge et al. (1957) and Cameron (1957). More recently, the widely used literature compilations by Anders & Grevesse (1989), Grevesse et al. (1993), Grevesse & Sauval (1998), Lodders (2003, 2019), Lodders et al. (2009), and Palme et al. (2014) adopted this approach with a preference for the meteoritic values for most elements on account of their typically higher precision[1]. Due to severe depletion of the highly volatile elements – H, He, C, N, O, Ne, Ar, Xe, and Kr – meteorites cannot, however, be relied upon to measure the bulk Solar System composition, for which the Sun is indispensable. There is also no guarantee that the abundances of other elements in the most primitive meteorites, the CI chondrites, truly reflect those of the Sun; indeed, this long-held assumption is not correct, as we show here.

The photospheric abundances are certainly not without shortcomings themselves. While often referred to as observed elemental abundances, the chemical composition of the Sun cannot be directly measured from the observed solar spectrum. Inferring the chemical make-up of a star requires a realistic model for the stellar atmosphere and of the transfer of radiation coupled with all atomic processes that shape the predicted emergent radiation to be compared with the observed spectrum. By necessity, the derived solar (and stellar) abundances are model dependent and therefore are not more reliable than the models from which they are inferred. Traditionally, quantitative solar spectroscopy has been done by means of one-dimensional (1D) model atmospheres: either theoretical models in radiative and convective equilibrium (e.g., Kurucz 1993; Gustafsson et al. 2008) or semi-empirical models in which the atmospheric temperature stratification is deduced from observations of the continuum centre-to-limb variation and of line depths, for example (e.g., Holweger & Müller 1974; Allende Prieto et al. 2001a; Fontenla et al. 2006). Neither type of 1D model attempts to describe the temporal variations or horizontal inhomogeneities in the atmosphere, and as such they include at best only a rudimentary description of convective energy transport (e.g., mixing length theory, Böhm-Vitense 1958).

A huge body of influential and careful work on determining the solar chemical composition has been carried out over several decades using such 1D solar atmosphere models (e.g., Goldberg et al. 1960; Lambert 1968, 1978; Grevesse & Sauval 1973, 1999; Ross & Aller 1976; Holweger et al. 1991; Blackwell et al. 1995). This has often been done in close collaboration with atomic physicists measuring or computing transition probabilities and other necessary input data, which is a highly successful synergy (e.g., Garz et al. 1969; Andersen et al. 1975; Biemont et al. 1981, 1991; Hannaford et al. 1992; Barklem et al. 2000; Lawler et al. 2001, 2013; Johansson et al. 2003; Ljung et al. 2006; Blackwell-Whitehead & Bergemann 2007; Den Hartog et al. 2019). These abundance analyses have mostly been within the framework of local thermodynamic equilibrium (LTE), thus assuming the Boltzmann, Saha, and Guldberg-Waage distributions for the atomic and molecular level populations and the Planck function for the radiation source function (e.g., Rutten 2003). While LTE is for many spectral lines that form in the solar photosphere a reasonable approximation, its validity cannot be taken for granted. For

some elements, departures from LTE for the line formation in 1D model atmospheres (here: 1D non-LTE) and their impact on the inferred solar abundances have been explored (e.g., Steenbock & Holweger 1984; Kiselman 1991; Takeda 1994; Korn et al. 2003; Mashonkina et al. 2011; Lind et al. 2011; Bergemann et al. 2012; Shi et al. 2014). Unfortunately, such statistical equilibrium calculations have still not been performed for the majority of the elements, rendering their solar abundances prone to systematic errors (Asplund 2005; Bergemann et al. 2012; Nissen & Gustafsson 2018).

With increased computational power, it has become possible to perform 3D (magneto-)hydrodynamical simulations of the outer convective and atmospheric layers in the Sun and other stars (e.g., Nordlund & Dravins 1990; Freytag et al. 1996; Ludwig et al. 1999; Asplund et al. 1999; Vögler et al. 2005; Collet et al. 2007; Muthsam et al. 2010; Magic et al. 2013; Trampedach et al. 2013; Beeck et al. 2013). In such modelling, the equations for the conservation of mass, momentum, and energy are solved together with the radiative transfer equation in a 3D simulation box covering a small but representative volume of the star. Besides shedding crucial light on, for example, the nature of convective energy transport (e.g., Stein & Nordlund 1998), the excitation and damping of solar and stellar oscillations (e.g., Sonoi et al. 2015; Zhou et al. 2019), and the dynamo-generation of stellar magnetic fields (e.g., Vögler & Schüssler 2007; Rempel 2014), such 3D simulations are eminently suited as model atmospheres for the prediction of the emergent radiation spectrum and thus for solar abundance analyses (e.g., Kiselman & Nordlund 1995; Asplund et al. 2000c, 2005b; Allende Prieto et al. 2001b; Holweger 2001; Caffau et al. 2008, 2011). Because convection emerges naturally in a self-consistent manner, there is no need to invoke the mixing length theory. These 3D hydrodynamical models are parameter-free in the sense that there is no tuning of any parameters involved to improve agreement with observations, yet their granulation properties, spectral line shapes, continuum centre-to-limb variations, and spectral energy distributions agree extremely well with observations; the choice of, for example, numerical resolution and sub-grid treatment does not impact the predictions (e.g., Asplund et al. 2000a; Nordlund et al. 2009; Pereira et al. 2013). Importantly, this is achieved without invoking any micro- and macro-turbulence parameters since the convective motions and stellar oscillations introduce the necessary Doppler shifts together with the (anti-)correlations in temperature and velocities in granules and intergranular lanes to explain the line strengths, widths, shifts and asymmetries (Asplund et al. 2000b). Clearly, the most recent 3D hydrodynamical solar models, such as the one employed herein, are highly realistic and far superior to any 1D model.

Today it is also feasible to carry out 3D non-LTE line formation calculations with comprehensive model atoms involving the relevant radiative and collisional processes for solar/stellar abundance purposes (e.g., Asplund et al. 2003, 2004; Cayrel et al. 2007; Lind et al. 2013; Steffen et al. 2015; Amarsi et al. 2016a, 2019; Bergemann et al. 2019). Such statistical equilibrium computations, while computationally demanding[2], make optimal use

---

[1] An indication of the incredible impact the solar elemental abundances have across astronomy and beyond is the fact that Anders & Grevesse (1989) is among the ten most cited astronomy articles of all time with more than 8000 citations to date according to ADS, or more than 12 000 citations in Google Scholar.

[2] The 3D non-LTE calculations are dominated by the formal solution of the radiative transfer equation. While in 1D LTE the synthesis of a single spectral line requires radiative transfer solutions along a ray for ~ 100 frequencies and a handful of angles; in 3D non-LTE, this typically has to be done for $\sim 10^4$ frequencies involving all populated atomic levels and transitions, ~ 25 angles, $\sim 10^4$ atmospheric columns, and 20–50 iterations to converge the rate equations for statistical equilibrium and for ~ 5 temporal snapshots, that is, $>10^9$ equivalent 1D LTE calculations.

of the highly realistic 3D hydrodynamical stellar surface convection models and self-consistently describe departures from the LTE within the trace-element assumption. The non-LTE effects can typically be expected to be exacerbated in 3D compared to 1D modelling (Asplund 2005). The field has benefited tremendously from the increased availability of accurate atomic data for the vast number of radiative and collisional cross-sections required, including the previously highly uncertain inelastic collisions with electrons and with neutral hydrogen, which are of paramount importance in the atmospheres of late-type stars (e.g., Barklem 2016a). It is truly remarkable that all free parameters – mixing length parameters, microturbulence, macroturbulence, Unsöld enhancement factor for pressure broadening, Drawin scaling factor for H collisions, etc – which have hampered quantitative stellar spectroscopy for decades, are now finally obsolete. Together with vastly improved stellar modelling and transition probabilities, this has drastically improved the accuracy and precision of the inferred stellar chemical compositions.

Asplund et al. (2009) presented the first fully 3D-based analysis of the solar photospheric elemental abundances with non-LTE calculations (usually based on 1D model atmospheres) for the most important elements; earlier 3D determinations for many elements were reported in for example Asplund et al. (2000c, 2004, 2005a,b). It was also the first time all spectroscopically available elements were analysed in a homogeneous manner and with the systematic uncertainties quantified in detail (see also Scott et al. 2015a,b and Grevesse et al. 2015 for further details).

Here, we discuss further improvements to our solar analysis, including new 3D non-LTE calculations for many more elements, better atomic data, and refined line selection, which have led to a revision of the abundances of numerous elements. We argue that our study represents a state-of-the-art determination of the solar chemical composition, yielding the most reliable results available today. Complemented with precise laboratory measurements of the compositions of the most pristine meteorites (e.g., Palme et al. 2014), the new solar abundances enable us to uncover subtle abundance differences with condensation temperatures of the elements between the Sun and CI chondrites, which reflect the complicated processes of star and planet formation. For convenience, we also provide estimates for the proto-solar (isotopic) abundances where the effects of atomic diffusion, nuclear burning, and radioactive decay have been taken into account, as well as the present-day and proto-solar mass fractions of H, He, and heavy elements.

2. Present-day photospheric solar abundances

Table 1 intercompares the main ingredients of this study and our previous 3D-based solar abundance analyses in terms of 3D solar modelling and spectral line formation, showing that most recent progress has concerned non-LTE calculations, as described further below. The recommended solar photospheric elemental abundances presented in Table 2 and shown in Fig. 1 represent, in our opinion, the most reliable measurements available today, obtained with state-of-the-art analysis techniques and the best atomic and molecular data. All abundances have well-quantified and justified uncertainties and supersede those given in our previous summaries of the solar chemical composition (e.g., Asplund et al. 2005a, 2009).

The abundances are expressed on the traditional astronomical logarithmic abundance scale. Hydrogen is the natural reference element for solar (and stellar) spectroscopy, both because it is the most abundant element and because it provides the continuous opacity in the optical and infrared through the negative
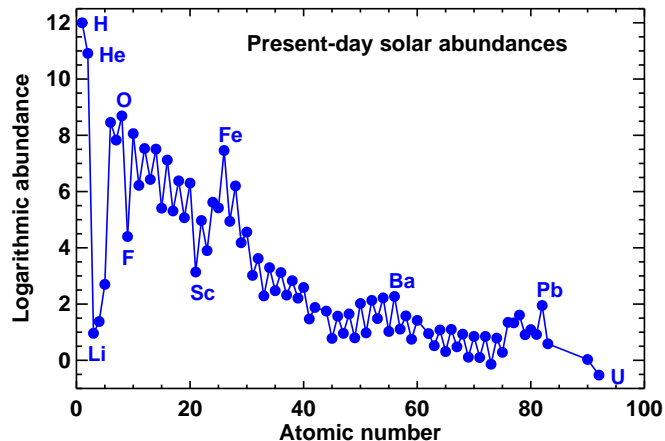

Fig. 1. Present-day solar photospheric logarithmic abundances (by number) as a function of atomic number, with H defined as log $\epsilon_H \equiv 12.00$. For elements for which no photospheric determination has been possible the CI chondritic abundance is shown, corrected for the identified correlation with condensation temperature (Sect. 3.3). H and He are the most abundant elements on account of being produced in the Big Bang with some contribution to He from stellar H-burning. Prominent peaks occur around O, Fe, Ba, and Pb, while elements with an even atomic number have higher abundances than neighbouring odd elements (so-called odd-even effect) as a result of stellar evolution and nuclear physics (minimum nuclear binding energy and nuclei magic numbers). Li, F, and Sc have particularly low abundances relative to nearby elements on account of them being odd elements, having relatively low binding energy, and not being part of the main nucleosynthesis production channels in stars. We note that the unstable elements Tc ($Z = 43$) and Pm ($Z = 61$) are not shown.

hydrogen ion H^-. The normalisation of the elemental number density N_X for an element X is defined as log $\epsilon_X \equiv$ log (N_X/N_H)+ 12.00, for historical reasons, hence log $\epsilon_H \equiv 12.00$[3].

After first summarising some central ingredients in our analysis, in the following sub-sections we present a detailed discussion of the elements for which solar photospheric abundances have been newly analysed, compared with our previous spectroscopic studies of elements heavier than Ne (Scott et al. 2015a,b; Grevesse et al. 2015). In some cases, we simply updated their results in light of new atomic data (in particular, transition probabilities) or improved non-LTE abundance corrections, or we made a different choice in terms of the line list or weighting of the individual lines. For Li, C, N, O, Na, Mg, Al, Si, K, Ca, Fe, and Ba, our results are based on new 3D non-LTE calculations. We also discuss the elements that are not accessible by spectroscopy of the quiet Sun for which other methods to infer the solar abundances are required.

2.1. General considerations of the analysis

Model atmospheres. As a default solar model atmosphere, we employed the same 3D hydrodynamic simulation of the solar surface convection computed with the Stagger code (Nordlund & Galsgaard 1995; Stein & Nordlund 1998; Magic et al. 2013), as was done in our recent studies of 3D

---

[3] This choice was supposedly to avoid having negative elemental abundances for the Sun (Claas 1951; Goldberg et al. 1960). While this is also true for the here recommended solar photospheric abundances – barely, with log $\epsilon_{Th} = 0.03 \pm 0.10$ being the smallest value – several naturally occurring elements indeed have log $\epsilon < 0$ in CI chondritic meteorites (Sect. 3): Ne, Ar, Kr, Xe, Ta, and U.

Table 1. Summary of main ingredients of our 3D-based solar abundance analyses.

Ingredient	Asplund et al. (2005a)	Asplund et al. (2009)	This work
3D model atmosphere:			
Code	Convec	Stagger	Stagger
Code reference	Stein & Nordlund (1998)	Nordlund & Galsgaard (1995)	Magic et al. (2013)
Input abundances	Anders & Grevesse (1989),	Asplund et al. (2005a)	Asplund et al. (2009)
	$\log \epsilon_{He} = 10.92$, $\log \epsilon_{Fe} = 7.50$		
Equation of state	Mihalas et al. (1988)	Trampedach et al. (2013)	Trampedach et al. (2013)
Continuous opacities	Gustafsson et al. (1975)	Gustafsson et al. (2008)	Hayek et al. (2010)
Line opacities	Kurucz (1993)	Gustafsson et al. (2008)	Gustafsson et al. (2008)
Numerical resolution	$200^2 \times 82$	240^3	240^3
Geometrical dimension	$6 \times 6 \times 3.5$ Mm	$6 \times 6 \times 3.5$ Mm	$6 \times 6 \times 3.5$ Mm
Opacity bins	4 (opacity)	12 (opacity & wavelength)	12 (opacity & wavelength)
Effective temperature $T_{eff} \pm$ s.d.	5767 ± 21 K	5778 ± 5 K	5773 ± 16 K
Continuum CLV	too steep $T(\tau)$	good agreement w/obs.	good agreement w/obs.
Spectral line formation:			
Full 3D non-LTE	Li, O	Li, O	Li, C, N, O, Na, Mg, Al, Si, K, Ca, Fe, Ba
3D LTE + 1D/⟨3D⟩ non-LTE	C, N, Na, Mg, Al, K	C, N, Na, Mg, Al, Si, S, K, Ca, Sc, Ti, Cr, Mn, Fe, Co, Cu, Zn, Sr, Ba, Eu, Pb, Th	S, Sc, Ti, Cr, Mn, Co, Cu, Zn, Rb, Sr, Pr, Eu, Pb, Th
3D LTE	Be, B, Si, P, S, Ca, Fe	Be, B, P, V, Ni, $Z \geq 31$	Be, B, P, V, Ni, $Z \geq 31$
1D LTE (literature)	remaining elements	F, Cl, In, Th	F, Cl, In, Th

non-LTE line formation of C, N, and O in the Sun (Amarsi et al. 2018a, 2019, 2020). This is an updated version of the Stagger solar model used in Asplund et al. (2009), Scott et al. (2015a,b), and Grevesse et al. (2015), but the differences in photospheric structure are minor. Detailed 3D radiative transfer with line-blanketing through the opacity binning technique (Nordlund 1982; Collet et al. 2018) is included under the assumption of LTE to compute the necessary radiative heating and cooling rates in the photosphere. The resulting temperature stratification is highly realistic, as is evident from comparisons with the observed continuum centre-to-limb variation (Amarsi et al. 2018a); this was also the case with the 3D model used in Asplund et al. (2009). The predictions of our 3D solar models are in excellent agreement with all key observational diagnostics (e.g., Pereira et al. 2013). The resulting effective temperature of the 24 h simulation sequence is 5773 ± 16 K (standard deviation), indistinguishable from the solar value of 5772 K (Prša et al. 2016). The 3D Stagger models employ an updated version of the so-called MHD (named after the authors) equation of state (Mihalas et al. 1988; Trampedach et al. 2013), continuous and line opacities from the MARCS package (Gustafsson et al. 2008; Hayek et al. 2010), and the solar chemical composition of Asplund et al. (2009). No magnetic fields were included. From the 240^3 simulation grid covering 6 Mm horizontally and 3 Mm vertically, a resampled 3D grid covering the photosphere (1 Mm vertically) was interpolated before the spectral line formation calculations for the abundance determinations to improve the numerical accuracy and to save computational time without sacrificing accuracy; the grid resolutions of both the original and interpolated solar models are sufficient to obtain the correct spectral line broadening from convective motions and oscillations (Asplund et al. 2000a,b; Pereira et al. 2013).

To quantify various systematic uncertainties, we also made use of several 1D model atmospheres: the temporally and spatially averaged 3D model (referred to here as ⟨3D⟩); a 1D hydrostatic ATMO model with mixing length theory convection

and identical equation of state and opacities to the 3D model (Magic et al. 2013, Appendix A); a 1D hydrostatic model computed with the widely used MARCS code (Gustafsson et al. 2008); and the 1D semi-empirical Holweger & Müller (1974) model, which has traditionally been the model of choice for solar abundance analyses for the past half-century.

Spectral line formation. For key atoms and ions, the results are based on 3D non-LTE calculations, using the MPI-parallelised Balder code (Amarsi et al. 2018b), our extensively modified version of Multi3D (Leenaarts & Carlsson 2009). For Li I, C I, N I, Al I, and Si I/Si II, these results were adopted from recently published studies (Wang et al. 2021; Amarsi et al. 2019, 2020; Nordlander & Lind 2017; Amarsi & Asplund 2017), while for O I, Na I, Mg I/Mg II, K I, Ca I/Ca II, and Fe I/Fe II, they are based on new calculations. We also adopted 3D non-LTE literature results for Ba II, which are based on Multi3D calculations (Gallagher et al. 2020).

Balder iteratively solves the 3D (or 1D) radiative transfer equation coupled with the equations for statistical equilibrium (i.e. the atomic level populations fulfil $\partial n_i/\partial t = 0$) under the assumption that the departures from LTE for an element do not feed back onto the atmospheric structure, nor do they impact the line formation of other elements. Balder employs a comprehensive equation of state, background continuum, and line opacities calculated with the Blue code as described in Amarsi et al. (2016b), with the present work adopting the occupation probability formalism to better model line opacities near the series limits (Hubeny et al. 1994). The 3D non-LTE radiative transfer is solved iteratively for typically 5–10 snapshots of the 3D solar model in 26 directions using short characteristics (Ibgui et al. 2013). The number of frequencies for which the radiative transfer equation needs to be computed to adequately resolve the bound-free and bound-bound transitions varies among elements, but for our most complex model atoms (Ca and Fe) it amounts to 20 000 and 45 000, respectively. After convergence, a final

Table 2. Present-day solar photospheric abundances together with those in CI chondrites (Palme et al. 2014), renormalised to the solar Si abundance (Sect. 3).

Z	Element	Photosphere	CI chondrites	Comments	Z	Element	Photosphere	CI chondrites	Comments
1	H	12.00 ± 0.00	8.22 ± 0.04	definition	44	Ru	1.75 ± 0.08	1.77 ± 0.02	
2	He	10.914 ± 0.013	1.29 ± 0.18	helioseismology	45	Rh	0.78 ± 0.11	1.04 ± 0.02	
3	Li	0.96 ± 0.06	3.25 ± 0.04	meteorites	46	Pd	1.57 ± 0.10	1.65 ± 0.02	
4	Be	1.38 ± 0.09	1.32 ± 0.03		47	Ag	0.96 ± 0.10	1.20 ± 0.04	
5	B	2.70 ± 0.20	2.79 ± 0.04		48	Cd		1.71 ± 0.03	meteorites
6	C	8.46 ± 0.04	7.39 ± 0.04		49	In	0.80 ± 0.20	0.76 ± 0.02	
7	N	7.83 ± 0.07	6.26 ± 0.06		50	Sn	2.02 ± 0.10	2.07 ± 0.06	
8	O	8.69 ± 0.04	8.39 ± 0.04		51	Sb		1.01 ± 0.06	meteorites
9	F	4.40 ± 0.25	4.42 ± 0.06		52	Te		2.18 ± 0.03	meteorites
10	Ne	8.06 ± 0.05	-1.12 ± 0.18	solar wind	53	I		1.55 ± 0.08	meteorites
11	Na	6.22 ± 0.03	6.27 ± 0.04		54	Xe	2.22 ± 0.05	-1.95 ± 0.18	nuclear physics
12	Mg	7.55 ± 0.03	7.53 ± 0.02		55	Cs		1.08 ± 0.03	meteorites
13	Al	6.43 ± 0.03	6.43 ± 0.03		56	Ba	2.27 ± 0.05	2.18 ± 0.02	
14	Si	7.51 ± 0.03	7.51 ± 0.01		57	La	1.11 ± 0.04	1.17 ± 0.01	
15	P	5.41 ± 0.03	5.43 ± 0.03		58	Ce	1.58 ± 0.04	1.58 ± 0.01	
16	S	7.12 ± 0.03	7.15 ± 0.02		59	Pr	0.75 ± 0.05	0.76 ± 0.01	
17	Cl	5.31 ± 0.20	5.23 ± 0.06		60	Nd	1.42 ± 0.04	1.45 ± 0.01	
18	Ar	6.38 ± 0.10	-0.50 ± 0.18	solar wind	62	Sm	0.95 ± 0.04	0.94 ± 0.01	
19	K	5.07 ± 0.03	5.08 ± 0.04		63	Eu	0.52 ± 0.04	0.52 ± 0.01	
20	Ca	6.30 ± 0.03	6.29 ± 0.03		64	Gd	1.08 ± 0.04	1.05 ± 0.01	
21	Sc	3.14 ± 0.04	3.04 ± 0.03		65	Tb	0.31 ± 0.10	0.31 ± 0.01	
22	Ti	4.97 ± 0.05	4.90 ± 0.03		66	Dy	1.10 ± 0.04	1.13 ± 0.01	
23	V	3.90 ± 0.08	3.96 ± 0.03		67	Ho	0.48 ± 0.11	0.47 ± 0.01	
24	Cr	5.62 ± 0.04	5.63 ± 0.02		68	Er	0.93 ± 0.05	0.93 ± 0.01	
25	Mn	5.42 ± 0.06	5.47 ± 0.03		69	Tm	0.11 ± 0.04	0.12 ± 0.01	
26	Fe	7.46 ± 0.04	7.46 ± 0.02		70	Yb	0.85 ± 0.11	0.92 ± 0.01	
27	Co	4.94 ± 0.05	4.87 ± 0.02		71	Lu	0.10 ± 0.09	0.09 ± 0.01	
28	Ni	6.20 ± 0.04	6.20 ± 0.03		72	Hf	0.85 ± 0.05	0.71 ± 0.01	
29	Cu	4.18 ± 0.05	4.25 ± 0.06		73	Ta		-0.15 ± 0.04	meteorites
30	Zn	4.56 ± 0.05	4.61 ± 0.02		74	W	0.79 ± 0.11	0.65 ± 0.04	
31	Ga	3.02 ± 0.05	3.07 ± 0.03		75	Re		0.26 ± 0.02	meteorites
32	Ge	3.62 ± 0.10	3.58 ± 0.04		76	Os	1.35 ± 0.12	1.35 ± 0.02	
33	As		2.30 ± 0.04	meteorites	77	Ir		1.32 ± 0.02	meteorites
34	Se		3.34 ± 0.03	meteorites	78	Pt		1.61 ± 0.02	meteorites
35	Br		2.54 ± 0.06	meteorites	79	Au	0.91 ± 0.12	0.81 ± 0.05	
36	Kr	3.12 ± 0.10	-2.27 ± 0.18	solar wind	80	Hg		1.17 ± 0.18	meteorites
37	Rb	2.32 ± 0.08	2.37 ± 0.03		81	Tl	0.92 ± 0.17	0.77 ± 0.05	
38	Sr	2.83 ± 0.06	2.88 ± 0.03		82	Pb	1.95 ± 0.08	2.03 ± 0.03	
39	Y	2.21 ± 0.05	2.15 ± 0.02		83	Bi		0.65 ± 0.04	meteorites
40	Zr	2.59 ± 0.04	2.53 ± 0.02		90	Th	0.03 ± 0.10	0.04 ± 0.03	
41	Nb	1.47 ± 0.06	1.42 ± 0.04		92	U		-0.54 ± 0.03	meteorites
42	Mo	1.88 ± 0.09	1.93 ± 0.04						

Notes. Elements that are commented on are those for which the adopted proto-solar abundances (Sect. 5) are not based on spectroscopy of the solar photosphere; we caution that the differences between solar and CI abundances show a trend with condensation temperature (Sect. 3.3), which should be taken into account when estimating the Solar System composition.

formal solution is carried out for the emergent vertical intensity and for the spectral lines of interest, using a long characteristics solver and higher frequency resolution for accuracy.

Other atomic and ionic lines, as well as all molecular lines, are based on 3D LTE spectrum synthesis using the SCATE code (Hayek et al. 2010), for the most part as presented in our earlier papers (Scott et al. 2015a,b; Grevesse et al. 2015). New 3D LTE calculations were adopted for molecular species of C, N, and O. When no 3D non-LTE calculations had been performed, we relied on our own or published 1D non-LTE abundance corrections, if possible; this procedure is not fully consistent but is expected to be more realistic than the LTE results. Many elements, in particular those beyond the Fe peak, unfortunately still lack non-LTE studies, requiring us to adopt the 3D LTE results. It is emphasised that no micro- and macro-turbulence enter the 3D calculations (Asplund et al. 2000b); for the comparison 1D spectrum syntheses, we assumed a microturbulence of $1\,\mathrm{km\,s^{-1}}$ (e.g., Holweger et al. 1978; Steffen et al. 2013).

Atomic data. The computation of the theoretical solar spectrum hinges critically on the availability of accurate atomic data. We have scoured and carefully assessed the literature and databases for the most up-to-date and most reliable input data required for our solar modelling: transition probabilities, hyperfine splitting, spectral line broadening, partition functions, excitation, ionisation, and dissociation energies, etc (e.g.,

Piskunov et al. 1995; Barklem & Collet 2016; Heiter et al. 2021). In most cases, experimental data have been selected over theoretical data, with the NIST Atomic Spectra Database[4] (Kramida 2019) providing much of the quantitative assessment of the uncertainties in gf-values. For the solar photosphere, the continuous opacities are well determined, except possibly in the UV, and hence they are not a major concern. For the non-LTE calculations, we also made extensive use of the bound-bound and bound-free radiative data from the Opacity Project, the Iron Project, and other dedicated atomic calculations (e.g., Seaton 1987; Hummer et al. 1993; Badnell et al. 2005), as well as theoretical cross-sections for collisions with electrons and with neutral hydrogen (e.g., Bray & Stelbovics 1992, 1995; Zatsarinny 2006; Zatsarinny & Bartschat 2013; Barklem 2016b; Barklem et al. 2017; Belyaev & Yakovleva 2017). Fortunately the situation today in terms of the necessary atomic and molecular data for solar/stellar spectroscopy is significantly improved compared to just a decade ago thanks to the tireless contributions from a relatively small group of atomic physicists to whom we are greatly indebted.

Observations. To derive the solar elemental abundances, the predicted solar spectrum was compared to the observed high-resolution disc-centre intensity spectrum of the quiet Sun with a preference for the Liège (named after its location of production, not observations which were done at Jungfraujoch) visual solar atlas (Delbouille et al. 1973) due to its low degree of contamination of telluric absorption lines. We also made use of other solar atlases for the disc-centre intensity (Neckel 1999; Kurucz 2005), the disc-integrated flux (Kurucz et al. 1984; Kurucz 2006; Reiners et al. 2016), as well as observations in the infrared (Delbouille et al. 1981; Farmer & Norton 1989; Abrams et al. 1996; Hase et al. 2010) as needed and for evaluation purposes; disc-centre intensity spectra are in general preferable to flux to disentangle the contribution of blends. In some cases, we also employ the high-resolution optical centre-to-limb observations of Pereira et al. (2009) and Stenflo (2015) to verify the correctness of our line formation calculations. All of these observed solar spectra have extremely high resolving power (typically equivalent of $R \equiv \lambda/\Delta\lambda > 200,000$) and signal-to-noise (mostly $S/N > 1000$). We either perform a line profile fitting using standard χ^2-techniques or match the observed and computed equivalent widths, depending on the line and possible presence of blends. We allowed our own local continuum placement around the spectral lines in question, as appropriate. Doerr et al. (2016) and Reiners et al. (2016) examined the differences between some of these atlases and overall find excellent agreement; our results are not significantly affected by the particular choice of observations except for a few individual lines.

Uncertainties. Homogenously quantifying the uncertainties of elemental abundances, including systematic errors is almost as important as having accurate determinations of them. Concerning elements for which multiple spectral lines are available for the abundance analysis, we used the weighted standard error of the mean as the statistical uncertainty, the weights being our assessment of the quality of the lines. In cases when only one or two lines can be used, we estimated the statistical error from the goodness of the profile fitting or equivalent width measurement uncertainty.

Following Asplund et al. (2009), we devoted much effort to carefully investigating and evaluating possible systematic

---

[4] https://physics.nist.gov/PhysRefData/ASD/lines_form.html

errors in the analysis, in particular related to the 3D model atmosphere and 3D non-LTE line formation. To quantify the errors from shortcomings in the photosphere temperature structure we take half the differences between the derived abundances from the ⟨3D⟩ model and the Holweger & Müller (1974) model; as noted above, we know from the centre-to-limb variation that the ⟨3D⟩ model is a much closer match to the real Sun (Asplund et al. 2009; Pereira et al. 2013) with newer semi-empirical solar model atmospheres (Grevesse & Sauval 1998; Allende Prieto et al. 2001a) having $50-100$ K lower temperatures than the Holweger & Müller (1974) model in the line-forming region, which is very similar to our 3D model. The impact of atmospheric inhomogeneities is evaluated from taking half the difference between the 3D and ⟨3D⟩ results, which is justified by the close resemblance between the predicted and observed solar granulation patterns. In general, the systematic uncertainty due to non-LTE line formation is estimated as half of the predicted non-LTE abundance correction (3D non-LTE − 3D LTE, or 1D non-LTE − 1D LTE) with a minimum error of 0.03 dex when no non-LTE calculations are available; an exception is made for O for which the non-LTE effects can be accurately quantified using, for example, the centre-to-limb variation of the O I 777 nm triplet and therefore the uncertainties would otherwise be significantly overestimated. These three systematic errors are combined in quadrature with the statistical error to compute the total abundance error.

For some elements, we tried to factor in uncertainties in the input atomic data but in general this has not been attempted due to those often being poorly known and the huge amount of atomic data required for non-LTE modelling. While impossible to know without even more sophisticated solar modelling, we expect our estimated uncertainties to be realistic and possibly conservative overall, although we caution that in a few cases, especially in the absence of any non-LTE calculations, the errors are likely underestimated; in cases where they were particularly striking, we artificially inflated the computed errors somewhat, as noted.

2.2. Light elements: Lithium to beryllium

Li, Be, and B were not analysed in our previous series of papers devoted to the solar chemical composition (Scott et al. 2015a,b; Grevesse et al. 2015) and are therefore discussed explicitly here.

Lithium (Z = 3). In practise, the solar Li abundance can only be determined from the very weak Li I 670.8 nm resonance line, an undertaking that is further complicated by the presence of several blending lines of CN, Fe, and other species. We adopted the recently revised solar Li abundance from Wang et al. (2021), who presented new 3D non-LTE spectral line formation calculations for a wide range of stellar parameters, including for the Sun. Importantly, their more complete treatment of background line opacities in the UV compared with previous studies (e.g., Carlsson et al. 1994; Asplund et al. 2003; Lind et al. 2009, 2013; Harutyunyan et al. 2018; Mott et al. 2020) significantly changes the statistical equilibrium balance of Li I, leading in general to a strengthening of the 670.8 nm line. Using their new 3D non-LTE calculations and allowing for blends, Wang et al. (2021) derived a solar Li abundance of $\log \epsilon_{Li} = 0.96 \pm 0.03$ (statistical) ± 0.05 (systematic) and a 0.09 dex (23%) reduction compared to the advocated value in Asplund et al. (2009).

Beryllium (Z = 4). Following Chmielewski et al. (1975), it was widely believed that Be was depleted by a factor of two in the solar photosphere compared with CI chondrites. This

conclusion was first challenged by Balachandran & Bell (1998) who demonstrated that missing UV opacity (e.g., Bell et al. 2001; Short & Hauschildt 2009) in the stellar models leads to an underestimated solar Be abundance when relying on the Be II 313 nm resonance lines. By calibrating the missing opacity in this wavelength region by enforcing the same O abundance to be estimated from nearby UV OH lines with OH lines in the IR, they found a solar photospheric Be abundance consistent with the meteoritic value. Their conclusion was corroborated in a 3D LTE analysis by Asplund (2004), which we adopted (log ϵ_{Be} = 1.38 ± 0.09; statistical + systematic), suggesting no solar Be depletion. We caution, however, that unaccounted-for blends in this crowded UV region may have biased the inferred Be abundance upwards. Revisiting the topic with 3D non-LTE calculations and a careful assessment of blending lines and continuum placement together with a detailed evaluation of any missing UV opacity would be worthwhile to finally settle the issue, especially given the importance of accurately constraining the amount of mixing below the solar convection zone (Sect. 3.2).

Boron (Z = 5). The solar B abundance can in practice only be inferred from the B I 249.7 nm resonance line, which makes the result quite uncertain due to the heavy crowding and possible missing opacity in this wavelength region. The most recent spectroscopic analysis is that of Cunha & Smith (1999), who inferred log ϵ_B = 2.70 ± 0.20 from a 1D LTE spectrum synthesis, which we have consequently adopted here as the present-day photospheric abundance. While the minority ionisation stage and low excitation potential may suggest that the 249.7 nm line should be susceptible to severe departures from LTE, this does not seem to be the case for the Sun due to a somewhat fortuitous cancellation of non-LTE effects in 1D (Kiselman 1994; Tan et al. 2010). No 3D non-LTE study for B exists to our knowledge.

2.3. Carbon, nitrogen, and oxygen

The fourth, sixth, and third most abundant elements in the Sun by number, C, N, and O are incredibly important to modern astronomy. They also play a central role in the outstanding solar modelling problem (e.g., Basu & Antia 2008; Zhang et al. 2019), wherein a highly significant discrepancy exists pertaining to the interior structure of the Sun as inferred precisely via helioseismic inversions and standard solar models (see Sect. 6). O is the dominant source of opacity at the most problematic region, namely the base of the convection zone, with C and N also providing a non-negligible contribution there. It has been noted that higher C, N, and (especially) O abundances by ≈0.15 dex would alleviate the discrepancy with the sound speed (e.g., Pinsonneault & Delahaye 2009), but this would not address all observational constraints (Buldgen et al. 2019b). Adding to the controversy, all three elements form volatile compounds and are thus depleted in meteorites; their abundances must be inferred through spectroscopy of the solar photosphere.

Parallel to our work, the CO^{5}BOLD group have led a commendable effort to measure the solar C, N, and O abundances from atomic lines, similarly employing 3D hydrodynamic model atmospheres (Caffau et al. 2008, 2009, 2010, 2013, 2015; Steffen et al. 2015); they have not yet explored the molecular lines. These studies tend to find slightly higher C, N, and O abundances by 0.03–0.07 dex that usually agree within the uncertainties (Caffau et al. 2011). These differences most likely do not originate in the 3D models or radiative transfer codes themselves, but rather can be traced to our more conservative choice of unblended lines, the adopted oscillator strengths, and the measured equivalent widths, as has been demonstrated for C (Amarsi et al. 2019) and N (Amarsi et al. 2020); moreover, unpublished calculations have similarly indicated good agreement for the O I 777 nm triplet when adopting exactly the same input data.

After submission of our article, we became aware of new 3D non-LTE line formation calculations of the O I 777 nm triplet and [O I] 630 nm forbidden line by Bergemann et al. (2021) using 3D solar models computed with the Stagger and Bifrost codes, the latter with and without a chromosphere. Their results agree perfectly with those presented here and in Asplund et al. (2009): log $\epsilon_{OI\,777}$ = 8.70 ± 0.05 and log $\epsilon_{[OI]\,630}$ = 8.71 ± 0.03, further supporting a low solar O abundance. Reassuringly, they find only a very minor effect (≈0.01 dex) of a chromospheric temperature rise on these lines.

An extension to using a 1D semi-empirical model atmosphere has recently been presented by Cubas Armas et al. (2017, 2020), who derived a 3D solar model from the spectral inversion of three spatially resolved Fe I lines. They applied it to the [O I] 630.0 nm line in the Sun to infer log ϵ_O = 8.80 ± 0.03. While this is an interesting approach well worth pursuing further, we consider it premature to adopt their derived abundance until this empirical 3D solar model has been exposed to a variety of observational tests, which our theoretical 3D hydrodynamical models have successfully passed (Nordlund et al. 2009; Pereira et al. 2013). In particular, it is not clear whether their model has the appropriate T_{eff} since it is neither an imposed constraint of the spectral inversion of the normalised line profiles, nor is it tested for afterwards. It remains to be seen whether consistent O abundances would be obtained from the [O I], O I, and OH lines.

Table 3 shows the results of our reanalysis of all the available indicators of C, N, and O using our most recent 3D model atmosphere and the most up-to-date atomic and molecular data. The atomic results are based on recent 3D non-LTE studies for C (Amarsi et al. 2019), N (Amarsi et al. 2020), and O (Amarsi et al. 2018a); in the latter case, the calculations were extended to include the other available atomic indicators (see also Amarsi 2016). The molecular results come from a new homogeneous analysis of 879 different lines, with the background C, N, and O abundances iterated to consistency (Amarsi et al. 2021). Compared to Asplund et al. (2009), the new recommended abundances are identical for N and O and only 0.03 dex higher for C.

Carbon (Z = 6). Of the three elements considered in this section, C has the largest number of available indicators (Table 3) and is arguably the best constrained. The [C I] result is drawn from the 3D non-LTE analysis of the 872.7 nm line from Amarsi et al. (2019), although we note that this low-excitation line is well-reproduced in 3D LTE. The C I result is based on the 14 lines also analysed in this 3D non-LTE study; here, the result has increased by 0.03 dex in light of new gf-values from large-scale atomic structure calculations by Li et al. (2021). The molecular results are based on new 3D LTE calculations of 39 lines in the C$_2$ Swan system, and CH lines which were divided into 51 fundamental rovibrational (dv = 1) lines and seven electronic lines in the CH A-X system. CO lines were also considered by adopting the O abundance inferred from OH lines for a particular model atmosphere and including the error in this O abundance in the total error budget. The CO lines were divided into two groups of rovibrational transitions, including 28 belonging to fundamental (dv = 1) bands and 52 to first overtone (dv = 2) bands.

The advocated solar C abundance is 8.46 ± 0.04. This was evaluated as the weighted mean and error of the [C I], C I, C$_2$, CH, and CO results given in Table 3; to avoid giving

Table 3. C, N, and O abundances in the solar photosphere as inferred from the available indicators and from different model atmospheres, with the combined statistical and systematic uncertainties in the final column.

Indicator	Non-LTE				LTE				Error
	3D	⟨3D⟩	MARCS	HM	3D	⟨3D⟩	MARCS	HM	
[C I]	8.453	8.424	8.421	8.432	8.453	8.424	8.421	8.432	0.034
C I	8.470	8.459	8.456	8.488	8.480	8.467	8.462	8.497	0.038
C_2 Swan	–	–	–	–	8.455	8.473	8.433	8.520	0.029
CH (A-X)	–	–	–	–	8.459	8.471	8.393	8.555	0.048
CH ($dv = 1$)	–	–	–	–	8.470	8.503	8.438	8.573	0.043
CO ($dv = 1$)	–	–	–	–	8.487	8.653	8.606	8.683	0.101
CO ($dv = 2$)	–	–	–	–	8.467	8.681	8.609	8.743	0.122
N I	7.767	7.816	7.804	7.864	7.780	7.828	7.813	7.879	0.035
NH ($dv = 0$)	–	–	–	–	7.881	8.032	8.021	8.079	0.087
NH ($dv = 1$)	–	–	–	–	7.921	7.988	7.914	8.056	0.050
CN (0–0)	–	–	–	–	7.867	7.964	7.927	8.016	0.072
CN ($dv \geq 1$)	–	–	–	–	7.899	7.994	7.959	8.046	0.078
[O I]	8.703	8.688	8.664	8.705	8.703	8.688	8.664	8.705	0.051
O I	8.686	8.682	8.657	8.678	8.805	8.779	8.732	8.789	0.030
OH ($dv = 0$)	–	–	–	–	8.690	8.792	8.782	8.837	0.070
OH ($dv = 1$)	–	–	–	–	8.707	8.800	8.728	8.884	0.063
OH ($dv = 2$)	–	–	–	–	8.690	8.756	8.673	8.848	0.087

these species too much weight, the rovibrational and electronic results for CH were first combined into a weighted mean (8.46), as were the fundamental and first overtone results for CO (8.48). The final result is a 0.03 dex increase over those stated in Asplund et al. (2009). Nevertheless, the agreement between the different indicators found here is excellent, and noticeably improved over that earlier study. The reason for the new, slightly higher value can primarily be attributed to improvements to the atomic and molecular input data ([C I] Froese Fischer 2006; C I Li et al. 2021; C_2 Brooke et al. 2013; CH Masseron et al. 2014; CO Li et al. 2015), as well as to the employed molecular dissociation constants (Barklem & Collet 2016).

Nitrogen (Z = 7). Compared to C, there are relatively few good indicators of the solar N abundance. There are no [N I] lines visible in the solar spectrum, and only five N I lines were identified as being sufficiently strong and unblended to be measured with confidence (Amarsi et al. 2020). The 3D non-LTE atomic result is combined with new 3D LTE results for molecular lines (Table 3). This includes NH rovibrational lines that were divided into two groups consisting of 13 pure rotational ($dv = 0$) and 15 fundamental ($dv = 1$) lines. CN lines were also considered by adopting weighted mean carbon abundances as inferred from C_2, CH, and CO and for the different model atmospheres, and including the error in this C abundance in the total error budget. The CN lines were separated into two groups consisting of 59 electronic lines in the 0−0 band, which typically has the best data, and 463 more lines with $dv \geq 1$ in various bands.

Table 3 shows a discrepancy of 0.13 dex between the atomic N I result (7.77), and the weighted mean (7.90) of the mean NH (7.91) and CN (7.88) results. We can only speculate on where the inconsistency arises. The N I oscillator strengths were taken from Tachiev & Froese Fischer (2002) and are expected to be reliable at the 0.03 dex level based on rankings from NIST (and verified with separate calculations as discussed in Sect. 2.1 of Amarsi et al. 2020). The oscillator strengths used here for NH and CN were taken from Brooke et al. (2014a,b, 2015), however it is difficult to imagine both sets of calculations having systematic offsets of 0.1 dex. Moreover, the dissociation energies of CN

and NH are now well established (Barklem & Collet 2016) and thus unlikely to be the reason behind the high molecular-based N abundance. We note that this discrepancy was already present in Asplund et al. (2009), albeit to a lesser degree, with the calculations there based on an unpublished set of older molecular data (A.J. Sauval, priv. comm.).

The advocated solar N abundance is 7.83 ± 0.07. Owing to the atomic versus molecular discrepancy, this was found by taking the unweighted mean of the atomic result together with the weighted mean of the molecular results. The uncertainty is given by the standard error in the mean (or equivalently, half the range between the two values). The value is unchanged from that of Asplund et al. (2009); however, the stipulated uncertainty is 0.02 dex larger.

Oxygen (Z = 8). The solar O abundance can be inferred from a number of different atomic and molecular indicators (Table 3). For the atomic indicators, we carried out a spectral line fitting analysis of the [O I] 557.7 nm, 630.0 nm, and 636.4 nm lines, and of the O I 615.8 nm, 777 nm, 844.7 nm, and 926.9 nm lines, using the 3D non-LTE model of Amarsi et al. (2018a). The fitting method follows that presented in Amarsi (2016, Chapter 4). Here, the strengths of the CN and C_2 blending lines were fixed by adopting the line lists and abundances of the earlier C and N analyses and the strength of the blending Ni I 630 nm line calculated using the gf-value from Johansson et al. (2003) and the Ni abundance inferred here (log ϵ_{Ni} = 6.20; Sect. 2.5). Ultimately, for [O I] nearly all weight was given to the 630.0 nm line after considering the relative difficulties in modelling the respective continua and blending contributions. Similarly for O I, most weight was given to the 777 nm triplet, because available centre-to-limb observations (Pereira et al. 2009) allow us to correct for and constrain errors in the cross-sections for inelastic collisions with neutral hydrogen (following Amarsi et al. 2018a). The molecular results are based on new 3D LTE calculations of OH rovibrational lines, which were divided into three groups consisting of 84 pure rotational ($dv = 0$), 50 fundamental ($dv = 1$), and 15 first overtone ($dv = 2$) lines, all giving highly consistent results.

The advocated solar O abundance is 8.69 ± 0.04. Our new value was determined from the weighted mean and error of the [O I], O I, and OH results given in Table 3, albeit first combining the three rovibrational OH results into a single weighted mean (8.70). An alternative value is obtained by taking the unweighted mean, either of these three species, or of all five indicators in Table 3. This would put less weight on the strong O I 777 nm triplet, but with both approaches the value is increased by less than 0.005 dex, since there is excellent agreement between the different indicators. Our recommended solar O abundance is unchanged from Asplund et al. (2009); however, the stipulated uncertainty is 0.01 dex smaller.

Combined with our revised C abundance, the solar C/O ratio is 0.59 ± 0.08, a value which has steadily increased over the last few decades (e.g., 0.43: Anders & Grevesse 1989; 0.48; Grevesse et al. 1991; 0.49: Grevesse & Sauval 1998; 0.50: Allende Prieto et al. 2001b, 2002; 0.54: Asplund et al. 2004, 2005b; 0.55: Asplund et al. 2009; Caffau et al. 2011; 0.56: Amarsi et al. 2018a, 2019). The Sun has a higher C/O ratio than most solar twins regardless of age (Bedell et al. 2018), which could be a result of the Sun having migrated radially outwards by 2−3 kpc in the Milky Way disc since birth (Nieva & Przybilla 2012).

2.4. Intermediate-mass elements: Sodium to calcium

Sodium (Z = 11). The solar Na abundances presented in Asplund et al. (2009) and Scott et al. (2015b) were based on a 3D LTE analysis corrected for non-LTE effects using 1D model atmospheres (Lind et al. 2011). Here, we present the first full 3D non-LTE calculations for Na in the Sun, employing the same 23-level Na model atom as in Lind et al. (2011), which importantly contains a full quantum mechanical description for inelastic Na I+H I collisions (Belyaev et al. 2010; Barklem et al. 2010). Experiments suggest these are sufficiently realistic for non-LTE modelling (Barklem et al. 2021).

A summary of the inferred abundances for the different lines using a variety of model atmospheres is provided in Table A.1. We employed the same five weak Na I lines as well as transition data as in Scott et al. (2015b); the equivalent widths were corrected for minor contributions from blending lines. The 3D non-LTE effects are minor (≈ -0.03 dex) and very similar to those previously determined in 1D. Our recommended 3D non-LTE Na abundance, based on the unweighted mean of the five Na I lines, becomes $\log \epsilon_{Na} = 6.22 \pm 0.01$ (statistical) ±0.03 (systematic), which is 0.01 dex larger than the value provided in Scott et al. (2015b).

Magnesium (Z = 12). Scott et al. (2015b) determined the solar photospheric Mg abundance based on 3D LTE line formation calculations coupled with non-LTE abundance corrections computed with different 1D model atmospheres. Their value, $\log \epsilon_{Mg} = 7.59 \pm 0.04$, was only 0.01 dex lower than the recommended abundance by Asplund et al. (2009). The Mg I and Mg II lines yielded fully consistent abundances in non-LTE, but they were significantly less so in LTE, highlighting the need for statistical equilibrium calculations for Mg II (non-LTE corrections are vanishingly small for Mg I for the Sun). Osorio et al. (2015) and Bergemann et al. (2017) carried out new 1D non-LTE calculations based on improved atomic data, but since their analyses were more focussed on other stars they have only very few lines in common with Scott et al. (2015b), most of their lines being much stronger in the Sun and less suitable for abundance purposes.

For the first time, we carried out full 3D non-LTE calculations of Mg in the solar photosphere. Our new atomic model consists of 48 Mg I levels, 27 Mg II levels, and the Mg III ground state; and 482 bound-bound and 71 bound-free radiative transitions, drawing on new experimental and theoretical transition probabilities for Mg I (Pehlivan Rhodin et al. 2017b). We made use of realistic cross-sections for inelastic collisions with electrons from Barklem et al. (2017) for Mg I and from Liang et al. (2009) for Mg II, and we used rate coefficients from Barklem et al. (2012) and Barklem (2016b) to describe inelastic collisions between Mg I and neutral hydrogen.

A summary of the inferred abundances for the different lines using a variety of model atmospheres is provided in Table A.1. The unweighted mean of eight Mg I lines gives $\log \epsilon_{Mg} = 7.56 \pm 0.01$ (statistical) in 3D non-LTE. The systematic uncertainty as estimated from the 3D LTE, ⟨3D⟩, and HM models is less than 0.01 dex as these all give highly consistent results for our Mg I lines. In 3D LTE, our Mg I result is 0.04 dex smaller than that given in Scott et al. (2015b) with the new gf-values only having a minor effect (−0.01 dex). Instead, the difference stems mainly from how pressure broadening was treated; here, we used ABO theory (Anstee & O'Mara 1995; Barklem & O'Mara 1997; Barklem et al. 1998), adopting new and extended tables (P. S. Barklem, priv. comm.[5]). Accordingly, we increased the systematic uncertainty in the Mg I result to 0.02 dex.

The 3D non-LTE result from the unweighted mean of six lines of Mg II is significantly smaller: $\log \epsilon_{Mg} = 7.52 \pm 0.03$ (statistical). The Mg II results have a noticeably larger line-to-line scatter, beyond the uncertainties in the adopted gf-values, which are all classified A or A+ ($\delta \log gf \leq \pm 0.01$ dex) by NIST (Kramida 2019). The systematic uncertainty as estimated from the 3D LTE, ⟨3D⟩, and HM models is 0.03 dex and is primarily driven by the large departures from LTE, in particular for three of the lines. Notably, we found that these lines are highly sensitive to the adopted recipe for inelastic collisions between Mg II and neutral hydrogen. Our results here are based on the Drawin (1968) recipe as formulated by Lambert (1993), without any ad-hoc scale factors applied, for lack of a better approach. Since the 3D LTE result is $\log \epsilon_{Mg} = 7.58$, more efficient collisions would help bring the Mg II result into better agreement with Mg I. Another uncertainty concerns the choice of Mg abundance for calculating the equation of state and hence electron pressures. Here, this abundance was varied consistently with the line formation calculations. An alternative approach would fix the Mg abundance to the value used to construct the model atmosphere ($\log \epsilon_{Mg} = 7.60$) and vary the gf-values instead. Test calculations on the ⟨3D⟩ model suggest that this alternative approach could increase the overall Mg II result by almost 0.02 dex; the electron pressure does not affect Mg I to first order since it is the minority ionisation stage in the solar photosphere.

Our recommended 3D non-LTE Mg abundance is the average of Mg I and Mg II, weighted by the total statistical and systematic errors: $\log \epsilon_{Mg} = 7.55 \pm 0.03$. A case could also be made for only adopting the Mg I results given the additional complications with Mg II, but the final abundance would only be 0.01 dex higher.

Aluminium (Z = 13). Nordlander & Lind (2017) recently performed full 3D non-LTE spectral line formation calculations for Al I lines in the Sun, based on their new model atom that includes realistic cross-sections for inelastic collisions with neutral hydrogen (Belyaev 2013). They employed the same 3D hydrodynamical Stagger model solar atmosphere and 3D non-LTE radiative

---

5 https://github.com/barklem/abo-cross

transfer code `Balder` as we employed in this study. Impressively, their solar modelling also agrees well with the observed IR emission lines of Al I. They adopted the same lines and line data as in Scott et al. (2015b), except that they excluded the 1089.1 nm line due to telluric contamination, finding a solar photospheric Al abundance of $\log \epsilon_{Al} = 6.43 \pm 0.03$ (statistical + systematic). Here, we adopted the Nordlander & Lind (2017) solar abundance, which is identical to the 3D LTE results of Scott et al. (2015b); for the Sun, departures from LTE are in fact largely unimportant for these five Al I lines.

Silicon (Z = 14). Here, we adopted the solar Si abundance from our recent analysis (Amarsi & Asplund 2017), the first full 3D non-LTE line formation calculations performed for this element. The same atomic data and line weighting as in Scott et al. (2015b) were used for the nine Si I and one Si II lines. The inferred photospheric Si abundance ($\log \epsilon_{Si} = 7.51 \pm 0.03$) is identical to the values found by Asplund et al. (2009) and Scott et al. (2015b); this value is used to normalise the meteoritic abundance scale to the photospheric one, see Sect. 3.1.

It should be noted that Pehlivan Rhodin et al. (2021) recently computed new gf-values for a large number of Si I and Si II lines, which are partly validated against experimental data. Had we adopted those for the seven Si lines in common with our study, the photospheric abundance would have increased to $\log \epsilon_{Si} = 7.53 \pm 0.03$ with a slightly reduced statistical scatter and a corresponding adjustment of the meteoritic abundances. We did, however, opt to retain the older experimental transition probabilities (Garz 1973), renormalised to the lifetimes of Becker et al. (1980) and O'Brian & Lawler (1991), mainly since the new theoretical values imply a significant ionisation imbalance of 0.1 dex between Si I and Si II, even in 3D non-LTE. The overall agreement with the meteoritic abundances further supports the Garz (1973) data (see Sect. 3.2). Further theoretical and experimental work on Si would be very welcome.

Phosphorus (Z = 15). We adopted the results from the 3D LTE analysis of Scott et al. (2015b): $\log \epsilon_P = 5.41 \pm 0.03$. To our knowledge, no non-LTE investigation of P exists in the literature, neither in 1D nor 3D. Due to the similarity between the weak P I and S I lines, the latter for which non-LTE investigations do exist (see below), comparably small non-LTE effects could be expected for the two elements. The value is unchanged from Asplund et al. (2009).

Sulphur (Z = 16). The solar S abundance $\log \epsilon_S = 7.12 \pm 0.03$ is taken from Scott et al. (2015b) who included 1D non-LTE corrections (−0.01 dex for optical lines but −0.05.. − 0.10 for the IR lines) from Takeda et al. (2005) to their 3D LTE results. The value is unchanged from Asplund et al. (2009).

Potassium (Z = 19). The recommended solar K abundance in Asplund et al. (2009) was $\log \epsilon_K = 5.03 \pm 0.09$, which Scott et al. (2015b) updated to $\log \epsilon_K = 5.04 \pm 0.05$. The latter result was based on a 3D LTE analysis of five weak lines (excluding the strong 766.5 and 769.9 nm K I resonance lines) together with 1D non-LTE abundance corrections taken from Takeda et al. (1996) in the absence of consistent non-LTE calculations with a 3D solar model. Reggiani et al. (2019) recently presented a new 1D non-LTE analysis with a comprehensive model atom consisting of 133 atomic levels of K I plus the ground state of K II and 250 radiative bound-bound transitions. Particular attention was placed on calculating or adopting reliable cross-sections for inelastic collisions, both with electrons, and with neutral hydrogen. Their 1D non-LTE calculations with a theoretical hydrostatic `MARCS` model atmosphere using the equivalent widths of three lines (including

K I 769.9nm) yielded a solar abundance of $\log \epsilon_K = 5.11 \pm 0.01$ (standard deviation only).

Here, we present a full 3D non-LTE calculations for K I using the same model atom as in Reggiani et al. (2019). A summary of the inferred abundances for the different lines using a variety of model atmospheres is provided in Table A.1. Compared to Scott et al. (2015b), the gf-values have been updated to those recommended by NIST (Kramida 2019), which in all cases are estimated to have an accuracy better than 1%. Furthermore, the spectral line profiles were re-examined and the equivalent widths remeasured, leading us ultimately to exclude the 404.4 and 580.2 nm lines due to their substantial and uncertain blending. Our recommended solar K abundance is thus based on the measured equivalent widths of three K I lines: 693.9, 1177.0, and 1252.2 nm. Although we did not consider the K I 769.9 nm resonance line for the final result due to its large line strength and very pronounced non-LTE effects ($\approx + 0.2$ dex), we note that its 3D non-LTE-based solar K abundance is fully consistent with those of the weak K I lines. Nevertheless, the departures from LTE are noticeable for the three retained K I lines (3D non-LTE − 3D LTE $\approx − 0.05$ dex), which reinforces the importance of a consistent 3D non-LTE analysis as employed here. Our recommended solar K abundance, based on the unweighted mean of the three K I lines, is $\log \epsilon_K = 5.07 \pm 0.01$ (statistical) ± 0.03 (systematic).

Calcium (Z = 20). Scott et al. (2015b) slightly revised the present-day photospheric Ca abundance of Asplund et al. (2009) to $\log \epsilon_{Ca} = 6.32 \pm 0.03$ with excellent agreement between the eleven Ca I and five Ca II lines employed. These results were based on 3D LTE line formation calculations with our own 1D non-LTE abundance corrections calculated on the ⟨3D⟩ model atmosphere, which range from +0.02 to −0.03 dex for Ca I, and 0.00 to −0.07 dex for Ca II. Recently, Mashonkina et al. (2017) and Osorio et al. (2019) presented new 1D non-LTE investigations that predict more severe, negative, non-LTE corrections for both species but more so for Ca II, which would worsen the ionisation balance obtained in Scott et al. (2015b).

In light of these issues, we carried out a detailed reanalysis of Ca, based on a consistent 3D non-LTE line formation study for the Sun. Our new Ca model atom consists of 141 Ca I levels, 46 Ca II levels, and the Ca III ground state, which are coupled radiatively by 2271 bound-bound and 135 bound-free transitions. We employed data for inelastic collisions with electrons from Zatsarinny et al. (2019b) for Ca I and from Meléndez et al. (2007) for Ca II; while for inelastic collisions with neutral hydrogen we draw on data from Barklem (2016b) and Belyaev et al. (2018) for Ca I and Ca II, respectively. Osorio et al. (2020) reported a non-negligible influence of non-LTE effects on Mg I influencing the statistical equilibrium of Ca in the Sun. We therefore ran test calculations with the background Mg opacity treated in non-LTE; however, these were found to have a negligible impact on our results, at least for the Ca lines adopted in our abundance analysis.

A summary of the inferred abundances for the different lines using a variety of model atmospheres is provided in Table A.1. Compared to Scott et al. (2015b), we adopted the same line data and mostly the same lines, dropping only the 616.13 nm that is affected by the broad damping wings of the neighbouring Ca I 616.22 nm line. The unweighted mean results from the ten Ca I lines and the five Ca II lines agree to better than 0.005 dex, with a very small line-to-line scatter for each species. Our recommended solar Ca abundance is $\log \epsilon_{Ca} = 6.30 \pm 0.03$ (total).

2.5. Fe-peak elements: Scandium to nickel

Scandium (Z = 21). Scott et al. (2015a) relied on a 3D LTE analysis of five Sc I and nine Sc II lines coupled with non-LTE corrections computed with 1D model atmospheres to determine a solar Sc abundance of $\log \epsilon_{Sc}$ = 3.16 ± 0.04. With the new, highly accurate experimental transition probabilities of Lawler et al. (2019), the weighted average becomes $\log \epsilon_{Sc}$ = 3.14 ± 0.01 (statistical) ±0.04 (systematic)[6]. It is noted that the departures from LTE are substantial for the Sc I lines, but the weighted mean Sc abundance is largely driven by Sc II. There is good agreement between the two ionisation stages, both of which give noticeably higher abundances than the CI meteoritic value (Sect. 3.1). Lawler et al. (2019) considered roughly twice as many Sc lines in their solar analysis, many of which are clean and have excellent atomic data; we postpone for later a study of these lines in conjunction with 3D non-LTE calculations and realistic collisional cross-sections.

Titanium (Z = 22). In their analysis of Fe-peak elements, Scott et al. (2015a) already benefited from the highly accurate experimental transition probabilities for Ti from the Wisconsin atomic physics group (Ti I: Lawler et al. 2013; Ti II: Wood et al. 2013[7]). They also applied non-LTE abundance corrections calculated with 1D model atmospheres, which are significant for Ti I ($\approx +0.06$ dex) but unimportant for Ti II. Scott et al. (2015a) found a large and unexplained difference in Ti abundance from the two ionisation stages: 4.88 ± 0.05 versus 4.97 ± 0.04 from Ti I and Ti II, respectively; their recommended solar Ti abundance was a weighted average of the two, resulting in $\log \epsilon_{Ti}$ = 4.93 ± 0.04. It is noteworthy that all of the considered theoretical and semi-empirical 1D model atmospheres implied significantly larger Ti I abundances than with the 3D `Stagger` model and more in line with the Ti II results. This strong model atmosphere sensitivity suggests that the adopted 1D non-LTE corrections are not appropriate in 3D and that a consistent 3D non-LTE analysis would yield higher Ti I abundances. In contrast to Scott et al. (2015a), we based our recommended solar Ti abundance solely on Ti II but increased the final error somewhat to reflect the discrepancy between the ionisation stages: $\log \epsilon_{Ti}$ = 4.97 ± 0.05 (total). A full 3D non-LTE study with realistic collisional cross-sections would be highly desirable; Lawler et al. (2013) and Wood et al. (2013) list a large number of high-quality Ti lines with now excellent atomic data available.

Vanadium (Z = 23). The recommended solar photospheric V abundance of Scott et al. (2015a) was based on a 3D LTE analysis of V I lines with an ad hoc non-LTE correction of 0.10 dex across the board in the absence of actual statistical equilibrium calculations based on the behaviour of Sc and Ti in 1D model atmospheres. As a minority species, V I is very sensitive to the atmospheric structure: the four considered theoretical and semi-empirical 1D model atmospheres imply a 0.07−0.18 dex higher abundance. Unfortunately, little guidance is available from the

few available V II lines due to their heavy blending, although nominally they suggest a ≈0.1 dex higher V abundance, both in 3D and 1D. Updating the Scott et al. (2015a) results with the Lawler et al. (2014) and Wood et al. (2014a) experimental gf-values, the mean V I abundance is only +0.01 dex higher, while the V II result changes by −0.02 dex[8]. We caution that our ad hoc V I non-LTE correction may well be underestimated, and we strongly encourage the first non-LTE investigation of this element to be performed. In the meantime we recommend the value found by Scott et al. (2015a) updated with the Lawler et al. (2014) transition probabilities: $\log \epsilon_V$ = 3.90 ± 0.08 (total).

Chromium (Z = 24). The solar photospheric Cr abundance of Scott et al. (2015a) was based on the weighted average of a large number of Cr I and Cr II lines with 1D non-LTE abundance corrections. Updating this result with the new experimental Cr II transition probabilities of Lawler et al. (2017) leads to the same mean abundance: $\log \epsilon_{Cr}$ = 5.62 ± 0.04.

Manganese (Z = 25). A new solar Mn abundance analysis was presented by Bergemann et al. (2019) based on full 3D non-LTE calculations. Using the same 3D hydrodynamical solar model (Magic et al. 2013) as for other elements and equipped with new ab initio inelastic Mn I+H I collisional cross-sections from Belyaev & Voronov (2017) (see also Grumer & Barklem 2020), they obtained $\log \epsilon_{Mn}$ = 5.52 ± 0.04. This is 0.10 dex larger than the result of Scott et al. (2015a)(5.42 ± 0.04) based on 3D LTE model spectra combined with ⟨3D⟩ non-LTE abundance corrections; the two results do not overlap within the error bars. The two studies have very few Mn I lines in common, making a detailed comparison difficult. The abundance difference cannot be traced to the adopted transition probabilities since the same sources are employed (mostly Den Hartog et al. 2011 and Blackwell-Whitehead & Bergemann 2007). Departures from LTE are obviously very prominent, with the 1D non-LTE − 1D LTE difference being +0.07 dex. according to Bergemann et al. (2019). One may suspect that the 3D non-LTE effects and Mn abundances in Bergemann et al. (2019) have been somewhat overestimated due to incomplete UV line blanketing over-estimating the photo-ionisation rates and thus weakening the predicted Mn I lines; a detailed comparison is further complicated by Bergemann et al. (2019) employing different non-LTE radiative transfer codes for their 1D and 3D analyses.

Until the situation has been clarified, we advocate the recommended photospheric Mn abundance of Scott et al. (2015a) but with increased errors to reflect the remaining uncertainties associated with the non-LTE modelling: $\log \epsilon_{Mn}$ = 5.42 ± 0.06. Some confidence in this result can be had by noting that Scott et al. (2015a) obtained a value of 5.43 from their consistent ⟨3D⟩ non-LTE analysis, only 0.01 dex larger. Our expectation is that, at least for atomic and ionic species in the disc-centre intensity spectrum of the Sun, the full 3D non-LTE result for Mn should be similar to the ⟨3D⟩ non-LTE abundance, as we have found in our investigations of Li, C, N, O, Na, Mg, Al, Si, K, Ca, and Fe. Nevertheless, we encourage the issue to be revisited with new 3D non-LTE calculations with realistic inclusion of blending lines both for the statistical equilibrium and for the Mn I abundance diagnostic lines.

---

[6] Pehlivan Rhodin et al. (2017a) also measured new lifetimes, which coupled with theoretical branching factors yield new rescaled semi-empirical Sc II oscillator strengths. Adopting those instead and excluding the highly discrepant 442.07 nm line would yield a Sc abundance of $\log \epsilon_{Sc}$ = 3.10 ± 0.05. Here, we preferred the arguably less uncertain experimental values of Lawler et al. (2019), which are available for all of our lines.

[7] Li et al. (2020) presented a new set of theoretical Ti II gf-values, which are in good overall agreement with the Wood et al. (2013) experimental values, although they lead to significantly larger abundance scatter for our lines; we assess the latter source to be more reliable for our purposes.

[8] Holmes et al. (2016) measured new experimental transitional probabilities but only for a subset of our solar diagnostics lines. On average, the difference with the Lawler et al. (2014) values is small, ≈+0.02 dex, and the line-to-line abundance scatter would increase somewhat. We argue that the Lawler et al. (2014) data are preferable for our purposes (see also Saloman & Kramida 2017).

Iron (Z = 26). In astronomy, Fe is often used as a proxy for the overall metallicity of a star on account of the element's relatively high abundance and the wealth of readily measurable lines. Iron is also an important opacity contributor in stellar interiors. In the Sun, many lines of both Fe I and Fe II with accurate experimental atomic data are available for a spectroscopic analysis (e.g., Grevesse & Sauval 1999; Asplund et al. 2000c; Caffau et al. 2011; Mashonkina et al. 2011). From a 3D analysis, Scott et al. (2015a) obtained 7.45 ± 0.04 (including 1D non-LTE corrections of $\approx +0.01$ dex) and 7.51 ± 0.04, from Fe I and Fe II lines, respectively, leading to a weighted average of $\log \epsilon_{Fe} = 7.47 \pm 0.04$ (statistical + systematic). Lind et al. (2017) updated this to $\log \epsilon_{Fe} = 7.47 \pm 0.04$ based on fully consistent 3D non-LTE calculations for Fe that for the first time were based on a large model atom that included ab initio collisional cross-sections for Fe I+H I (Barklem 2018).

We undertook a new analysis of Fe I and Fe II using full 3D non-LTE calculations and improved atomic data. Our new Fe model atom consists of 100 Fe I levels, 76 Fe II levels, and the Fe III ground state, which are radiatively coupled through 4313 bound-bound and 100 bound-free transitions, amounting to 46000 wavelength points. We employed data for inelastic collisions with electrons from Wang et al. (2018) for Fe I and from Bautista et al. (2015) and Zhang & Pradhan (1995) for Fe II; while for inelastic collisions with neutral hydrogen, we drew on data from Barklem (2018) and Yakovleva et al. (2019) for Fe I and Fe II, respectively. Photoionisation cross-sections for Fe I were sourced from Zatsarinny et al. (2019a). Recently, new accurate experimental transition probabilities for additional excellent solar Fe I lines have been published (Den Hartog et al. 2014; Belmonte et al. 2017), which we employed together with previous lines used by Scott et al. (2015a) with the transition probabilities recommended by the Oxford (e.g., Blackwell et al. 1995), Hannover (e.g., Holweger et al. 1991), and Wisconsin (e.g., O'Brian et al. 1991) groups[9].

A summary of the inferred abundances for the different lines using a variety of model atmospheres is provided in Table A.2. We now obtain excellent agreement between the two ionisation stages: 7.46 ± 0.04 and 7.47 ± 0.04 from Fe I and Fe II respectively, based on unweighted means and including statistical and systematic uncertainties. Departures from LTE are small for both species in the Sun. There are no significant dependencies with wavelength, excitation potential, line strength or provenance of the gf-values in 3D, in contrast to the results using the 1D semi-empirical Holweger & Müller (1974) model atmosphere (Fig. 2). With 1D theoretical models, the mean Fe abundance becomes unrealistically low ($\log \epsilon_{Fe} < 7.40$), while with the $\langle 3D \rangle$ model, ionisation balance is not fulfilled, thus attesting to the need for full 3D non-LTE calculations. Our recommended photospheric Fe abundance is the average of the Fe I and Fe II results: $\log \epsilon_{Fe} = 7.46 \pm 0.04$ (total), a value which has hardly moved over the past two decades in spite of major improvements in 3D and non-LTE analysis techniques and better atomic data (Asplund et al. 2000c, 2005a, 2009; Bergemann et al. 2012; Scott et al. 2015a; Amarsi et al. 2016b; Lind et al. 2017).

Cobalt (Z = 27). We update the Scott et al. (2015a) results with the gf-values from Lawler et al. (2015) for the Co I lines in common: $\log \epsilon_{Co} = 4.94 \pm 0.05$ (total). While the new Co abundance is only 0.01 dex higher, the reduced line-to-line scat-

---

[9] We did not utilise any of the IR Fe I lines for which new experimental data are now available (Ruffoni et al. 2013) since these particular lines are typically too strong and/or blended in the Sun for a high-precision analysis.
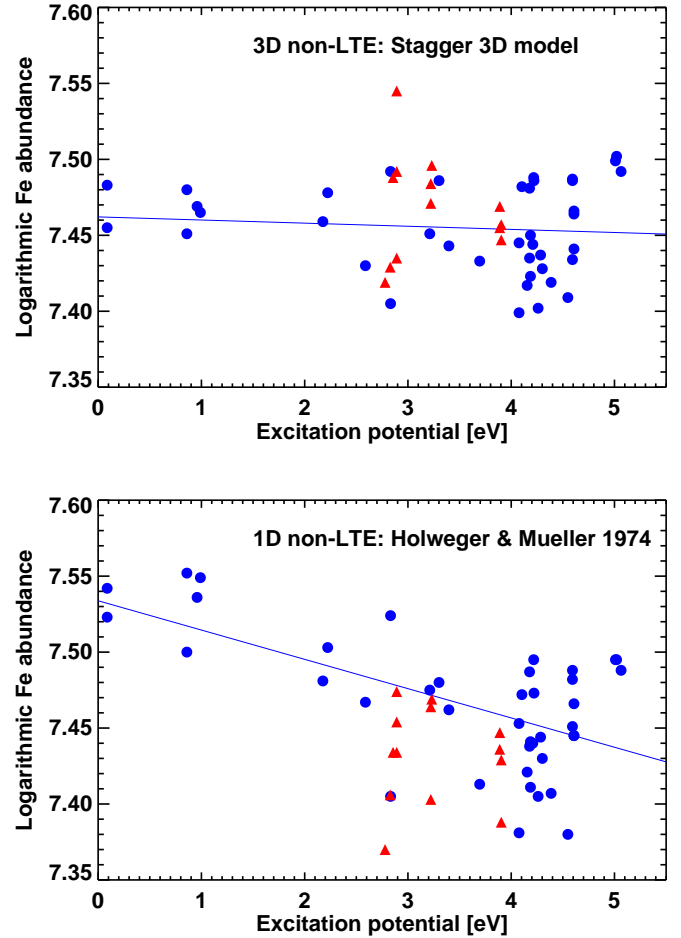
Fig. 2. Inferred photospheric Fe abundances from detailed non-LTE calculations using the 3D hydrodynamical Stagger model (*upper panel*) and the 1D Holweger & Müller (1974) model (*lower panel*). The results for Fe I and Fe II lines are shown as blue circles and red triangles, respectively. The solid lines denote the least-square fits to the Fe I results. In 3D non-LTE, there is excellent excitation and ionisation balance for Fe, contrary to the 1D case; it is noted that the trend with excitation potential with the Holweger & Müller (1974) model is even steeper in LTE (see Table A.2).

ter is a testament to the high accuracy of the new experimental data. As for most Fe-peak elements, one concern relates to the adopted non-LTE corrections, which may be prone to error as they stem from our 1D calculations, and mainly draw on classical and semi-empirical recipes for inelastic collisions with electrons and with neutral hydrogen.

Nickel (Z = 28). In the absence of any non-LTE calculations for Ni I, we adopt the 3D LTE based Ni abundance of Scott et al. (2015a), who used the accurate experimental transition probabilities from Wood et al. (2014b): $\log \epsilon_{Ni} = 6.20 \pm 0.04$. Based on our detailed 3D non-LTE calculations for Fe I, we expect the non-LTE effects for Ni I to be similarly minor, but this requires confirmation.

2.6. The heavy elements: Copper to uranium

Relatively little work has been done recently to update the solar photospheric analysis by Grevesse et al. (2015) of the neutron capture elements. With the exception of the elements listed below, we adopt their recommended solar abundances. We note

that many of these elements have few available spectral lines located in the crowded UV region, causing major problems in fitting the lines. Taking an even more conservative approach, we deemed some lines used by Grevesse et al. (2015) as too uncertain for a meaningful abundance determination even if very few, if any, alternative lines of the element are available. In some cases, we increased the error bars to attest to the challenges in working with heavily blended lines; often the blending lines are not even identified. The reader is furthermore cautioned that departures from LTE are largely unexplored territory for the heavy elements in the Sun. This deficiency can be expected to introduce significant systematic errors, quite possible at the level of ±0.1 dex, in particular for many of the minority species.

Copper (Z = 29). We retain the solar Cu abundance $\log \epsilon_{Cu} = 4.18 \pm 0.05$ of Grevesse et al. (2015) despite it relying on old and relatively uncertain experimental oscillator strengths (e.g., Kock & Richter 1968) since the newer theoretical gf-values of Liu et al. (2014) imply an unacceptably large line-to-line abundance scatter. New laboratory data for this astrophysically important element would be welcome.

Germanium (Z = 32). We reinspected the spectral line profile of the quite strong but blended Ge I 326.95 nm line and revised the equivalent width downwards relative to Grevesse et al. (2015) to 4.20 pm. Our 3D LTE result consequently shifts downwards to $\log \epsilon_{Ge} = 3.62 \pm 0.10$.

Rubidium (Z = 37). The only two available Rb I lines in the solar spectrum, the resonance lines at 780.03 and 794.76 nm, are unfortunately both perturbed by other species. We revised the measured line strengths of Grevesse et al. (2015) (to 0.53 and 0.29 pm, respectively) to better account for these blends and adjusted the remaining uncertainties to reflect the difficulties in fitting the weak Rb I lines. The resulting 3D LTE abundance is slightly lower than before: $\log \epsilon_{Rb} = 2.44 \pm 0.08$ (total). Very recently, Korotin (2020) performed 1D non-LTE calculations for the Rb I resonance lines, employing ab initio data for inelastic collisions with neutral hydrogen (Yakovleva et al. 2018). They found substantial departures from LTE ($\Delta \log \epsilon_{Rb} = -0.12$ dex) and a solar Rb abundance consistent with the meteoritic value for the first time[10]. Their study employed blending lines in the statistical equilibrium computations as well as Rb spectrum synthesis. Applying the new non-LTE corrections of Korotin (2020) to our 3D LTE value above implies a solar Rb abundance of $\log \epsilon_{Rb} = 2.32 \pm 0.08$.

Rhodium (Z = 45). We updated the Grevesse et al. (2015) Rh abundance with the new experimental transition probabilities for Rh I lines from Malcheva et al. (2015), while restricting the analysis to the 369.24 nm line due to the heavy blending of the 343.49 nm line. When also considering the uncertainties in the line strength and gf-values, we obtain $\log \epsilon_{Rh} = 0.78 \pm 0.11$ (statistical + systematic). The derived photospheric Rh abundance remains substantially below the value measured in CI chondrites, which may indicate pronounced departures from LTE for this minority species in the 3D model that are not yet possible to account for. It is noted that 1D semi-empirical solar

---

atmosphere models yield abundances in better agreement with the meteoritic evidence; the shallower temperature gradient of the Holweger & Müller (1974) model tends to result in smaller departures from LTE (Asplund 2005), a phenomenon termed 'non-LTE masking' by Rutten & Kostik (1982).

Palladium (Z = 46). We reassessed the Pd I lines at 324.27 and 340.46 nm and revised their equivalent widths upwards relative to Grevesse et al. (2015), to 2.50 pm and 3.58 pm, respectively. Our 3D LTE result consequently shifts upwards to $\log \epsilon_{Pd} = 1.57 \pm 0.10$, which is incidentally identical to the value recommended by Asplund et al. (2009).

Barium (Z = 56). Unfortunately, only a few spectral lines of Ba are available as abundance diagnostics, which furthermore are strong and saturated. The solar Ba abundances presented in Asplund et al. (2009) and Grevesse et al. (2015) were based on 3D LTE calculations to which 1D non-LTE abundance corrections were applied; naturally this approach is not fully self-consistent, but it was the only one available at the time for this element. Very recently, Gallagher et al. (2020) revisited the issue using full 3D non-LTE computations with the same Stagger 3D hydrodynamical solar model as employed elsewhere in our study. Their inferred solar Ba abundance of $\log \epsilon_{Ba} = 2.27 \pm 0.01$ (statistical) ±0.02 (systematic) was obtained from a 1D LTE spectrum synthesis with a MARCS model atmosphere (Gustafsson et al. 2008) to which abundance corrections from blending lines and 3D (i.e. the differences in abundances in 3D non-LTE to obtain the 1D LTE equivalent width) were applied separately; this is not fully consistent either, but it is a more realistic approach than that in Grevesse et al. (2015). In addition to the three Ba II lines employed by Grevesse et al. (2015), Gallagher et al. (2020) also considered the heavily blended 614.17 nm line and obtained consistent results. It is noted that the 3D LTE abundances in the two studies differ substantially for unknown reasons.

Here, we adopt the Gallagher et al. (2020) 3D non-LTE based result but inflate their uncertainties slightly to account for possible systematic errors from the model atmosphere, non-LTE calculations, and their assumed microturbulence in 1D: $\log \epsilon_{Ba} = 2.27 \pm 0.05$ (total). A new study directly comparing the 3D non-LTE line profiles (including blends) with observations would be welcome for this important element, especially given the difference with the CI chondritic abundance ($\log \epsilon_{Ba} = 2.18 \pm 0.02$).

Praseodymium (Z = 59). We apply the 1D non-LTE abundance correction (+0.03 dex) for Pr I from Mashonkina et al. (2009) to the 3D LTE results of Grevesse et al. (2015), which in turn was based on 3D abundance corrections applied to the 1D spectrum synthesis of Sneden et al. (2009). The revised Pr abundance becomes $\log \epsilon_{Pr} = 0.75 \pm 0.05$.

Tungsten (Z = 74). Compared to Grevesse et al. (2015), we remove the weak 484.38 nm line owing to uncertainties in measuring its equivalent width. Therefore, restricting the 3D LTE analysis of Grevesse et al. (2015) to the W I 400.875 nm line implies $\log \epsilon_{W} = 0.79 \pm 0.11$.

Osmium (Z = 76). After inspecting the spectral line profile of the Os I 330.16 nm transition, we revise its equivalent width downwards relative to Grevesse et al. (2015), to 0.86 pm. The resulting 3D LTE result is 0.05 dex lower: $\log \epsilon_{Os} = 1.35 \pm 0.12$.

Iridium (Z = 77). We judge that the only detectable Ir I line, at 322.08 nm, is too badly blended and has too uncertain a continuum placement to allow us to make a meaningful solar Ir abundance measurement.

---

[10] Even more recently, Takeda (2021) performed a similar 1D non-LTE study, including for the Sun, where they found a less noticeable non-LTE correction: −0.05 dex. Because they only considered the classical Drawin (1968) formula with a scaling factor for the inelastic H collisions and no specification is given as to which recipe for the electron collisions is employed, we here give a preference to the results of Korotin (2020). Revisiting the solar Rb abundance issue with 3D non-LTE calculations would be desirable.

Gold (Z = 79). Accounting for the uncertain continuum placement around the weak and badly blended Au I 312.28 nm line leads to a more conservative error estimate than in Grevesse et al. (2015): $\log \epsilon_{Au} = 0.91 \pm 0.12$ (total).

Lead (Z = 82). We update the solar Pb abundance based on our new measurement of the equivalent width (0.91 pm) of the Pb I 368.35 nm, which results in $\log \epsilon_{Pb} = 1.95 \pm 0.08$, 0.03 dex larger than in Grevesse et al. (2015).

2.7. Elements observed in sunspots: Fluorine, chlorine, indium, and thallium

Fluorine (Z = 9). While no spectral lines of F are detectable in the photospheric spectrum of the quiet Sun, there are features of the HF molecule in sunspot spectra that enable a determination of the solar F abundance. Maiorca et al. (2014) analysed the umbral atlas of Wallace et al. (2001) with a 1D theoretical model atmosphere corresponding to an effective temperature of $T_{eff} = 4250$ K to estimate $\log \epsilon_F = 4.40 \pm 0.25$; most of the uncertainty stems from the choice of model atmosphere since the employed radiative-equilibrium model without magnetic fields may not be appropriate for this particular sunspot umbra. Here, we recommend the value of Maiorca et al. (2014), which represents a 0.16 dex reduction compared to the older Hall & Noyes (1969) result adopted by Asplund et al. (2009).

Chlorine (Z = 17). Similar to F, the photospheric Cl abundance can only be estimated from sunspot spectra since the HCl molecule requires cool temperatures; no atomic features of Cl are present in the solar spectrum. Recently, Maas et al. (2016) revisited the previous HCl sunspot study of Hall & Noyes (1972) with improved molecular data and observations to obtain a 0.19 dex lower abundance: $\log \epsilon_{Cl} = 5.31 \pm 0.12$. Given the remaining model challenges, especially in finding a suitable model atmosphere for a sunspot of unknown T_{eff}, we argue that the quoted uncertainty is likely overly optimistic, and we instead adopt ± 0.20 dex. A more accurate determination of the solar abundances of the halogen elements would be possible through the abundance ratio of another species with similar temperature dependence and spectral features with well-determined gf-values, such as FeH and MgH.

Indium (Z = 49). Analyses of the In I 451.13 nm spectral line in the quiet Sun have traditionally yielded an In abundance much higher than the CI chondritic value (e.g., Bord & Cowley 2002: $\log \epsilon_{In} = 1.56 \pm 0.20$). Vitas et al. (2008) showed that this is likely due to an unknown blend and instead confirmed that the solar In abundance is close to the meteoritic value based on a sunspot spectrum: $\log \epsilon_{In} = 0.80 \pm 0.20$. We adopt this value here, as we did in Asplund et al. (2009).

Thallium (Z = 81). The most recent determination of the solar Tl abundance dates back almost half a century. Updating with the current NIST-recommended transition probability for the only viable but heavily blended Tl I 535.04 nm line, the sunspot analysis of Lambert et al. (1972) suggests $\log \epsilon_{Tl} = 0.92 \pm 0.17$, quite likely with an underestimated uncertainty. A more accurate determination would be possible from the abundance ratio with another similar species such as Zr I.

2.8. Indirect abundance determinations: Noble elements

The photospheric abundance of the noble gases cannot be inferred directly from spectroscopy due to the extremely high excitation potentials and thus minuscule level populations involved. Other indirect methods are therefore required.

Helium (Z = 2). The solar He abundance can be derived from the corona, prominences, solar wind, solar-energetic particles, and the gas giant planets. However, the He/H ratio varies greatly depending on environment, from 0.01 to 0.09 (e.g., Bochsler 2007; Reames 2014). The Genesis sample return mission of the solar wind implies a ratio of about 0.05 (Huss et al. 2020), which is significantly lower than expected in the Sun as a result of Coulomb-drag fractionation.

Here, we instead rely on helioseismology, which enables an accurate determination of the He abundance in the solar convection zone and thus photosphere, which cannot be probed spectroscopically. The change in the adiabatic index $\Gamma_1 = (\partial \ln P / \partial \ln \rho)_S$ in the He II ionisation zone occurring at temperatures $T \approx 10^5$ K (corresponding to a radius of $r \approx 0.98 R_\odot$) leaves an observable signature in the p-mode oscillation frequencies that depends on the He content (e.g., Basu 2016 and references therein). In Asplund et al. (2009), we adopted the helioseismic He mass fraction value of $Y_{surface} = 0.2485 \pm 0.0034$ from Basu & Antia (2004); most of the quoted uncertainty stems from the choice of equation of state (OPAL: Rogers & Nayfonov 2002 vs. MHD: Mihalas et al. 1988). Due to the overlapping higher ionisation zones of other abundant elements, especially O, there is a degeneracy with the adopted metal mass fraction $Z_{surface}$ in the reference solar model for the helioseismic inversion: $\delta Y_{surface} / \delta Z_{surface} = -1.06$ and -0.56 with the OPAL (Basu & Antia 2004) and MHD (Trampedach et al. 2006) equation of states, respectively. Using a similar technique but with the improved SAHA-S3 equation of state, Vorontsov et al. (2013) obtained maximum-likelihood estimates of $Y_{surface} = 0.240 - 0.255$ and $Z_{surface} = 0.008 - 0.013$.

Taking the mean of the Basu & Antia (2004) and Vorontsov et al. (2013) He abundances corrected to our recommended present-day photospheric composition ($Z_{surface} = 0.0139$, Sect. 5) implies $Y_{surface} = 0.2423 \pm 0.0054$, which we adopt here. In terms of the standard logarithmic scale, this corresponds to $\log \epsilon_{He} = 10.914 \pm 0.013$, or He/H=0.082 by number density.

Neon (Z = 10). The absolute Ne abundance can be determined from the radiation originating in the high-temperature regions of the Sun (e.g., transition region, corona, flares) or in situ measurements of the solar wind and solar energetic particles. Both types of analyses are, however, complicated by the existence of the still poorly understood first ionisation potential (FIP) effect (e.g., Laming 2015); the abundances in the upper solar atmosphere and solar wind are modified relative to the photospheric values by a degree inversely dependent on the elemental ionisation potential. Arguably a more reliable approach, that we employ here, is to combine the abundance ratio of Ne ($\chi_{ion} = 21.56$ eV) with an element with a similarly high ionisation potential and its photospheric abundance, under the assumption that the two elements experience the same, or at least a very similar, FIP effect.

A common comparison element is O ($\chi_{ion} = 13.62$ eV) since it can be measured in conjunction with Ne in the upper atmosphere and solar wind, and its photospheric abundance can be determined spectroscopically (albeit with challenges, Sect. 2.3); it is certainly conceivable that the difference in ionisation potential could still introduce elemental variations. Young (2018) recently revisited the measured abundance ratios in the transition region of the quiet Sun, finding a significantly higher Ne/O ratio than previously estimated: Ne/O=0.24 $\pm$ 0.05 compared with

0.175 ± 0.031 by Young (2005). Most of this adjustment comes from improvements in the atomic data, resulting in changes to the ionisation and recombination rates. Together with our photospheric O abundance, this would imply a photospheric Ne abundance of $\log \epsilon_{Ne} = 8.08 \pm 0.09$, a 40% increase compared with the value recommended in Asplund et al. (2009) using the Young (2005) Ne/O ratio.

Landi et al. (2007) inferred the absolute coronal Ne abundance from solar flare spectra: $\log \epsilon_{Ne} = 8.11 \pm 0.12$. There are, however, variations between flares both in the absolute Ne abundances (e.g., $\log \epsilon_{Ne} = 7.92 \pm 0.03$ Landi & Testa (2015) and in the Ne/O ratio during the solar cycle as a result of the FIP effect. It is expected that the results are the least susceptible to the FIP effect during solar minima, for which Landi & Testa (2015) obtained Ne/O= 0.25 ± 0.05, in perfect agreement with the quiet Sun transition region determination by Young (2018). The Ne/O ratio is typically lower in solar energetic particles (e.g., 0.140−0.157 ± 0.010, Reames 2020) and solar wind (e.g., 0.11−0.14, Reisenfeld et al. 2013), which suggests the existence of additional elemental fractionation. Thus, inferences of the absolute solar composition directly from solar wind measurements (e.g., von Steiger & Zurbuchen 2016) are likely prone to systematics and are probably unreliable (for further discussion see Serenelli et al. 2016).

An independent probe of the Ne abundance is offered by the measurements from the Genesis sample return mission (Burnett et al. 2019). Genesis offers a comparison with He, which has a more similar ionisation potential ($\chi_{ion} = 24.59$ eV) to Ne than O has. The quoted ^{4}He/^{20}Ne and ^{20}Ne/^{22}Ne ratios from the Genesis study of Heber et al. (2009) together with the helioseismic He/H ratio in the convection zone lead to a solar Ne abundance of $\log \epsilon_{Ne} = 8.14 \pm 0.01$. When accounting for correlations in the measured Ne/He and H/He ratios in different solar wind regimes, the abundance becomes $\log \epsilon_{Ne} = 8.06 \pm 0.03$ (Burnett et al. 2019; Huss et al. 2020), which is in excellent agreement with the above estimate using the Young (2018) Ne/O ratio. In the absence of a proper understanding of the physical processes responsible for the FIP effect, it is difficult to estimate the full uncertainties attached to this Genesis abundance. We tentatively assign half the difference between Heber et al. (2009) and Burnett et al. (2019) as a systematic error, which leads to our final recommended solar photospheric Ne abundance of $\log \epsilon_{Ne} = 8.06 \pm 0.03$ (statistical) ±0.04 (systematic). The excellent agreement with the coronal value by Young (2018) lends strong support to this 0.13 dex higher abundance than in Asplund et al. (2009) and consequently also the here advocated photospheric O abundance.

Argon (Z = 18). Asplund et al. (2009) used the straight average from a variety of methods to arrive at a solar Ar abundance of $\log \epsilon_{Ar} = 6.40 \pm 0.13$ following the procedure outlined by Lodders (2008): solar wind, solar flares and energetic particles, nuclear statistical equilibrium, Jupiter, and solar neighbourhood. Updating this exercise with new data and down-weighting the planetary and stellar data would lead to $\log \epsilon_{Ar} = 6.36 \pm 0.11$.

Here, we instead opt for a single, high-precision measurement: the Genesis sample return of the solar wind (Burnett et al. 2019), in the same manner as our recommended Ne abundance was determined. Allowing for correlations between the measured H/He and ^{36}Ar/^{4}He ratios, Burnett et al. (2019) and Huss et al. (2020) obtained $\log \epsilon_{Ar} = 6.38 \pm 0.08$ (statistical). We estimate that the remaining systematic errors are significant given the still poorly understood FIP effect (Laming 2015) and the differences in ionisation potential between Ar ($\chi_{ion} =$

15.76 eV) and the reference element He ($\chi_{ion} = 24.59$ eV); it is noted that Meshik et al. (2020) have argued that the FIP fractionation still varies with ionisation potential even for $\chi_{ion} > 13$ eV. We adopt $\log \epsilon_{Ar} = 6.38 \pm 0.10$ for the Sun.

Krypton (Z = 36). Here, we base the recommended solar Kr abundance on the Genesis measurements of the solar wind by Meshik et al. (2020). With the quoted Kr and H fluences, one obtains $\log \epsilon_{Kr} = 3.12 \pm 0.03$ (statistical). This value is preconditioned on the assumption that the FIP fractionation corrections are identical for Kr ($\chi_{ion} = 14.00$ eV) and H ($\chi_{ion} = 13.60$ eV) even when individually the corrections are about a factor of three. Alternatively, using the Kr and Ar ($\chi_{ion} = 15.76$ eV) fluences together with the above estimated solar Ar abundance leads to a slightly higher value with a greater statistical uncertainty: $\log \epsilon_{Kr} = 3.16 \pm 0.08$. Burnett et al. (2019) found a Kr abundance 0.2 dex lower with the same Genesis data when using O ($\chi_{ion} = 13.62$ eV) as the reference element, which may imply element-specific corrections for high-FIP elements beyond theoretical predictions (Meshik et al. 2020), or that the true photospheric O abundance is correspondingly much higher than advocated here (Laming et al. 2017). In all likelihood, the uncertainty is dominated by systematic errors from the FIP effect, whichever method is chosen. We adopt $\log \epsilon_{Kr} = 3.12 \pm 0.10$ including estimated systematic errors.

Traditionally, the solar Kr abundance has been estimated from the smooth variations in the abundances of nearby odd-mass number isotopes in CI chondrites (Sect. 3) as predicted by the measured cross-sections for the slow neutron capture process (e.g., Wisshak et al. 1998), a method originally proposed by Suess (1947a,b). With updated isotopic abundances, this leads to $\log \epsilon_{Kr} = 3.15 \pm 0.10$ (statistical). The true uncertainty is likely larger given that the odd-nuclei abundance smoothness has been questioned and that a more realistic distribution of neutron exposures than in this classical model leads to significantly different predictions for Kr (Arlandini et al. 1999). Nevertheless, it is reassuring that this completely independent method agrees well with the estimate based on the solar-wind.

Xenon (Z = 54). The Xe abundance can be inferred via the photospheric Sm measurement combined with experimental neutron capture cross-sections under the assumption that the reaction flow has reached equilibrium. Using their measured cross-sections for the pure s-process isotopes, ^{130}Xe and ^{150}Sm Reifarth et al. (2002) obtained $\log \epsilon_{Xe} = 2.24 \pm 0.01$ (statistical). With our updated photospheric Sm abundance, we revise this estimate slightly to $\log \epsilon_{Xe} = 2.22 \pm 0.05$, including estimated systematic errors (adopting the CI chondritic Sm abundance instead to normalise the s-process production would imply a 0.01 dex lower Xe abundance). The solar wind abundance inferred from Genesis data (Meshik et al. 2020) is significantly higher, $\log \epsilon_{Xe} = 2.42 \pm 0.05$ (statistical), suggesting a different FIP fractionation between Xe ($\chi_{ion} = 12.13$ eV) and H, as also expected on theoretical grounds (Laming et al. 2017).

3. Comparison with meteoritic abundances

3.1. Chemical composition of CI chondrites

Independent and complementary data on the overall chemical composition of the Solar System are offered by meteorites. The vast majority of the more than 50 000 meteorites found on Earth have undergone fractionation and alteration to varying degrees, leaving just a handful of the most primitive and undifferentiated carbonaceous chondrites, the so-called CI chondrites: the Alais,

Ivuna, Orgueil, Revelstoke, and Tonk meteorites, named after the locations of the falls[11]. On account of the overall similarities with the solar photospheric abundances, it has long been argued that the CI chondrites contain pristine samples of the original proto-solar nebula (e.g., Urey 1952, Cameron 1968; see Lodders 2019 for a historical overview). The aqueous alteration and thermal metamorphism of the textural and mineralogical structure all CI chondrites have experienced are not believed to have significantly changed its overall chemical composition, with the exception of the highly volatile elements that are strongly depleted (Palme et al. 2014)[12]. Since these depleted elements are also the most cosmically abundant, the meteoritic abundances by number densities are therefore traditionally normalised relative to Si: $N_{Si} \equiv 10^6$ (Suess & Urey 1956). To anchor the two sets of abundances onto the same scale, the meteoritic and photospheric Si abundances are therefore set equal with our recommended solar Si abundance (Sect. 2.4): $\log \epsilon_X = 1.51 + \log N_X$. In principle, more elements can be included in the conversion (e.g., Anders & Grevesse 1989; Lodders et al. 2009; Palme et al. 2014, who used 12, 39, and 38 elements, respectively), but for simplicity we only employ Si, which was also done by Asplund et al. (2005a, 2009) and Lodders (2019); we would have obtained the same result had we adopted the same normalisation elements as Palme et al. (2014).

Several literature compilations of the chemical compositions of CI chondrites exist, with Wasson & Kallemeyn (1988), Anders & Grevesse (1989), Lodders (2003), Lodders et al. (2009), Palme et al. (2014), and Lodders (2019) being particularly highly regarded and authoritative. These studies provide a comprehensive curation of a large number of original references of laboratory data on meteorites. Here (see Table 2), we adopt the CI chondritic abundances recommended by Palme et al. (2014) for the 83 elements for which data from the Orgueil meteorite exist. To convert the meteoritic abundance measurements by mass to the standard meteoritic abundance scale by number, we used the atomic weights recommended by Meija et al. (2016a) with a few adjustments to accommodate more representative Solar System isotopic ratios as described in Sect. 4. The quoted CI abundance uncertainties are only statistical sampling errors.

We did not attempt to factor in the recent measurements by Braukmüller et al. (2018) on account of the surprisingly large variation between their analyses of Orgueil and Ivuna, as well as with prior CI measurements for several elements, including Na, K, Zr, the rare Earth elements, and Th and U (Fig. 3). The Ivuna analysis by King et al. (2020) agrees well with the Palme et al. (2014) recommended abundances overall, although some striking discrepancies exist, including for S, P, K, Zr, Ba, Hf, Ta, W, and Th and U (Fig. 3). These differences can largely be traced to increased mobility in fluids for some elements during the aqueous alterations of the CI chondrites (Palme et al. 2014; Braukmüller et al. 2018). The recommended values of Palme et al. (2014) agree very well with the newer compilation by Lodders (2019), with a few exceptions. Notable changes have occurred for C, N, F, Br, Sb, I, and Hg, as seen in Fig. 3, but those elements are also among the most uncertain. Lodders (2019) performed a weighted average of the available analyses of all CI
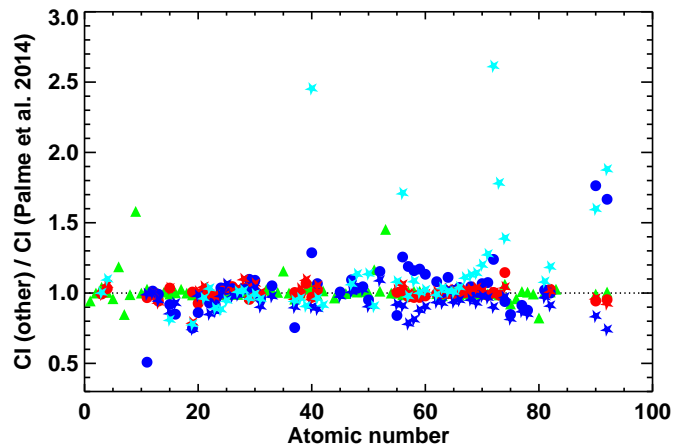

Fig. 3. Comparison between the recommended CI chondritic abundances by Palme et al. (2014), which we have adopted here, with other recent CI analyses (red symbols: Barrat et al. 2012; blue: Braukmüller et al. 2018; turquoise: King et al. 2020; green: Lodders 2019). Circle symbols correspond to data for the Orgueil meteorite, star symbols are for the Ivuna CI chondrite, and triangles for mean of all CI chondrites. All data are published abundances (ppm by mass) relative to Palme et al. (2014).

chondrites, but since they did not provide references to the original data, we instead opted for the compilation of Palme et al. (2014).

3.2. CI chondritic and photospheric abundances

Figure 4 shows a comparison of our recommended present-day solar photospheric abundances with those from CI chondrites on the astronomical logarithmic abundance scale. Clearly, the agreement is very good overall, with a few striking and well-known differences. The noble gases (He, Ne, Ar, Kr, Xe) are highly depleted in CI chondrites by factors ranging from $>10^4$ (Xe) to $>10^9$ (He, Ne), while the other highly volatile gases H, C, N, and O are depleted by factors of 10^4, 10, 40, and 2, respectively.

The solar photospheric Li abundance is a factor of almost 200 lower than in CI chondrites due to nuclear processing in the Sun, much more than predicted by standard solar models. It implies additional mixing below the solar convection zone, bringing gas down to high enough temperatures ($\approx 2.5 \cdot 10^6$ K) for nuclear destruction to take place and subsequently returning it to the convection zone (e.g., Charbonnel & Talon 2005). Several possible physical processes for this mixing have been proposed (e.g., internal gravity waves, rotation, convective overshooting, and atomic diffusion or a combination thereof), but all available modelling still requires parametrisation and hence remains uncertain. Solar twins show a slow and monotonically increasing Li depletion with age (Carlos et al. 2019), with the Sun being unusually deficient in Li by ≈ 0.3 dex given its age for reasons not yet understood. There is a long and chequered history surrounding the question of whether Li depletion in the Sun and similar stars is related to planet formation (e.g., Bouvier 2008; Israelian et al. 2009; Baumann et al. 2010; Baraffe & Chabrier 2010).

Given the existence of additional mixing below the convection zone as evident from Li, the photospheric abundances of Be and B take on particular importance, since they burn at slightly higher temperatures than Li ($\approx 3.5 \cdot 10^6$ K and $\approx 5 \cdot 10^6$ K, respectively). The fact that solar twins spanning a wide age

---

[11] Orgueil is the largest CI chondrite weighing in at 14 kg, followed by Alais (6 kg) and Ivuna (0.7 kg). In comparison, the Tonk (8 g) and Revelstoke (1 g) meteorites are tiny, and as a result very few mass spectroscopic analyses have been undertaken on them.

[12] Large CI chondrites such as Orgueil do display some heterogeneity due to parent body redistribution of elements, which contributes significantly to the statistical uncertainties of the meteoritic abundances (Palme et al. 2014).
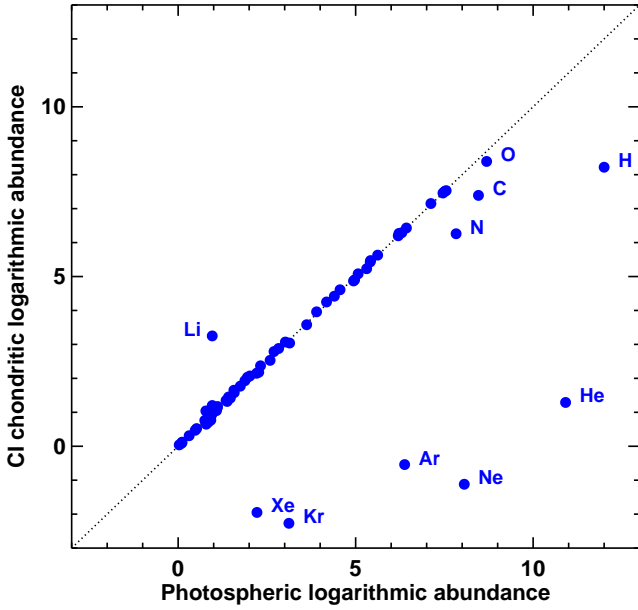
Fig. 4. Comparison between our recommended abundances in present-day solar photosphere and CI chondrites. Most elements agree well, with the exception of the highly volatile elements, which are depleted in meteorites, and Li, which has been largely destroyed in the Sun due to nuclear burning.
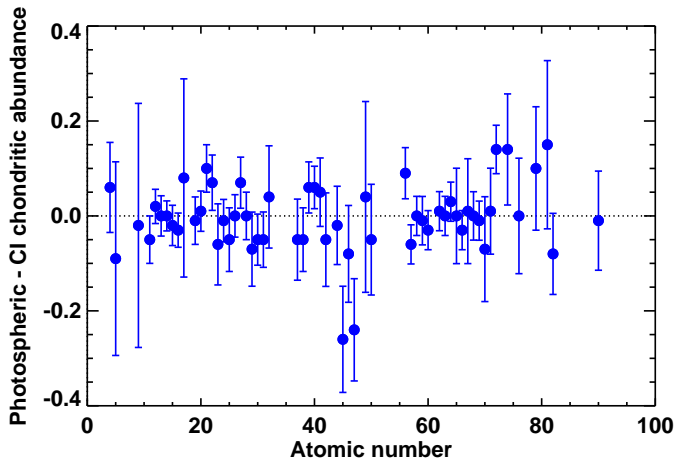

Fig. 5. Differences of the photospheric and CI chondritic logarithmic abundances as functions of atomic number. In most cases, the elemental abundances agree within the combined uncertainties; the highly volatile elements and Li are not shown in the figure due to meteoritic and solar depletion, respectively. The two most discrepant elements are Rh and Ag, both of which are suspected to have underestimated photospheric abundances in the absence of non-LTE calculations.

range all have very similar photospheric Be abundances suggests that the Sun has not experienced significant Be depletion in the convection zone, even though the solar Be abundance is perhaps ≈0.05 dex lower than expected for its age (Tucci Maia et al. 2015). A modest B deficiency could, in principle, be hidden within the large error bars, but the absence of a significant Be depletion argues against it. The photospheric Li, Be, and B abundances imply shallow extra mixing below the convection zone present over Gyr timescales in the Sun.

A more detailed comparison of the photospheric and CI chondritic abundances as a function of atomic number is shown in Fig. 5. With the exception of the depleted elements mentioned above, essentially all elements agree within their combined uncertainties. Using the inverse of the combined photospheric and meteoritic abundance uncertainties in quadrature as weights, the mean average difference of the 58 non-depleted elements (i.e. excluding Li and the highly volatiles) amounts to 0.000 ± 0.007 (s.d.= 0.052) dex. We remind the reader that the meteoritic abundance scale has been normalised to the photospheric Si abundance, which is here only quoted to within 0.01 dex, and hence this perfect agreement is somewhat fortuitous. This comparison does, however, support our choice of transition probabilities for Si (Sect. 2.4). Likewise, it is noted that atomic diffusion and gravitational settling taking place in the Sun over the past 4.57 Gyr will retain this overall agreement since all elements bar H and He diffuse in nearly identical amounts (Sect. 5). Of these 58 elements, four are nominal $>2\sigma$ outliers: Sc, Rh, Ag, and Hf; we suspect that the photospheric abundances from the minority ionisation stages Rh I and Ag I to have been significantly underestimated in the absence of non-LTE calculations (Sect. 2.6). Overall, CI chondrites closely resemble the solar photospheric abundances, justifying their historical use as a compositional proxy. Caveats are in place, however, as discussed below.

3.3. Chemical signatures of planet formation

The overall impressive consistency between the CI chondrites and the solar photosphere notwithstanding, it is worthwhile to ask whether the two abundance sets are truly the same. Or in other words, are CI chondrites a true reflection of the pristine chemical composition of the proto-solar nebula as has long been assumed (e.g. Suess & Urey 1956)? Figure 6 shows the differences between the photospheric and the CI meteoritic logarithmic abundances as a function of 50% equilibrium condensation temperature ($T_{\rm cond}$) computed for solar composition gas at a pressure of 10^{-4} bar (Wood et al. 2019, see also Lodders 2003); for clarity, only elements with a combined abundance uncertainty of <0.10 dex are included. With the anchoring of the two abundance scales through Si ($T_{\rm cond}$ = 1314 K), it appears as though the moderately volatile elements (300 ≲ $T_{\rm cond}$ ≲ 1250 K; here: Pb, S, Zn, Rb, K, Ga, Cu, Na, Mn, in order of increasing $T_{\rm cond}$) are enriched in the CI chondrites relative to the Sun: the weighted mean difference is -0.042 ± 0.006 (s.d.= 0.018) dex. Not surprisingly, the main component elements (1250 ≲ $T_{\rm cond}$ ≲ 1370 K; here: Mg, P, Si, Cr, V, Fe, Co, Ni) agree excellently, due to the fact that we enforced the Si abundances to agree: $+0.004 \pm 0.009$ (s.d.= 0.025) dex. The refractory elements ($T_{\rm cond}$ ≳ 1370 K, here 24 elements) may be slightly depleted in CI chondrites, but the relatively large scatter prevents a firm conclusion: $+0.015 \pm 0.010$ (s.d.= 0.048) dex. We caution that the absolute level of enhancement/depletion depends on the chosen reference element. It is well known that the CI chondrites are volatile rich compared to the other carbonaceous chondrites, but here we thus find evidence that this is also the case in comparison to the Sun. The opposite is of course true for the highly volatile ($T_{\rm cond}$ ≲ 250 K) elements (H, He, C, N, O, Ne, Ar, Xe, Kr), which are greatly depleted in all meteorites, including the CI chondrites (Sect. 3.1). This disposition for volatiles and refractories in the Sun and CI chondrites was first noticed by Gonzalez (1997) when discussing the metal-richness of the first discovered exoplanet host stars, and it is here substantiated by our more accurate photospheric abundances.

There is significant scatter in Fig. 6 around any possible trend, mostly driven by the photospheric abundance uncertainties; higher precision is naturally obtained when instead
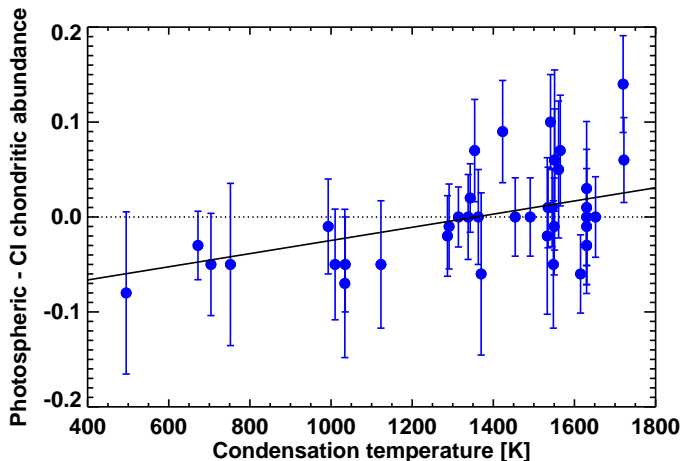
Fig. 6. Differences of the photospheric and CI chondritic logarithmic abundances as a function of 50% condensation temperature at a pressure of 10^{-4} bar for a solar composition gas (Wood et al. 2019), showing a tendency for the refractory elements to be enhanced in the Sun compared with the meteorites. Only elements with a combined uncertainty of <0.1 dex in the abundance difference are shown in the figure. It should be noted that C, N, and O (condensation temperature <200 K) fall outside the plot with the meteoritic abundances depleted compared to the Sun, as is also the case for the noble gases. The solid line is a weighted least-squares fit to the data with a slope of $(6.9 \pm 2.7) \cdot 10^{-5}$ dex K^{-1}.

intercomparing relative abundances of similar objects analysed homogeneously, such as solar/stellar twins or chondrites. A weighted linear least-squares fit implies $\Delta \log \epsilon = (6.9 \pm 2.7) \cdot 10^{-5} T_{\text{cond}} + (-0.09 \pm 0.04)$, and hence the correlation does not quite reach 3σ significance; with the condensation temperatures of Lodders (2003), the slope would be $(7.3 \pm 2.6) \cdot 10^{-5}$ dex K^{-1}. Including all elements except Li and the highly volatile elements hardly changes the best fit. The quality of the current abundance data does not motivate a more sophisticated function, such as piece-wise linear and step functions, as attempted in related cases involving dust condensation (e.g., Meléndez et al. 2009; Gonzalez 2014).

Compared to CI chondrites, other types of carbonaceous chondrites show increasing fractionation with condensation temperature (CI→CM→CR→CO→CV→CB→CH, Wasson & Kallemeyn 1988; Krot et al. 2014). Since Palme et al. (2014) did not provide data for other classes of chondrites, we made use of the published abundances by Bland et al. (2005) for 42 elements, re-normalised and converted to the astronomical logarithmic abundance scale. An advantage with the Bland et al. (2005) dataset is that they tabulate the compositions both for the bulk of the chondritic material as well as the fine-grained matrix of the meteorites, which are important for our discussion below. The abundances for other chondrite classes are given normalised to CI (and the element Yb). While the relative Si abundances are provided for the matrix components, they are missing for the bulk material for non-CI chondrites for reasons unclear to us. As a result, when comparing the bulk compositions we have had to normalise to the astronomical abundance scale using Mg as the reference element, which introduces a 0.02 dex shift; as will become clear, this minor offset is unimportant for our conclusions.

The resulting CI abundances from Bland et al. (2005) are not identical to those adopted in Sect. 3.1, but the differences are in most cases minor, as seen in Fig. 7. Importantly, the correla-
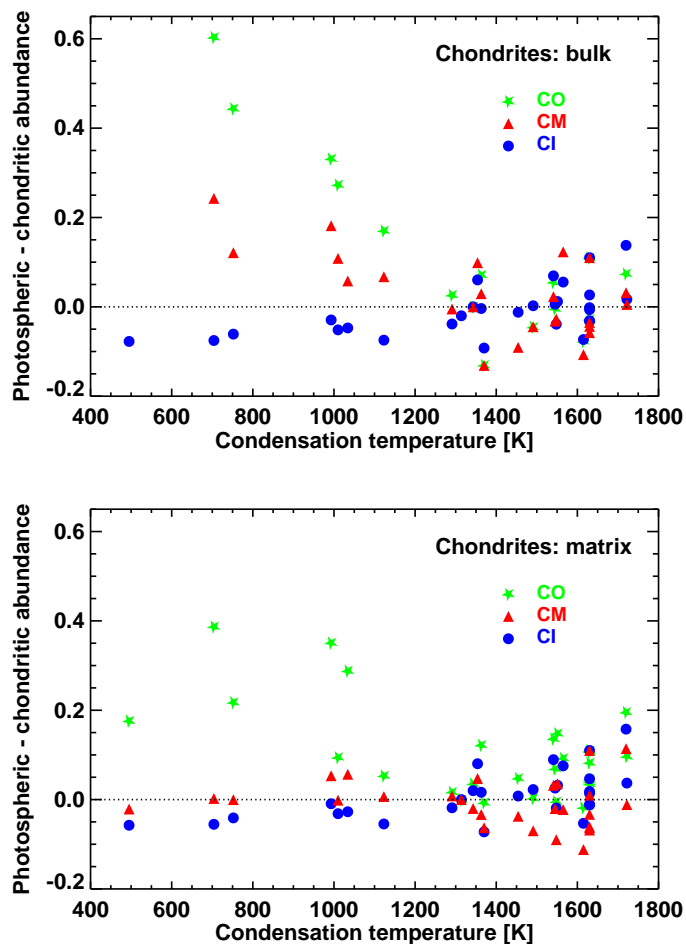

Fig. 7. *Upper panel:* difference between the solar photospheric and bulk abundances for CI (blue circles), CM (red triangles), and CO (green stars) chondrites as measured by Bland et al. (2005). CM and CO chondrites show increasing fractionation compared to the Sun, especially for the volatile elements. *Lower panel:* same, but for the fine-grained matrix of chondrites. Surprisingly, the solar abundances more closely resemble the CM matrix than the CI equivalent, which shows a trend with condensation temperature. As explained in the text, for the bulk comparison Mg has been used as the reference element to connect the meteoritic and photospheric abundance scales since the Si abundances are not provided by Bland et al. (2005) for non-CI chondrite classes, which introduces a 0.02 dex offset. For the matrix compositions, the usual reference element Si has been used.

tion with condensation temperature is still apparent even if data for some elements, including the moderately volatile Na and S, are lacking; the weighted difference between the Sun and the Bland et al. (2005) CI data for the moderately volatile elements is -0.040 ± 0.007 (s.d. = 0.018) dex, which is almost identical to the case with the Palme et al. (2014) CI abundances adopted elsewhere in our study. In terms of their bulk abundances, the CI chondrites are clearly the most solar-like, the trend with condensation temperature notwithstanding, followed by the CM and CO meteorites, which show increasing depletion of the volatile elements, while the refractory elements display less of a variation relative to the Sun and CI (Fig. 7); the highly volatile elements (H, C, N, O, and noble gases) not included in the figure are even more depleted in the non-CI chondrites.

An important distinction between the chondrite classes is that CI meteorites are only comprised of the fine-grained matrix, while other chondrites also consist of chondrules and refractory

inclusions with a volatile-depleted/refractory-enriched composition relative to their matrices; the fraction of matrix material varies between the classes as well as between meteorites of the same type. Chondrules have experienced rapid heating to temperatures >1400 K, followed by similarly quick cooling, likely in the inner part of the proto-planetary disc, but the details of their formation and subsequent incorporation into the matrix is still hotly debated; the matrix material has not experienced any significant heating events. The chemical complementarity between the chondrules and matrix that has been previously argued for (e.g., Bland et al. 2005; Palme & Hezel 2011) has more recently been questioned, implying that the chondrules and matrix did not necessarily form from the same reservoir (van Kooten et al. 2019; Alexander 2019). To facilitate a fair comparison with the solar abundances, one should therefore consider the chondritic matrices, which are clearly more pristine than the chondrules, rather than their bulk compositions.

The lower panel of Fig. 7 compares the matrix compositions of CI, CM, and CO chondrites relative to the Sun using data from Bland et al. (2005). Since the chondritic matrix contains a higher abundance of volatile elements than chondrules, the matrices are more similar to the Sun. Remarkably, the CM matrix is overall a very good match to the present-day solar photosphere, closer in fact than the CI chondrites. In particular, the moderately volatile elements agree better with a weighted mean difference of +0.014 ± 0.010 (s.d.= 0.027) dex, while the refractory elements show similar differences for CI and CM matrix although of opposite sign; in both cases, the main component elements agree excellently with the Sun. The weighted linear least-squares fit for the CM matrix data has a slope of $(-4.6 \pm 3.6) \cdot 10^{-5}$ dex K^{-1}, while the corresponding slope for CI chondrites is $(8.6 \pm 3.6) \cdot 10^{-5}$ dex K^{-1} with the Bland et al. (2005) elemental abundances. We conclude that CI chondrites are not a perfect compositional match with the Sun, as has been assumed for more than half a century. Instead, the solar abundances more closely resemble those of the matrices of CM chondrites, although not the bulk CM composition. This could reflect spatially separate origins of the CM matrix and chondrules with differing chemical make-up, with some chemical complementarity possibly emerging later following transport to where amalgamation occur (van Kooten et al. 2019). A more detailed comparison will be required to elucidate how, where and when the different chondrite constituents formed and their relation to the solar composition in this new scenario (e.g., Scott 2007; Alexander 2019; van Kooten et al. 2019). In the meantime, we advise against using meteoritic abundances to estimate the Solar System composition, which is often done due to their generally higher precision (e.g., Vinyoles et al. 2017; Lodders 2019; Wang et al. 2019).

The correlations with chondrites shown in Fig. 7 are reminiscent of the peculiar solar abundances relative to solar twins; the Sun is unusually volatile rich and refractory poor with an abundance amplitude of about 0.08 dex (Meléndez et al. 2009; Ramírez et al. 2010). In other words, the abundance differences relative to the average of solar twins is almost exactly a mirror image of the differences with the CI chondrites. Only ≈10% of the studied stars share the detailed chemical fingerprint with the Sun, which furthermore cannot be explained by differences in age or Galactic birthplace of the stars (Bedell et al. 2018; Nissen & Gustafsson 2018). The correlation with condensation temperature suggests that the signature is related to planet formation. The initial suggestion that the abundance pattern is imprinted by the formation of terrestrial planets in the Solar System (Meléndez et al. 2009; Chambers 2010) is likely not cor-

rect since the solar convection zone was much deeper during the proto-planetary disc phase compared to today, thus requiring much more than a few M$_\oplus$ of refractory-rich material locked up in rocky planets. Furthermore, transit data from Kepler imply that most solar-like stars harbour super-Earths or mini-Neptunes more massive than the terrestrial planets in the Solar System (Zink et al. 2019), which would make the Sun stand out in the opposite manner compositionally. The alternative explanation that other stars have on average experienced more accretion of rocky planets is also unlikely to hold up due to the rapid erasure of such metal-rich accretion from the stellar surface convection zone due to thermohaline mixing (Théado & Vauclair 2012).

Recently, a more promising scenario was proposed by Booth & Owen (2020), which involves the early formation of giant planets trapping >100 $M_\oplus$ of refractory-rich dust external to their orbits while volatile-rich gas continues to accrete onto the proto-star. They found that such gas-dust separation could imprint an abundance pattern similar to that observed when the Sun is deficient in refractory elements by ≈0.08 dex (20%). The prediction is thus that most solar twins lack a gas giant planet, allowing the gas and dust accretion to continue largely unimpeded. The incidence of the peculiar solar abundance pattern is consistent with the frequency of giant planets being ≈7% (Wittenmyer et al. 2020). Long-term precision radial velocity monitoring of both stars most similar and most chemically disparate to the Sun should be undertaken to search for Jupiter-like planets; HIP11915 is also a chemically solar twin that hosts a Jupiter twin (Yana Galarza et al. 2021), although the planet hosts HIP5301 and HIP15227 seemingly do not fit the pattern (Bedell et al. 2018) – a much larger sample is obviously needed. The connection with the chondritic compositions discussed above also needs to be deciphered within the framework of an early formation of Jupiter.

4. Isotopic abundances

Isotopic abundances can only be measured from solar spectroscopy for C and O, and even then only with significant uncertainties (Scott et al. 2006; Ayres et al. 2013; Lyons et al. 2018)[13]. Instead, alternative methods are used to infer the solar values, including sample return missions of the solar wind such as NASA's Genesis probe (Burnett et al. 2003; Jurewicz et al. 2003) and laboratory measurements of various terrestrial, lunar, meteoritic, cometary, and asteroid samples. Our advocated isotopic abundances can be found in Table B.1.

The present-day solar D abundance can not be directly determined due to near-complete burning of D to ^{3}He during the pre-main-sequence evolution. The increase from the proto-solar ^{3}He/^{4}He ratio as indicated by the value measured in Jupiter $(1.66 \pm 0.05 \cdot 10^{-4}$, Mahaffy et al. 1998) and the local interstellar cloud $(1.62 \pm 0.29 \cdot 10^{-4}$, Busemann et al. 2006), to the present-day ratio in the solar wind is thus a reflection of the proto-solar D/H ratio. The isotope fluences determined from the Genesis probe suggest ^{3}He/^{4}He$= (4.5 - 4.8) \cdot 10^{-4}$ depending on the solar wind regime (Heber et al. 2012), which indicates the presence of isotopic fractionation during the formation and acceleration of the solar wind. Two methods to account for fractionation are presented in Heber et al. (2012): theoretical corrections based on the inefficient Coulomb drag model or those based on empirical correlations between ^{3}He/^{4}He and

---

[13] The Li I 670.8 nm line in the Sun is unfortunately too weak to facilitate a determination of the photospheric ^{6}Li/^{7}Li isotopic ratio, as has been possible in some stars (e.g., Lind et al. 2013; Mott et al. 2017).
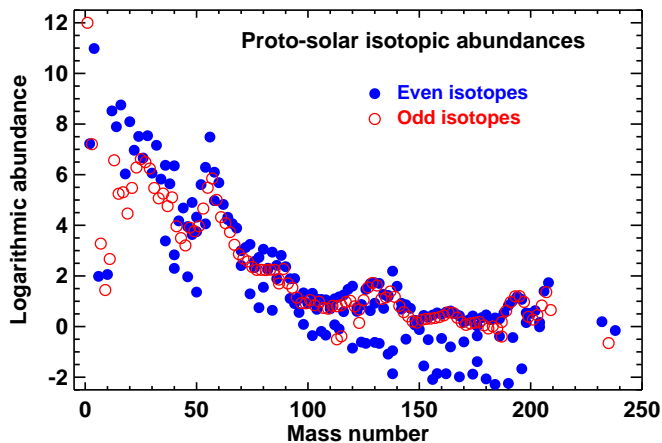
Fig. 8. Proto-solar isotopic abundances as a function of mass number after taking into account atomic diffusion for He (+0.07 dex) and heavier elements (+0.06 dex) and radioactive decay. Even isotopes are shown as filled blue circles and odd isotopes as open red circles.

H/^{4}He in the solar wind, which is similar to our determination of the solar Ne and Ar absolute abundances. Substantially different present-day ^{3}He/^{4}He ratios and thus proto-solar D/H abundances are obtained: $1.24 \cdot 10^{-5}$ (theoretical) and $1.67 \cdot 10^{-5}$ (empirical). We take the average of the two values together with the Jovian D/H ($2.1 \cdot 10^{-5}$, Lellouch et al. 2001) to obtain a proto-solar D/H ratio of $(1.67 \pm 0.25) \cdot 10^{-5}$. We caution that the here-derived proto-solar D/H value is in contradiction with the present-day D abundance in the local interstellar medium of D/H$\geq (2.0 \pm 0.1) \cdot 10^{-5}$ (Linsky et al. 2006; Prodanović et al. 2010) since astration of D in stars should result in a monotonic decrease with time. The here-deduced proto-solar D would also lead to uncomfortably large astration factors from the primordial value of $(2.53 \pm 0.03) \cdot 10^{-5}$ as inferred from high-redshift, metal-poor damped Ly-alpha systems (Weinberg 2017; Cooke et al. 2018). The proto-solar D/H isotopic ratio clearly deserves further scrutiny.

The ^{12}C/^{13}C ratio does not appear to vary significantly between different Solar System objects. We therefore adopt the reference terrestrial value of 89.3 ± 0.2 (Meija et al. 2016b), which is consistent with the solar photospheric determination (Scott et al. 2006; Lyons et al. 2018) and the preliminary Genesis results for the solar wind (Wiens et al. 2013).

The ^{14}N/^{15}N ratio varies tremendously between Solar System sources for reasons that are still poorly understood. The Genesis team has measured the isotopic ratio in the solar wind (Marty et al. 2010), which with an isotopic fractionation correction (Laming et al. 2017) implies ^{14}N/^{15}N= 453 ± 66. A similar value, 435 ± 57, is obtained for Jupiter (Owen et al. 2001). We take the weighted mean of these two measurements: ^{14}N/^{15}N= 443 ± 13.

The isotopic composition of O in the solar wind was measured by McKeegan et al. (2011) using the Genesis sample return mission. After correction for isotopic fractionation in the solar wind, they estimated solar isotopic ratios of ^{16}O/^{18}O= 530 and ^{16}O/^{17}O= 2798, which we adopt here. The most recent spectroscopic analyses of CO lines in the Sun with 3D atmosphere models are consistent with these ratios, albeit with relatively large uncertainties (Lyons et al. 2018). Like almost all rocky material in the inner Solar System, the Earth is enriched in ^{18}O and ^{17}O in comparison to ^{16}O (isotopic ratios of 499 and 2632, respectively, Meija et al. 2016b), likely as a result of CO

self-shielding during the proto-planetary disc phase of the Solar System's formation (Clayton 2002; McKeegan et al. 2011).

Genesis solar wind data also allow the isotopic abundances of the other noble gases Ne, Ar, Kr, and Xe to be determined. For Ne and Ar, the isotopic fractionations are significantly smaller than for He, while for Kr and Xe they can be neglected altogether (Heber et al. 2012). Using the empirical correlations to correct for the fractionation, the present-day solar isotopic ratios are ^{20}Ne/^{22}Ne= 13.36 ± 0.09, ^{21}Ne/^{22}Ne= 0.0324, and ^{36}Ar/^{38}Ar= 5.37 ± 0.03 (Heber et al. 2012; Meshik et al. 2014); almost identical values are obtained with the inefficient Coulomb drag theoretical model (Bodmer & Bochsler 2000). To our knowledge, the ^{36}Ar/^{40}Ar ratio has not been determined from the Genesis samples and hence the proto-solar ^{40}Ar abundance is highly uncertain (Anders & Grevesse 1989); the terrestrial abundance is completely dominated by the radioactive decay of ^{40}K (Meija et al. 2016b), making it the most abundant isotope. For Kr and Xe, we embrace the Genesis results from Meshik et al. (2014) and Meshik et al. (2020), respectively.

For the non-volatile elements, the Genesis solar wind samples have not yet delivered final isotopic abundances, although this should be feasible for elements like Mg, Si, S, and Fe in due course (Burnett et al. 2019). Mg is particularly interesting since it enables a critical test of the solar wind isotopic fractionation models (e.g., Bodmer & Bochsler 2000; Laming et al. 2017), which are in reasonable agreement with the most recent Genesis results (Jurewicz et al. 2020). Fe isotopic measurements of the Genesis data on the other hand would test the notion of a chemically homogeneous proto-solar nebula, that is, whether the Sun and, for example, the most chemically pristine meteorites are expected to have identical composition as normally assumed (Sect. 3).

For the elements not discussed above, we take the present-day relative isotopic fractions from the recommendations by the International Union of Pure and Applied Chemistry (Meija et al. 2016b with subsequent updates for Yb, Ta, Ir, and Hf[14]) for representative terrestrial samples (the mean when a range is given). The proto-solar isotopic fractions given in Table B.1 are assumed to be the same as the present-day values, with the exception of radioactive elements and their daughter products; we adopt the recommended isotopic half-lives from IAEA Nuclear Data Services[15] and a Solar System age of 4.568 Gyr (Bouvier & Wadhwa 2010; Connelly et al. 2012).

5. Present-day and proto-solar Solar System abundances

With the Sun providing >99.85% of the total mass in the Solar System, we can safely adopt the solar abundances as the basis of the chemical composition of the solar system overall. The present-day photospheric elemental abundances, however, are not the same the Sun was born with due to three main effects: nuclear processing, radio-active decay, and diffusion. The first effect only impacts Li (and possibly Be), which has been largely destroyed in the convection zone, as is evident from the comparison with the most pristine meteorites (Sect. 3.2). No nuclear products from H-burning in the solar core have reached the solar surface layers, with the exception of D-burning in the deep convection zone during the pre-main sequence (Sect. 4). Secondly, elements such as Th and U are radioactively unstable,

---

[14] https://www.ciaaw.org/isotopic-abundances.htm
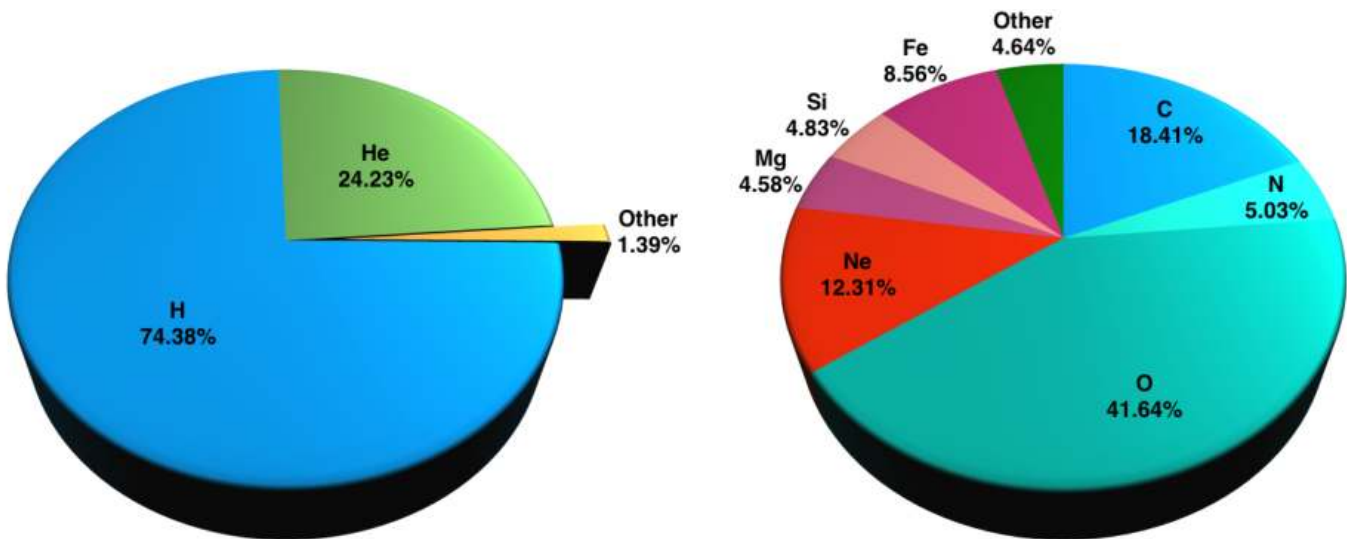[15] https://www-nds.iaea.org/relnsd/NdsEnsdf/QueryForm.html

Fig. 9. Present-day photospheric mass fractions the most abundant elements. *Left panel:* mass fractions of H, He, and heavy elements. *Right panel:* relative mass fractions of the most abundant heavy elements with the highly volatile C, N, O, and Ne contributing more than 77% of all heavy elements by mass.

and hence their proto-solar abundances 4.57 Gyr ago were larger than measured today; as noted in Sect. 4, we account for this using the recommended half-lives. Finally, all elements heavier than H have partly settled from the surface convection zone to the radiative interior from the combined effects of microscopic thermal diffusion, gravitational settling, and radiative acceleration, normally together referred to as atomic diffusion (Thoul et al. 1994).

Quantitative predictions for elemental diffusion are hampered by the possibility of additional mixing below the convection zone due to still poorly understood processes like convective overshooting, rotation, internal gravity waves, and turbulence (e.g., Goldreich & Schubert 1967; Chaboyer et al. 1995; Baraffe et al. 2017; Aerts et al. 2019; Dumont et al. 2021), which is required to explain the solar Li abundance and interior rotation profile. Different groups thus require slightly varying proto-solar abundances depending on the ingredients of their stellar evolution codes when calibrating to the solar luminosity, effective temperature and surface composition at the solar age. Here we adopt the predictions from the standard solar model of Vinyoles et al. (2017) computed with the Asplund et al. (2009) chemical composition. In terms of number densities relative to H, the proto-solar He abundance is higher by 0.070 dex compared with the present-day photospheric value, while for all heavier elements the difference is 0.064 dex. Because the Vinyoles et al. (2017) solar model does not include any additional mixing beyond atomic diffusion as required to explain the solar Li depletion, these diffusion corrections may be slightly over-estimated; more recent solar models which simultaneously agree better with the Li depletion and helioseismology (see below) have diffusion abundance corrections about half of this: ≈0.03 dex for all elements other than H (Eggenberger et al. 2021).

Regarding elements for which no photospheric abundance determination is feasible from spectroscopy or solar wind measurements (Table 2), we base their present-day photospheric abundances on the CI chondritic abundances. Those are first corrected for the trend in abundance difference with condensation temperature (Fig. 6, Sect. 3.3) before applying the effects of atomic diffusion to compute the proto-solar abundances. The proto-solar isotopic abundances are given in Table B.1.

In terms of mass fractions of H, He, and heavy elements, the elemental abundances presented in Table 2 correspond to present-day photospheric values of $X_{surface} = 0.7438 \pm 0.0054$, $Y_{surface} = 0.2423 \pm 0.0054$, $Z_{surface} = 0.0139 \pm 0.0006$, and $Z_{surface}/X_{surface} = 0.0187 \pm 0.0009$; Fig. 9 illustrates the present-day photospheric mass fractions of the most abundant elements. The quoted uncertainty on $Y_{surface}$ stems from the helioseismic determination (Sect. 2.8), while for the heavier elements we assumed that their abundance errors to be independent. The here inferred solar surface metallicity is slightly higher than (but within the uncertainties of) the value ($Z_{surface} = 0.0134$) derived in Asplund et al. (2009), mainly as a result of the revised Ne abundance following the adoption of the Genesis solar wind measurements (Sect. 2.8). With the Vinyoles et al. (2017) solar model for atomic diffusion, the proto-solar mass fractions would be $X_{initial} = 0.7121$, $Y_{initial} = 0.2725$, and $Z_{initial} = 0.0154$, while with a smaller abundance correction of 0.03 dex for all elements heavier than H (Eggenberger et al. 2021) the values are $X_{initial} = 0.7304$, $Y_{initial} = 0.2550$, and $Z_{initial} = 0.0146$. Table 4 lists the inferred present-day photospheric and proto-solar mass fractions based on some widely used compilations of the solar chemical composition over the past three decades.

6. Solar abundances, standard solar models, and helioseismology

Care must be exercised when interpreting proto-solar mass fractions in light of the long-standing and exasperating discrepancy between helioseismology and predictions from standard solar models constructed with present-day surface abundances similar to those presented here: the so-called solar modelling problem[16] (e.g., Basu & Antia 2004; Bahcall et al. 2005; Vinyoles et al. 2017; Christensen-Dalsgaard 2021). In particular, the comparatively low photospheric C, N, and O abundances (and associated Ne abundance) from 3D-based spectroscopic analyses (e.g., Allende Prieto et al. 2001b, 2002; Asplund et al. 2004, 2005b, 2009; Amarsi et al. 2018a, 2019,

---

[16] While sometimes referred to as the solar abundance problem, we argue that this is a misnomer since it is not at all clear that the solar composition is at fault.

Table 4. Present-day photospheric and proto-solar mass fractions of hydrogen (X), helium (Y), and metals (Z) for a number of widely used compilations of the solar chemical composition.

Source	Present-day photospheric				Proto-solar			
	X_{surface}	Y_{surface}	Z_{surface}	$Z_{\text{surface}}/X_{\text{surface}}$	X_{initial}	Y_{initial}	Z_{initial}	$Z_{\text{initial}}/X_{\text{initial}}$
Present work	0.7438	0.2423	0.0139	0.0187	0.7121	0.2725	0.0154	0.0216
Lodders 2019	0.7389	0.2463	0.0148	0.0200	0.7061	0.2766	0.0173	0.0245
Caffau et al. 2011 [a]	0.7321	0.2526	0.0153	0.0209				
Asplund et al. 2009	0.7381	0.2485	0.0134	0.0181	0.7154	0.2703	0.0142	0.0199
Lodders et al. 2009	0.7390	0.2469	0.0141	0.0191	0.7112	0.2735	0.0153	0.0215
Asplund et al. 2005a	0.7392	0.2485	0.0122	0.0165	0.7166	0.2704	0.0130	0.0181
Lodders 2003	0.7491	0.2377	0.0133	0.0177	0.7111	0.2741	0.0149	0.0210
Grevesse & Sauval 1998	0.7347	0.2483	0.0169	0.0231	0.7062	0.2750	0.0188	0.0266
Grevesse et al. 1993	0.7028	0.2800	0.0172	0.0245				
Anders & Grevesse 1989	0.7065	0.2741	0.0194	0.0274				

Notes. [a]Caffau et al. (2011) determined the abundances of Li, C, N, O, P, S, K, Fe, Eu, Hf, Os, and Th and adopted the recommended values of Lodders et al. (2009) for all other elements. They did not quote any proto-solar mass fractions.

2020) have ruined the good agreements with helioseismology that were obtained with global solar models computed with the older higher solar metallicity (e.g., Anders & Grevesse 1989: $Z_{\text{surface}}/X_{\text{surface}} = 0.274$; Grevesse et al. 1993: $Z_{\text{surface}}/X_{\text{surface}} = 0.246$; Grevesse & Sauval 1998: $Z_{\text{surface}}/X_{\text{surface}} = 0.231$). The predicted surface He abundance, depth of the convection zone, and the sound speed as a function of solar radius from a solar calibration are now significantly more discrepant compared to the inversion of the observed solar p-mode oscillation frequencies; the solar surface composition presented here goes in the right direction but will not resolve the mismatch. We note, however, that the available seismic data in fact favours a low metallicity ($Z_{\text{surface}} < 0.014$) in the convection zone (Vorontsov et al. 2013; Buldgen et al. 2017), suggesting that current standard solar models are missing important physics or are constructed with faulty input data in the radiative zone below the convection zone.

A huge body of work has been devoted to reconciling the spectroscopic and interior solar models triggered by our 3D-based solar abundances over the past two decades. Arguably the most straightforward explanation would be underestimated opacities, especially near the bottom of the convection zone where the discrepancies are most acute, to compensate for the lowering of the abundances of the dominant elements. It would require the computed data sets of atomic opacities (e.g., Badnell et al. 2005; Mondet et al. 2015; Colgan et al. 2016) all to be underestimated by about 20% in the relevant temperature-pressure regime (Serenelli et al. 2009; Christensen-Dalsgaard et al. 2009). In fact recent experimental opacity measurements are systematically higher than calculations with the missing opacity for Fe alone accounting for about half of what is required to resolve the solar modelling problem (Bailey et al. 2015; Nagayama et al. 2019). With new experiments and updated calculations with previously overlooked atomic processes underway (e.g., Nahar & Pradhan 2016; Krief et al. 2018) it remains to be seen whether the final atomic opacities will be sufficient. Important independent constraints on the solar interior composition will also come from measurements of the solar neutrino fluxes, especially those produced in the CNO-cycle that were recently reported by the Borexino experiment (Borexino Collaboration 2020). Finally, encouraging signs are appearing from new solar models with improved mixing below the convection zone aimed at explaining the depletion of Li and the interior rotation profile, which standard models cannot do (e.g., Yang 2019; Zhang et al. 2019; Buldgen et al.

2019a,b; Eggenberger et al. 2021). We remain cautiously optimistic that the persistent solar modelling problem will soon have been resolved without necessitating any major revision of the photospheric solar abundances presented here.

7. Concluding remarks

The elemental abundances derived and presented here are a further stepping stone towards the advancement of our understanding of the solar chemical composition, which is of such crucial importance for astronomy as a whole. As demonstrated above, major improvements in terms of the solar spectroscopic analysis have been accomplished, which should make the inferred elemental abundances both more precise and more accurate. It is now perfectly feasible to perform detailed 3D non-LTE line formation calculations using highly realistic 3D radiative-hydrodynamical simulations of the solar surface convection and atmosphere. This has been achieved for 13 elements – Li, C, N, O, Na, Mg, Al, Si, K, Ca, Mn, Fe, and Ba – all using comprehensive model atoms with reliable atomic data, including the previously notoriously uncertain cross-sections for H collisions. Compared to Asplund et al. (2009), in which only the abundances of Li and O were based on a consistent 3D non-LTE analysis, this certainly represents substantial progress. The abundances of a further 45 elements have been determined on the basis of a 3D LTE spectroscopic analysis. In total, we present the solar photospheric abundances of 68 elements when also including the noble gases, for which helioseismic and solar wind measurements are available, and four trace elements evaluated from sunspot observations. Importantly, the abundance uncertainties for these 68 elements have been carefully evaluated, including both statistical and systematic uncertainties. These have been augmented with meteoritic data (corrected for an identified trend with condensation temperature) for a further 15 elements, thus providing Solar System abundances for all 83 long-lived elements.

Based on our state-of-the-art 3D non-LTE analysis, we can safely confirm that the old high solar metallicity of, for example, Grevesse et al. (1993) and Grevesse & Sauval (1998), which are still used to construct standard solar models, should finally be discarded – there are simply no arguments in favour of those outdated 1D LTE results spectroscopically. Our study is, however, definitely not the final word on the issue of the solar

chemical composition, with much work remaining to reach comparable abundance precision to that of the most pristine meteorites. Arguably, the most pressing need is to extend non-LTE calculations to additional elements: only 26 elements have their solar abundances determined from a non-LTE analysis, half of which are only in 1D. Of particularly high priority is to carry out 3D non-LTE computations for the remaining Fe-peak elements (including revisiting the important case of Mn, Sect. 2.5) as well as other elements of key astronomical significance, such as Be (to constrain solar depletion, Sect. 3.2), S, Zn, Rb (volatile elements to confirm differences with CI chondrites, Sect. 3.3), P, Cu, and Sr (stellar nucleosynthesis yields, Kobayashi et al. 2020). Several of these elements already show substantial non-LTE effects in existing 1D non-LTE calculations, which can be expected to be amplified in 3D.

As always, solar spectroscopy is reliant on having access to accurate atomic data. Over the past decade, the situation regarding experimental transition probabilities has improved significantly for the Fe-peak elements in particular, thanks to the dedicated and valiant efforts by a relatively small group of atomic physicists around the world, as discussed in Sect. 2.5. Several other elements have also seen significant updates, however, the need for further work is essentially endless. Here it suffices to mention the case of Si, the element anchoring the meteoritic abundance scale to the solar photospheric values (Sect. 2.4). Besides the need for refined transition probabilities of spectral lines used as diagnostics, there is also a demand for more and better atomic data for lines blending the primary abundance indicators. Since those lines are typically weaker and arise from higher-excitation levels, they are often not even properly identified or, when included in existing atomic calculations, have faulty gf-values.

For non-LTE modelling, significantly more atomic data are necessary, including all radiative (bound-bound and bound-free) and collisional (with electrons and hydrogen) transitions coupling the different atomic levels. Great progress has recently been achieved in this regard, especially related to inelastic H collisions (e.g., Barklem 2016a; Belyaev et al. 2018; Barklem et al. 2021), which has made the non-LTE results much more trustworthy. Crucially, the relevant atomic data now exist for a 3D non-LTE study for almost all of the elements highlighted above; mainly what is lacking is (wo)man-power to take on the necessary but time-consuming 3D non-LTE analyses. What has not yet been fully explored for the Sun is how departures from LTE in one element affect those of other elements or feed back onto the solar atmospheric structure; preliminary calculations suggest that this may well be of importance (Osorio et al. 2020). Furthermore, we caution that magnetic fields have not been included in the 3D solar atmosphere model employed throughout this study. While early work based on imposed vertical magnetic fields implied that the effects could be substantial (Fabbian et al. 2010), more recent 3D LTE calculations based on a 3D MHD solar model with a self-consistent small-scale magnetic dynamo (Rempel 2014) reveal that the impact on solar abundance determination is negligible (<0.01 dex) at least for C, N, O, and Fe (Shchukina & Trujillo Bueno 2015; Shchukina et al. 2016); this may not hold however for elements in which non-LTE effects are important and thus deserves further scrutiny. Similarly, there is no indication that the inclusion of a chromosphere or other magnetic activity in the solar model would significantly impact the derived abundances for the weak photospheric lines employed here using disc-centre observations of the quiet Sun (Bergemann et al. 2021).

Besides the obvious benefits from having a better definition of a widely used astronomical yardstick, the continuously improved 3D-based solar abundances reported here and in our earlier works (e.g., Asplund et al. 2005a, 2009) have uncovered two surprising peculiarities regarding the solar chemical composition, neither of which have been explained. The inconsistency between the composition at the surface, as measured from spectroscopy, and the interior, as inferred from helioseismology, has now been around for almost two decades in spite of tremendous efforts in reconciling the two with further improvements to the solar modelling. It is crucial to remember that this is not a solar problem but a stellar problem. If indeed the explanation is missing opacity as suggested by recent experiments (Sect. 6), it would imply that current stellar interior and evolution models are not fully trustworthy. Since such stellar models underpin much of the field of astronomy, it would have profound implications. The second solar abundance feature uncovered here, namely that the supposedly most primitive meteorites – the CI chondrites – and the Sun in fact do not share the same composition, implies that a revision of the earliest history of the Solar System is required, given that their equivalence has been taken for granted for more than half a century (Sect. 3.3). The existence of a similar abundance trend of the condensation temperature between the Sun and solar twins suggests that this may well give us a deeper understanding of planet formation around stars in general.

References

Abrams, M. C., Goldman, A., Gunson, M. R., Rinsland, C. P., & Zander, R. 1996, Appl. Opt., 35, 2747
Aerts, C., Mathis, S., & Rogers, T. M. 2019, ARA&A, 57, 35
Alexander, C. M. O. 2019, Geochim. Cosmochim. Acta, 254, 277
Allende Prieto, C., Barklem, P. S., Asplund, M., & Ruiz Cobo, B. 2001a, ApJ, 558, 830
Allende Prieto, C., Lambert, D. L., & Asplund, M. 2001b, ApJ, 556, L63
Allende Prieto, C., Lambert, D. L., & Asplund, M. 2002, ApJ, 573, L137
Amarsi, A. M. 2016, PhD Thesis, The Australian National University, Australia
Amarsi, A. M., & Asplund, M. 2017, MNRAS, 464, 264
Amarsi, A. M., Asplund, M., Collet, R., & Leenaarts, J. 2016a, MNRAS, 455, 3735
Amarsi, A. M., Lind, K., Asplund, M., Barklem, P. S., & Collet, R. 2016b, MNRAS, 463, 1518
Amarsi, A. M., Barklem, P. S., Asplund, M., Collet, R., & Zatsarinny, O. 2018a, A&A, 616, A89
Amarsi, A. M., Nordlander, T., Barklem, P. S., et al. 2018b, A&A, 615, A139
Amarsi, A. M., Barklem, P. S., Collet, R., Grevesse, N., & Asplund, M. 2019, A&A, 624, A111
Amarsi, A. M., Grevesse, N., Grumer, J., et al. 2020, A&A, 636, A120
Amarsi, A. M., Grevesse, N., Asplund, M., & Collet, R. 2021, A&A, in press, https://doi.org/10.1051/0004-6361/202141384
Anders, E., & Grevesse, N. 1989, Geochim. Cosmochim. Acta, 53, 197
Andersen, T., Poulsen, O., Ramanujam, P. S., & Petkov, A. P. 1975, Sol. Phys., 44, 257
Anstee, S. D., & O'Mara, B. J. 1995, MNRAS, 276, 859
Arlandini, C., Käppeler, F., Wisshak, K., et al. 1999, ApJ, 525, 886

Asplund, M. 2004, A&A, 417, 769
Asplund, M. 2005, ARA&A, 43, 481
Asplund, M., Nordlund, Å., Trampedach, R., & Stein, R. F. 1999, A&A, 346, L17
Asplund, M., Nordlund, Å., Trampedach, R., & Stein, R. F. 2000a, A&A, 359, 743
Asplund, M., Nordlund, Å., Trampedach, R., Allende Prieto, C., & Stein, R. F. 2000b, A&A, 359, 729
Asplund, M., Ludwig, H.-G., Nordlund, Å., & Stein, R. F. 2000c, A&A, 359, 669
Asplund, M., Carlsson, M., & Botnen, A. V. 2003, A&A, 399, L31
Asplund, M., Grevesse, N., Sauval, A. J., Allende Prieto, C., & Kiselman, D. 2004, A&A, 417, 751
Asplund, M., Grevesse, N., Sauval, A. J., Allende Prieto, C., & Blomme, R. 2005a, A&A, 431, 693
Asplund, M., Grevesse, N., & Sauval, A. J. 2005b, in Cosmic Abundances as Records of Stellar Evolution and Nucleosynthesis, eds. T. G. Barnes, III., & F. N. Bash, ASP Conf. Ser., 336, 25
Asplund, M., Grevesse, N., Sauval, A. J., & Scott, P. 2009, ARA&A, 47, 481
Ayres, T. R., Lyons, J. R., Ludwig, H.-G., Caffau, E., & Wedemeyer-Böhm, S. 2013, ApJ, 765, 46
Badnell, N. R., Bautista, M. A., Butler, K., et al. 2005, MNRAS, 360, 458
Bahcall, J. N., Serenelli, A. M., & Basu, S. 2005, ApJ, 621, L85
Bailey, J. E., Nagayama, T., Loisel, G. P., et al. 2015, Nature, 517, 56
Balachandran, S. C., & Bell, R. A. 1998, Nature, 392, 791
Baraffe, I., & Chabrier, G. 2010, A&A, 521, A44
Baraffe, I., Pratt, J., Goffrey, T., et al. 2017, ApJ, 845, L6
Barklem, P. S. 2016a, A&ARv, 24, 9
Barklem, P. S. 2016b, Phys. Rev. A, 93, 042705
Barklem, P. S. 2018, A&A, 612, A90
Barklem, P. S., & Collet, R. 2016, A&A, 588, A96
Barklem, P. S., & O'Mara, B. J. 1997, MNRAS, 290, 102
Barklem, P. S., O'Mara, B. J., & Ross, J. E. 1998, MNRAS, 296, 1057
Barklem, P. S., Piskunov, N., & O'Mara, B. J. 2000, A&AS, 142, 467
Barklem, P. S., Belyaev, A. K., Dickinson, A. S., & Gadéa, F. X. 2010, A&A, 519, A20
Barklem, P. S., Belyaev, A. K., Spielfiedel, A., Guitou, M., & Feautrier, N. 2012, A&A, 541, A80
Barklem, P. S., Osorio, Y., Fursa, D. V., et al. 2017, A&A, 606, A11
Barklem, P. S., Amarsi, A. M., Grumer, J., et al. 2021, ApJ, 908, 245
Barrat, J. A., Zanda, B., Moynier, F., et al. 2012, Geochim. Cosmochim. Acta, 83, 79
Basu, S. 2016, Liv. Rev. Sol. Phys., 13, 2
Basu, S., & Antia, H. M. 2004, ApJ, 606, L85
Basu, S., & Antia, H. M. 2008, Phys. Rep, 457, 217
Baumann, P., Ramírez, I., Meléndez, J., Asplund, M., & Lind, K. 2010, A&A, 519, A87
Bautista, M. A., Fivet, V., Ballance, C., et al. 2015, ApJ, 808, 174
Becker, U., Kerkhoff, H., Kwiatkowski, M., et al. 1980, Phys. Lett. A, 76, 125
Bedell, M., Bean, J. L., Meléndez, J., et al. 2018, ApJ, 865, 68
Beeck, B., Cameron, R. H., Reiners, A., & Schüssler, M. 2013, A&A, 558, A48
Bell, R. A., Balachandran, S. C., & Bautista, M. 2001, ApJ, 546, L65
Belmonte, M. T., Pickering, J. C., Ruffoni, M. P., et al. 2017, ApJ, 848, 125
Belyaev, A. K. 2013, Phys. Rev. A, 88, 052704
Belyaev, A. K., & Voronov, Y. V. 2017, A&A, 606, A106
Belyaev, A. K., & Yakovleva, S. A. 2017, A&A, 606, A147
Belyaev, A. K., Barklem, P. S., Dickinson, A. S., & Gadéa, F. X. 2010, Phys. Rev. A, 81, 032706
Belyaev, A. K., Voronov, Y. V., & Gadéa, F. X. 2018, ApJ, 867, 87
Bergemann, M., Lind, K., Collet, R., Magic, Z., & Asplund, M. 2012, MNRAS, 427, 27
Bergemann, M., Collet, R., Amarsi, A. M., et al. 2017, ApJ, 847, 15
Bergemann, M., Gallagher, A. J., Eitner, P., et al. 2019, A&A, 631, A80
Bergemann, M., Hoppe, R., Semenova, E., et al. 2021, MNRAS, in press, https://doi.org/10.1093/mnras/stab2160
Biemont, E., Grevesse, N., Hannaford, P., & Lowe, R. M. 1981, ApJ, 248, 867
Biemont, E., Baudoux, M., Kurucz, R. L., Ansbacher, W., & Pinnington, E. H. 1991, A&A, 249, 539
Blackwell, D. E., Lynas-Gray, A. E., & Smith, G. 1995, A&A, 296, 217
Blackwell-Whitehead, R., & Bergemann, M. 2007, A&A, 472, L43
Bland, P. A., Alard, O., Benedix, G. K., et al. 2005, Proc. Natl. Acad. Sci., 102, 13755
Bochsler, P. 2007, A&A, 471, 315
Bodmer, R., & Bochsler, P. 2000, J. Geophys. Res., 105, 47
Böhm-Vitense, E. 1958, Z. Astrophys., 46, 108
Booth, R. A., & Owen, J. E. 2020, MNRAS, 493, 5079
Bord, D. J., & Cowley, C. R. 2002, Sol. Phys., 211, 3
Borexino Collaboration (Agostini, M., et al.) 2020, Nature, 587, 577

Bouvier, J. 2008, A&A, 489, L53
Bouvier, A., & Wadhwa, M. 2010, Nat. Geosci., 3, 637
Braukmüller, N., Wombacher, F., Hezel, D. C., Escoube, R., & Münker, C. 2018, Geochim. Cosmochim. Acta, 239, 17
Bray, I., & Stelbovics, A. T. 1992, Phys. Rev. A., 46, 6995
Bray, I., & Stelbovics, A. T. 1995, Comput. Phys. Commun., 85, 1
Brooke, J. S. A., Bernath, P. F., Schmidt, T. W., & Bacskay, G. B. 2013, J. Quant. Spectr. Rad. Transf., 124, 11
Brooke, J. S. A., Bernath, P. F., Western, C. M., van Hemert, M. C., & Groenenboom, G. C. 2014a, J. Chem. Phys., 141, 054310a
Brooke, J. S. A., Ram, R. S., Western, C. M., et al. 2014b, ApJS, 210, 23
Brooke, J. S. A., Bernath, P. F., & Western, C. M. 2015, J. Chem. Phys., 143, 026101a
Buldgen, G., Salmon, S. J. A. J., Noels, A., et al. 2017, MNRAS, 472, 751
Buldgen, G., Salmon, S. J. A. J., Noels, A., et al. 2019a, A&A, 621, A33
Buldgen, G., Salmon, S., & Noels, A. 2019b, Front. Astron. Space Sci., 6, 42
Burbidge, E. M., Burbidge, G. R., Fowler, W. A., & Hoyle, F. 1957, Rev. Mod. Phys., 29, 547
Burnett, D. S., Barraclough, B. L., Bennett, R., et al. 2003, Space Sci. Rev., 105, 509
Burnett, D. S., Jurewicz, A. J. G., & Woolum, D. S. 2019, Meteorit. Planet. Sci., 54, 1092
Busemann, H., Bühler, F., Grimberg, A., et al. 2006, ApJ, 639, 246
Caffau, E., Ludwig, H.-G., Steffen, M., et al. 2008, A&A, 488, 1031
Caffau, E., Maiorca, E., Bonifacio, P., et al. 2009, A&A, 498, 877
Caffau, E., Ludwig, H.-G., Bonifacio, P., et al. 2010, A&A, 514, A92
Caffau, E., Ludwig, H.-G., Steffen, M., Freytag, B., & Bonifacio, P. 2011, Sol. Phys., 268, 255
Caffau, E., Ludwig, H.-G., Malherbe, J.-M., et al. 2013, A&A, 554, A126
Caffau, E., Ludwig, H.-G., Steffen, M., et al. 2015, A&A, 579, A88
Cameron, A. G. W. 1957, Atomic Energy of Canada Ltd., Pub.
Cameron, A. G. W. 1968, in Origin and Distribution of the Elements, 125
Carlos, M., Meléndez, J., Spina, L., et al. 2019, MNRAS, 485, 4052
Carlsson, M., Rutten, R. J., Bruls, J. H. M. J., & Shchukina, N. G. 1994, A&A, 288, 860
Cayrel, R., Steffen, M., Chand, H., et al. 2007, A&A, 473, L37
Chaboyer, B., Demarque, P., & Pinsonneault, M. H. 1995, ApJ, 441, 865
Chambers, J. E. 2010, ApJ, 724, 92
Charbonnel, C., & Talon, S. 2005, Science, 309, 2189
Chmielewski, Y., Brault, J. W., & Mueller, E. A. 1975, A&A, 42, 37
Christensen-Dalsgaard, J. 2021, Liv. Rev. Sol. Phys., 18, 2
Christensen-Dalsgaard, J., di Mauro, M. P., Houdek, G., & Pijpers, F. 2009, A&A, 494, 205
Claas, W. J. 1951, The Composition of the Solar Atmosphere
Clayton, R. N. 2002, Nature, 415, 860
Colgan, J., Kilcrease, D. P., Magee, N. H., et al. 2016, ApJ, 817, 116
Collet, R., Asplund, M., & Trampedach, R. 2007, A&A, 469, 687
Collet, R., Nordlund, Å., Asplund, M., Hayek, W., & Trampedach, R. 2018, MNRAS, 475, 3369
Connelly, J. N., Bizzarro, M., Krot, A. N., et al. 2012, Science, 338, 651
Cooke, R. J., Pettini, M., & Steidel, C. C. 2018, ApJ, 855, 102
Cubas Armas, M., Asensio Ramos, A., & Socas-Navarro, H. 2017, A&A, 600, A45
Cubas Armas, M., Asensio Ramos, A., & Socas-Navarro, H. 2020, A&A, 643, A142
Cunha, K., & Smith, V. V. 1999, ApJ, 512, 1006
Delbouille, L., Roland, G., & Neven, L. 1973, Atlas photometrique du spectre solaire de [lambda] 3000 a [lambda] 10000 (Liege: Universite de Liege, Institut d'Astrophysique)
Delbouille, L., Roland, G., Brault, J., & Testerman, L. 1981, Photometric Atlas of the Solar Spectrum from 1850 to 10 000 cm-1 (Kitt Peak National Observatory)
Den Hartog, E. A., Lawler, J. E., Sobeck, J. S., Sneden, C., & Cowan, J. J. 2011, ApJS, 194, 35
Den Hartog, E. A., Ruffoni, M. P., Lawler, J. E., et al. 2014, ApJS, 215, 23
Den Hartog, E. A., Lawler, J. E., Sneden, C., Cowan, J. J., & Brukhovesky, A. 2019, ApJS, 243, 33
Doerr, H.-P., Vitas, N., & Fabbian, D. 2016, A&A, 590, A118
Drawin, H.-W. 1968, Z. Phys., 211, 404
Dumont, T., Palacios, A., Charbonnel, C., et al. 2021, A&A, 646, A48
Eggenberger, P., Buldgen, G., Salmon, S., et al. 2021, Nat. Astron., submitted
Fabbian, D., Khomenko, E., Moreno-Insertis, F., & Nordlund, Å. 2010, ApJ, 724, 1536
Farmer, C. B., & Norton, R. H. 1989, A high-resolution atlas of the infrared spectrum of the sun and the earth atmosphere from space. A compilation of ATMOS spectra of the region from 650 to 4800 cm^{-1} (2.3 to 16 μm). Vol. I. The sun
Fontenla, J. M., Avrett, E., Thuillier, G., & Harder, J. 2006, ApJ, 639, 441

Freytag, B., Ludwig, H. G., & Steffen, M. 1996, A&A, 313, 497
Froese Fischer, C. 2006, J. Phys. B, 39, 2159
Gallagher, A. J., Bergemann, M., Collet, R., et al. 2020, A&A, 634, A55
Garz, T. 1973, A&A, 26, 471
Garz, T., Holweger, H., Kock, M., & Richter, J. 1969, A&A, 2, 446
Goldberg, L., Muller, E. A., & Aller, L. H. 1960, ApJS, 5, 1
Goldreich, P., & Schubert, G. 1967, ApJ, 150, 571
Goldschmidt, V. M. 1938, Skrifter Norske Videnskaps - Akademi Oslo. I. Mat. - Naturv. Klasse, 4, 1
Goldschmidt, V. M. 1922, Naturwissenschaften, 10, 918
Gonzalez, G. 1997, MNRAS, 285, 403
Gonzalez, G. 2014, MNRAS, 443, L99
Grevesse, N., & Noels, A. 1993, eds. N. Prantzos, E. Vangioni-Flam, & M. Casse Origin and Evolution of the Elements, 15–25
Grevesse, N., & Sauval, A. J. 1973, A&A, 27, 29
Grevesse, N., & Sauval, A. J. 1998, Space Sci. Rev., 85, 161
Grevesse, N., & Sauval, A. J. 1999, A&A, 347, 348
Grevesse, N., Lambert, D. L., Sauval, A. J., et al. 1991, A&A, 242, 488
Grevesse, N., Scott, P., Asplund, M., & Sauval, A. J. 2015, A&A, 573, A27
Grumer, J., & Barklem, P. S. 2020, A&A, 637, A28
Gustafsson, B., Bell, R. A., Eriksson, K., & Nordlund, A. 1975, A&A, 42, 407
Gustafsson, B., Edvardsson, B., Eriksson, K., et al. 2008, A&A, 486, 951
Hall, D. N. B., & Noyes, R. W. 1969, Astrophys. Lett., 4, 143
Hall, D. N. B., & Noyes, R. W. 1972, ApJ, 175, L95
Hannaford, P., Lowe, R. M., Grevesse, N., & Noels, A. 1992, A&A, 259, 301
Harutyunyan, G., Steffen, M., Mott, A., et al. 2018, A&A, 618, A16
Hase, F., Wallace, L., McLeod, S. D., Harrison, J. J., & Bernath, P. F. 2010, J. Quant. Spectr. Rad. Transf., 111, 521
Hayek, W., Asplund, M., Carlsson, M., et al. 2010, A&A, 517, A49
Heber, V. S., Wieler, R., Baur, H., et al. 2009, Geochim. Cosmochim. Acta, 73, 7414
Heber, V. S., Baur, H., Bochsler, P., et al. 2012, ApJ, 759, 121
Heiter, U., Lind, K., Bergemann, M., et al. 2021, A&A, 645, A106
Holmes, C. E., Pickering, J. C., Ruffoni, M. P., et al. 2016, ApJS, 224, 35
Holweger, H. 2001, in Joint SOHO/ACE workshop "Solar and Galactic Composition", ed. R. F. Wimmer-Schweingruber, AIP Conf. Ser., 598, 23
Holweger, H., & Müller, E. A. 1974, Sol. Phys., 39, 19
Holweger, H., Gehlsen, M., & Ruland, F. 1978, A&A, 70, 537
Holweger, H., Bard, A., Kock, M., & Kock, A. 1991, A&A, 249, 545
Hubeny, I., Hummer, D. G., & Lanz, T. 1994, A&A, 282, 151
Hummer, D. G., Berrington, K. A., Eissner, W., et al. 1993, A&A, 279, 298
Huss, G. R., Koeman-Shields, E., Jurewicz, A. J. G., et al. 2020, Meteorit. Planet. Sci., 55, 326
Ibgui, L., Hubeny, I., Lanz, T., & Stehlé, C. 2013, A&A, 549, A126
Israelian, G., Delgado Mena, E., Santos, N. C., et al. 2009, Nature, 462, 189
Johansson, S., Litzén, U., Lundberg, H., & Zhang, Z. 2003, ApJ, 584, L107
Jurewicz, A. J. G., Burnett, D. S., Wiens, R. C., et al. 2003, Space Sci. Rev., 105, 535
Jurewicz, A. J. G., Rieck, K. D., Hervig, R., et al. 2020, Meteorit. Planet. Sci., 55, 352
King, A. J., Phillips, K. J. H., Strekopytov, S., Vita-Finzi, C., & Russell, S. S. 2020, Geochim. Cosmochim. Acta, 268, 73
Kiselman, D. 1991, A&A, 245, L9
Kiselman, D. 1994, A&A, 286, 169
Kiselman, D., & Nordlund, A. 1995, A&A, 302, 578
Kobayashi, C., Karakas, A. I., & Lugaro, M. 2020, ApJ, 900, 179
Kock, M., & Richter, J. 1968, ZAp, 69, 180
Korn, A. J., Shi, J., & Gehren, T. 2003, A&A, 407, 691
Korotin, S. A. 2020, Astron. Lett., 46, 541
Kramida, A. 2019, in APS Meeting Abstracts, 2019, N09.004
Krief, M., Kurzweil, Y., Feigel, A., & Gazit, D. 2018, ApJ, 856, 135
Krot, A. N., Keil, K., Scott, E. R. D., Goodrich, C. A., & Weisberg, M. K. 2014, in Classification of Meteorites and Their Genetic Relationships, ed. A. M. Davis, 1, 1
Kurucz, R. 1993, ATLAS9 Stellar Atmosphere Programs and 2 km/s grid. Kurucz CD-ROM No. 13. Cambridge, Mass.: Smithsonian Astrophysical Observatory, 1993, 13
Kurucz, R. L. 2005, Mem. Soc. Astron. It. Suppl., 8, 189
Kurucz, R. L. 2006, ArXiv e-prints [arXiv:astro-ph/0605029]
Kurucz, R. L., Furenlid, I., Brault, J., & Testerman, L. 1984, Solar flux atlas from 296 to 1300 nm
Lambert, D. L. 1968, MNRAS, 138, 143
Lambert, D. L. 1978, MNRAS, 182, 249
Lambert, D. L. 1993, Phys. Scr. Vol. T, 47, 186
Lambert, D. L., Mallia, E. A., & Smith, G. 1972, Sol. Phys., 26, 250
Laming, J. M. 2015, Liv. Rev. Sol. Phys., 12, 2
Laming, J. M., Heber, V. S., Burnett, D. S., et al. 2017, ApJ, 851, L12
Landi, E., & Testa, P. 2015, ApJ, 800, 110

Landi, E., Feldman, U., & Doschek, G. A. 2007, ApJ, 659, 743
Lawler, J. E., Wickliffe, M. E., den Hartog, E. A., & Sneden, C. 2001, ApJ, 563, 1075
Lawler, J. E., Guzman, A., Wood, M. P., Sneden, C., & Cowan, J. J. 2013, ApJS, 205, 11
Lawler, J. E., Wood, M. P., Den Hartog, E. A., et al. 2014, ApJS, 215, 20
Lawler, J. E., Sneden, C., & Cowan, J. J. 2015, ApJS, 220, 13
Lawler, J. E., Sneden, C., Nave, G., et al. 2017, ApJS, 228, 10
Lawler, J. E., Hala, C., Sneden, G., et al. 2019, ApJS, 241, 21
Leenaarts, J., & Carlsson, M. 2009, in The Second Hinode Science Meeting, eds. B. Lites, M. Cheung, T. Magara, J. Mariska, & K. Reeves, ASP Conf. Ser., 415, 87
Lellouch, E., Bézard, B., Fouchet, T., et al. 2001, A&A, 370, 610
Li, G., Gordon, I. E., Rothman, L. S., et al. 2015, ApJS, 216, 15
Li, W., Hartman, H., Wang, K., & Jönsson, P. 2020, A&A, 643, A156
Li, W., Amarsi, A. M., Papoulia, A., Ekman, J., & Jönsson, P. 2021, MNRAS, 502, 3780
Liang, G. Y., Whiteford, A. D., & Badnell, N. R. 2009, J. Phys. B At. Mol. Phys., 42, 225002
Lind, K., Asplund, M., & Barklem, P. S. 2009, A&A, 503, 541
Lind, K., Asplund, M., Barklem, P. S., & Belyaev, A. K. 2011, A&A, 528, A103
Lind, K., Melendez, J., Asplund, M., Collet, R., & Magic, Z. 2013, A&A, 554, A96
Lind, K., Amarsi, A. M., Asplund, M., et al. 2017, MNRAS, 468, 4311
Linsky, J. L., Draine, B. T., Moos, H. W., et al. 2006, ApJ, 647, 1106
Liu, Y. P., Gao, C., Zeng, J. L., Yuan, J. M., & Shi, J. R. 2014, ApJS, 211, 30
Ljung, G., Nilsson, H., Asplund, M., & Johansson, S. 2006, A&A, 456, 1181
Lodders, K. 2003, ApJ, 591, 1220
Lodders, K. 2008, ApJ, 674, 607
Lodders, K. 2019, ArXiv e-prints [arXiv:1912.00844]
Lodders, K., Palme, H., & Gail, H. P. 2009, Landolt Börnstein, 44
Ludwig, H.-G., Freytag, B., & Steffen, M. 1999, A&A, 346, 111
Lyons, J. R., Gharib-Nezhad, E., & Ayres, T. R. 2018, Nat. Commun., 9, 908
Maas, Z. G., Pilachowski, C. A., & Hinkle, K. 2016, AJ, 152, 196
Magic, Z., Collet, R., Asplund, M., et al. 2013, A&A, 557, A26
Mahaffy, P. R., Donahue, T. M., Atreya, S. K., Owen, T. C., & Niemann, H. B. 1998, Space Sci. Rev., 84, 251
Maiorca, E., Uitenbroek, H., Uttenthaler, S., et al. 2014, ApJ, 788, 149
Malcheva, G., Engström, L., Lundberg, H., et al. 2015, MNRAS, 450, 223
Marty, B., Zimmermann, L., Burnard, P. G., et al. 2010, Geochim. Cosmochim. Acta, 74, 340
Mashonkina, L., Ryabchikova, T., Ryabtsev, A., & Kildiyarova, R. 2009, A&A, 495, 297
Mashonkina, L., Gehren, T., Shi, J.-R., Korn, A. J., & Grupp, F. 2011, A&A, 528, A87
Mashonkina, L., Sitnova, T., & Belyaev, A. K. 2017, A&A, 605, A53
Masseron, T., Plez, B., Van Eck, S., et al. 2014, A&A, 571, A47
McKeegan, K. D., Kallio, A. P. A., Heber, V. S., et al. 2011, Science, 332, 1528
Meija, J., Coplen, T. B., Berglund, M., et al. 2016a, Pure Appl. Chem., 88, 265
Meija, J., Coplen, T. B., Berglund, M., et al. 2016b, Pure Appl. Chem., 88, 293
Meléndez, M., Bautista, M. A., & Badnell, N. R. 2007, A&A, 469, 1203
Meléndez, J., Asplund, M., Gustafsson, B., & Yong, D. 2009, ApJ, 704, L66
Meshik, A., Hohenberg, C., Pravdivtseva, O., & Burnett, D. 2014, Geochim. Cosmochim. Acta, 127, 326
Meshik, A., Pravdivtseva, O., & Burnett, D. 2020, Geochim. Cosmochim. Acta, 276, 289
Mihalas, D., Dappen, W., & Hummer, D. G. 1988, ApJ, 331, 815
Mondet, G., Blancard, C., Cossé, P., & Faussurier, G. 2015, ApJS, 220, 2
Mott, A., Steffen, M., Caffau, E., Spada, F., & Strassmeier, K. G. 2017, A&A, 604, A44
Mott, A., Steffen, M., Caffau, E., & Strassmeier, K. G. 2020, A&A, 638, A58
Muthsam, H. J., Kupka, F., Löw-Baselli, B., et al. 2010, New Astron., 15, 460
Nagayama, T., Bailey, J. E., Loisel, G. P., et al. 2019, Phys. Rev. Lett., 122, 235001
Nahar, S. N., & Pradhan, A. K. 2016, Phys. Rev. Lett., 116, 235003
Neckel, H. 1999, Sol. Phys., 184, 421
Nieva, M.-F., & Przybilla, N. 2012, A&A, 539, A143
Nissen, P. E., & Gustafsson, B. 2018, A&ARv, 26, 6
Nordlander, T., & Lind, K. 2017, A&A, 607, A75
Nordlund, Å. 1982, A&A, 107, 1
Nordlund, Å., & Dravins, D. 1990, A&A, 228, 155
Nordlund, Å., & Galsgaard, K. 1995, A 3D MHD code for Parallel Computers, Tech. rep. (Niels Bohr Institute, University of Copenhagen)
Nordlund, Å., Stein, R. F., & Asplund, M. 2009, Liv. Rev. Sol. Phys., 6, 2
O'Brian, T. R., & Lawler, J. E. 1991, Phys. Lett. A, 152, 407
O'Brian, T. R., Wickliffe, M. E., Lawler, J. E., Whaling, W., & Brault, J. W. 1991, J. Opt. Soc. Am. B Opt. Phys., 8, 1185
Osorio, Y., Barklem, P. S., Lind, K., et al. 2015, A&A, 579, A53

Osorio, Y., Lind, K., Barklem, P. S., Allende Prieto, C., & Zatsarinny, O. 2019, A&A, 623, A103
Osorio, Y., Allende Prieto, C., Hubeny, I., Mészáros, S., & Shetrone, M. 2020, A&A, 637, A80
Owen, T., Mahaffy, P. R., Niemann, H. B., Atreya, S., & Wong, M. 2001, ApJ, 553, L77
Palme, H., & Hezel, D. C. 2011, Meteorit. Planet. Sci. Suppl., 74, 5302
Palme, H., Lodders, K., & Jones, A. 2014, in Solar System Abundances of the Elements, ed. A. M. Davis, 2, 15
Payne, C. H. 1925, PhD Thesis, Radcliffe College, USA
Pehlivan Rhodin, A., Hartman, H., Nilsson, H., & Jönsson, P. 2017a, A&A, 598, A102
Pehlivan Rhodin, A., Belmonte, M. T., Engström, L., et al. 2017b, MNRAS, 472, 3337
Pehlivan Rhodin, A., Hartmann, H., Nilsson, H., & Jönsson, P. 2021, A&A, submitted
Pereira, T. M. D., Asplund, M., & Kiselman, D. 2009, A&A, 508, 1403
Pereira, T. M. D., Asplund, M., Collet, R., et al. 2013, A&A, 554, A118
Pinsonneault, M. H., & Delahaye, F. 2009, ApJ, 704, 1174
Piskunov, N. E., Kupka, F., Ryabchikova, T. A., Weiss, W. W., & Jeffery, C. S. 1995, A&AS, 112, 525
Prodanović, T., Steigman, G., & Fields, B. D. 2010, MNRAS, 406, 1108
Prša, A., Harmanec, P., Torres, G., et al. 2016, AJ, 152, 41
Ramírez, I., Asplund, M., Baumann, P., Meléndez, J., & Bensby, T. 2010, A&A, 521, A33
Reames, D. V. 2014, Sol. Phys., 289, 977
Reames, D. V. 2020, Space Sci. Rev., 216, 20
Reggiani, H., Amarsi, A. M., Lind, K., et al. 2019, A&A, 627, A177
Reifarth, R., Heil, M., Käppeler, F., et al. 2002, Phys. Rev. C, 66, 064603
Reiners, A., Mrotzek, N., Lemke, U., Hinrichs, J., & Reinsch, K. 2016, A&A, 587, A65
Reisenfeld, D. B., Wiens, R. C., Barraclough, B. L., et al. 2013, Space Sci. Rev., 175, 125
Rempel, M. 2014, ApJ, 789, 132
Rogers, F. J., & Nayfonov, A. 2002, ApJ, 576, 1064
Ross, J. E., & Aller, L. H. 1976, Science, 191, 1223
Ruffoni, M. P., Allende Prieto, C., Nave, G., & Pickering, J. C. 2013, ApJ, 779, 17
Russell, H. N. 1929, ApJ, 70, 11
Rutten, R. J. 2003, Radiative Transfer in Stellar Atmospheres, 8th edn. (Utrecht University)
Rutten, R. J., & Kostik, R. I. 1982, A&A, 115, 104
Saloman, E. B., & Kramida, A. 2017, ApJS, 231, 18
Scott, E. R. D. 2007, Ann. Rev. Earth Planet. Sci., 35, 577
Scott, P. C., Asplund, M., Grevesse, N., & Sauval, A. J. 2006, A&A, 456, 675
Scott, P., Asplund, M., Grevesse, N., Bergemann, M., & Sauval, A. J. 2015a, A&A, 573, A26
Scott, P., Grevesse, N., Asplund, M., et al. 2015b, A&A, 573, A25
Seaton, M. J. 1987, J. Phys. B, 20, 6363
Serenelli, A. M., Basu, S., Ferguson, J. W., & Asplund, M. 2009, ApJ, 705, L123
Serenelli, A., Scott, P., Villante, F. L., et al. 2016, MNRAS, 463, 2
Shchukina, N., & Trujillo Bueno, J. 2015, A&A, 579, A112
Shchukina, N., Sukhorukov, A., & Trujillo Bueno, J. 2016, A&A, 586, A145
Shi, J. R., Gehren, T., Zeng, J. L., Mashonkina, L., & Zhao, G. 2014, ApJ, 782, 80
Short, C. I., & Hauschildt, P. H. 2009, ApJ, 691, 1634
Sneden, C., Lawler, J. E., Cowan, J. J., Ivans, I. I., & Den Hartog, E. A. 2009, ApJS, 182, 80
Sonoi, T., Samadi, R., Belkacem, K., et al. 2015, A&A, 583, A112
Steenbock, W., & Holweger, H. 1984, A&A, 130, 319
Steffen, M., Caffau, E., & Ludwig, H.-G. 2013, Mem. Soc. Astron. It. Suppl., 24, 37
Steffen, M., Prakapavičius, D., Caffau, E., et al. 2015, A&A, 583, A57
Stein, R. F., & Nordlund, Å. 1998, ApJ, 499, 914
Stenflo, J. O. 2015, A&A, 573, A74
Suess, H. E. 1947a, Zeitschrift Naturforschung Teil A, 2, 311
Suess, H. E. 1947b, Zeitschrift Naturforschung Teil A, 2, 604
Suess, H. E., & Urey, H. C. 1956, Rev. Mod. Phys., 28, 53
Tachiev, G. I., & Froese Fischer, C. 2002, A&A, 385, 716
Takeda, Y. 1994, PASJ, 46, 53
Takeda, Y. 2021, Astron. Nachr., 342, 515
Takeda, Y., Kato, K.-I., Watanabe, Y., & Sadakane, K. 1996, PASJ, 48, 511
Takeda, Y., Hashimoto, O., Taguchi, H., et al. 2005, PASJ, 57, 751
Tan, K., Shi, J., & Zhao, G. 2010, ApJ, 713, 458
Théado, S., & Vauclair, S. 2012, ApJ, 744, 123
Thoul, A. A., Bahcall, J. N., & Loeb, A. 1994, ApJ, 421, 828
Trampedach, R., Däppen, W., & Baturin, V. A. 2006, ApJ, 646, 560
Trampedach, R., Asplund, M., Collet, R., Nordlund, Å., & Stein, R. F. 2013, ApJ, 769, 18
Tucci Maia, M., Meléndez, J., Castro, M., et al. 2015, A&A, 576, L10
Unsöld, A. 1948, ZAp, 24, 306
Urey, H. C. 1952, Phys. Rev., 88, 248
van Kooten, E. M. M. E., Moynier, F., & Agranier, A. 2019, Proc. Natl. Acad. Sci., 116, 18860
Vinyoles, N., Serenelli, A. M., Villante, F. L., et al. 2017, ApJ, 835, 202
Vitas, N., Vince, I., Lugaro, M., et al. 2008, MNRAS, 384, 370
Vögler, A., & Schüssler, M. 2007, A&A, 465, L43
Vögler, A., Shelyag, S., Schüssler, M., et al. 2005, A&A, 429, 335
von Steiger, R., & Zurbuchen, T. H. 2016, ApJ, 816, 13
Vorontsov, S. V., Baturin, V. A., Ayukov, S. V., & Gryaznov, V. K. 2013, MNRAS, 430, 1636
Wallace, L., Hinkle, K., & Livingston, W. C. 2001, Sunspot umbral spectra in the region 4000 to 8640 cm(-1) (1.16 to 2.50 [microns])
Wang, K., Bartschat, K., & Zatsarinny, O. 2018, ApJ, 867, 63
Wang, H. S., Lineweaver, C. H., & Ireland, T. R. 2019, Icarus, 328, 287
Wang, E. X., Nordlander, T., Asplund, M., et al. 2021, MNRAS, 500, 2159
Wasson, J. T., & Kallemeyn, G. W. 1988, Phil. Trans. R. Soc. London, Ser. A, 325, 535
Weinberg, D. H. 2017, ApJ, 851, 25
Wiens, R. C., Reisenfeld, D. B., Olinger, C., et al. 2013, Space Sci. Rev., 175, 93
Wisshak, K., Voss, F., Käppeler, F., Kazakov, L., & Reffo, G. 1998, Phys. Rev. C, 57, 391
Wittenmyer, R. A., Wang, S., Horner, J., et al. 2020, MNRAS, 492, 377
Wood, M. P., Lawler, J. E., Sneden, C., & Cowan, J. J. 2013, ApJS, 208, 27
Wood, M. P., Lawler, J. E., Den Hartog, E. A., Sneden, C., & Cowan, J. J. 2014a, ApJS, 214, 18
Wood, M. P., Lawler, J. E., Sneden, C., & Cowan, J. J. 2014b, ApJS, 211, 20
Wood, B. E., Müller, H.-R., & Möbius, E. 2019, ApJ, 881, 55
Yakovleva, S. A., Barklem, P. S., & Belyaev, A. K. 2018, MNRAS, 473, 3810
Yakovleva, S. A., Belyaev, A. K., & Kraemer, W. P. 2019, MNRAS, 483, 5105
Yana Galarza, J., Meléndez, J., Karakas, A. I., Asplund, M., & Lorenzo-Oliveira, D. 2021, MNRAS, 502, L104
Yang, W. 2019, ApJ, 873, 18
Young, P. R. 2005, A&A, 439, 361
Young, P. R. 2018, ApJ, 855, 15
Zatsarinny, O. 2006, Comput. Phys. Commun., 174, 273
Zatsarinny, O., & Bartschat, K. 2013, J. Phys. B, 46, 112001
Zatsarinny, O., Parker, H., & Bartschat, K. 2019a, Phys. Rev. A, 99, 012706
Zatsarinny, O., Bartschat, K., Fernandez-Menchero, L., & Tayal, S. S. 2019b, Phys. Rev. A, 99, 023430
Zhang, H. L., & Pradhan, A. K. 1995, A&A, 293
Zhang, Q.-S., Li, Y., & Christensen-Dalsgaard, J. 2019, ApJ, 881, 103
Zhou, Y., Asplund, M., & Collet, R. 2019, ApJ, 880, 13
Zink, J. K., Christiansen, J. L., & Hansen, B. M. S. 2019, MNRAS, 483, 4479

Appendix A: Line lists for Na, Mg, K, Ca, and Fe

Table A.1. Line list for the Na, Mg, K, and Ca lines used for 3D non-LTE spectral line formation calculations to derive the solar photospheric abundances.

λ_{air}/nm	E_{lower}/eV	E_{upper}/eV	$\log gf$	W/pm	Non-LTE				LTE			
					3D	$\langle 3D\rangle$	MARCS	HM	3D	$\langle 3D\rangle$	MARCS	HM
					Na I							
475.18	2.10443	4.71289	−2.077	1.14	6.223	6.225	6.199	6.243	6.250	6.259	6.231	6.280
514.88	2.10230	4.50963	−2.044	1.32	6.231	6.235	6.206	6.251	6.259	6.271	6.239	6.288
615.42	2.10230	4.11636	−1.547	3.98	6.250	6.255	6.215	6.266	6.294	6.307	6.262	6.320
616.07	2.10443	4.11636	−1.246	5.83	6.178	6.179	6.135	6.190	6.229	6.240	6.193	6.256
1074.64	3.19135	4.34476	−1.294	1.33	6.221	6.221	6.188	6.223	6.226	6.227	6.194	6.231
					Mg I							
631.87	5.10783	7.06946	−2.020	4.13	7.546	7.546	7.509	7.559	7.545	7.547	7.509	7.559
631.92	5.10783	7.06930	−2.242	2.60	7.549	7.547	7.516	7.558	7.548	7.547	7.516	7.558
871.27	5.93195	7.35459	−1.152	6.80	7.565	7.560	7.517	7.566	7.566	7.561	7.518	7.568
871.78	5.93279	7.35459	−0.930	10.00	7.581	7.575	7.524	7.584	7.583	7.577	7.526	7.587
892.36	5.39373	6.78275	−1.679	6.33	7.608	7.605	7.562	7.614	7.607	7.605	7.562	7.614
998.32	5.93154	7.17313	−2.177	1.00	7.558	7.553	7.525	7.556	7.559	7.554	7.526	7.558
1031.25	6.11821	7.32015	−1.718	1.83	7.515	7.508	7.479	7.513	7.515	7.509	7.479	7.513
1587.95	5.94592	6.72648	−1.226	16.80	7.570	7.565	7.517	7.594	7.571	7.566	7.518	7.595
					Mg II							
787.70	9.99554	11.56910	0.389	1.90	7.540	7.542	7.526	7.572	7.568	7.570	7.542	7.606
789.64	9.99933	11.56904	0.645	3.00	7.635	7.655	7.640	7.681	7.682	7.702	7.669	7.731
921.82	8.65471	9.99933	0.269	7.40	7.531	7.501	7.481	7.504	7.642	7.592	7.559	7.607
924.43	8.65471	9.99554	−0.034	5.15	7.489	7.465	7.447	7.478	7.567	7.535	7.505	7.554
1009.22	11.62968	12.85786	1.283	1.33	7.495	7.541	7.523	7.598	7.490	7.536	7.518	7.596
1091.42	8.86365	9.99933	0.036	5.22	7.427	7.401	7.388	7.419	7.518	7.481	7.451	7.509
					K I							
693.88	1.61711	3.40345	−1.145	0.43	5.045	5.044	5.010	5.050	5.071	5.081	5.046	5.087
1176.97	1.61711	2.67025	−0.481	3.50	5.082	5.070	5.029	5.079	5.135	5.144	5.102	5.153
1252.22	1.61711	2.60696	−0.128	7.60	5.093	5.075	5.025	5.090	5.157	5.163	5.110	5.178
					Ca I							
451.23	2.52568	5.27263	−1.900	2.20	6.296	6.304	6.272	6.327	6.285	6.304	6.270	6.327
526.04	2.52126	4.87755	−1.719	3.00	6.265	6.271	6.230	6.290	6.253	6.272	6.230	6.292
586.76	2.93251	5.04497	−1.570	2.30	6.278	6.284	6.244	6.298	6.269	6.285	6.244	6.300
616.38	2.52126	4.53221	−1.286	6.20	6.295	6.331	6.282	6.350	6.286	6.339	6.290	6.362
616.64	2.52126	4.53134	−1.142	7.13	6.281	6.271	6.210	6.294	6.275	6.284	6.221	6.309
616.93 [a]	2.52433	4.53347	−0.308	21.66	6.293	6.259	6.185	6.287	6.304	6.295	6.215	6.325
645.56	2.52299	4.44302	−1.340	5.65	6.319	6.309	6.261	6.326	6.311	6.322	6.272	6.340
647.17	2.52568	4.44095	−0.686	9.30	6.297	6.241	6.177	6.263	6.317	6.294	6.224	6.320
649.96	2.52299	4.43001	−0.818	8.75	6.334	6.286	6.225	6.307	6.348	6.330	6.264	6.355
					Ca II							
500.15	7.50514	9.98340	−0.507	1.35	6.231	6.235	6.238	6.290	6.237	6.241	6.243	6.299
645.69	8.43798	10.35764	0.412	1.85	6.296	6.291	6.269	6.329	6.296	6.293	6.269	6.331
732.39	0.00000	1.69241	−7.536	1.00	6.372	6.373	6.344	6.391	6.372	6.373	6.344	6.391
824.88	7.51484	9.01749	0.556	6.70	6.302	6.261	6.228	6.267	6.364	6.324	6.279	6.339
825.47	7.51484	9.01641	−0.398	1.80	6.296	6.284	6.270	6.303	6.322	6.310	6.291	6.333

Notes. [a]Doublet consisting of the 616.9042 nm and 616.9563 nm components. The quoted gf-value and equivalent width are the combined values.

Table A.2. Line list for the Fe lines used for 3D non-LTE spectral line formation calculations to derive the solar photospheric abundances.

λ_{air}/nm	E_{lower}/eV	E_{upper}/eV	$\log gf$	W/pm	Non-LTE				LTE			
					3D	$\langle$3D$\rangle$	MARCS	HM	3D	$\langle$3D$\rangle$	MARCS	HM
					Fe I							
444.55	0.08729	2.87550	−5.412	3.80	7.455	7.496	7.453	7.542	7.424	7.511	7.462	7.558
457.42	3.21119	5.92093	−2.350	3.87	7.451	7.448	7.408	7.475	7.440	7.450	7.408	7.479
524.70	0.08729	2.44956	−4.961	6.40	7.483	7.477	7.421	7.523	7.434	7.498	7.436	7.550
537.96	3.69460	5.99868	−1.420	6.17	7.433	7.383	7.329	7.413	7.429	7.399	7.340	7.433
548.31	4.15435	6.41493	−1.390	4.37	7.417	7.399	7.353	7.421	7.407	7.401	7.352	7.426
553.85	4.21758	6.45554	−1.540	3.73	7.488	7.477	7.436	7.495	7.480	7.478	7.435	7.498
560.02	4.26045	6.47375	−1.420	3.65	7.402	7.386	7.343	7.405	7.388	7.385	7.339	7.407
561.86	4.20888	6.41493	−1.250	5.00	7.444	7.418	7.369	7.440	7.432	7.421	7.368	7.446
566.13	4.28435	6.47375	−1.756	2.22	7.437	7.429	7.393	7.444	7.424	7.427	7.389	7.445
570.55	4.30128	6.47375	−1.355	3.96	7.428	7.411	7.367	7.430	7.418	7.413	7.366	7.434
577.51	4.22036	6.36665	−1.080	6.19	7.486	7.449	7.396	7.473	7.481	7.459	7.401	7.486
577.85	2.58811	4.73314	−3.440	2.04	7.430	7.446	7.406	7.467	7.416	7.451	7.409	7.474
578.47	3.39651	5.53924	−2.532	2.58	7.443	7.444	7.405	7.462	7.429	7.445	7.403	7.465
585.51	4.60759	6.72456	−1.478	2.20	7.441	7.432	7.395	7.445	7.430	7.430	7.392	7.446
595.67	0.85900	2.93985	−4.552	5.02	7.451	7.467	7.419	7.500	7.424	7.483	7.431	7.522
615.16	2.17595	4.19086	−3.282	4.88	7.459	7.455	7.409	7.481	7.443	7.466	7.417	7.494
624.06	2.22271	4.20888	−3.287	4.76	7.478	7.477	7.432	7.503	7.465	7.488	7.441	7.519
631.15	2.83159	4.79547	−3.141	2.66	7.492	7.502	7.463	7.524	7.481	7.509	7.467	7.532
649.89	0.95816	2.86539	−4.695	4.16	7.469	7.499	7.455	7.536	7.445	7.517	7.466	7.555
651.84	2.83159	4.73314	−2.448	5.72	7.405	7.378	7.325	7.405	7.392	7.392	7.334	7.421
657.42	0.99011	2.87550	−5.010	2.54	7.465	7.517	7.472	7.549	7.442	7.532	7.482	7.565
669.91	4.59311	6.44335	−2.101	0.78	7.487	7.481	7.448	7.488	7.476	7.480	7.445	7.490
679.33	4.07581	5.90041	−2.326	1.25	7.445	7.443	7.408	7.453	7.434	7.444	7.407	7.456
683.70	4.59311	6.40604	−1.687	1.77	7.486	7.474	7.440	7.482	7.475	7.475	7.438	7.485
684.37	4.54851	6.35967	−0.730	6.50	7.409	7.362	7.304	7.380	7.401	7.373	7.309	7.396
685.48	4.59311	6.40133	−1.926	1.29	7.434	7.439	7.395	7.451	7.423	7.438	7.391	7.451
685.81	4.60759	6.41493	−0.900	5.50	7.464	7.431	7.380	7.445	7.456	7.437	7.382	7.455
699.99	4.10337	5.87412	−1.380	5.79	7.482	7.456	7.405	7.472	7.477	7.466	7.412	7.486
700.80	4.17770	5.94640	−1.770	2.95	7.435	7.426	7.386	7.438	7.425	7.429	7.386	7.443
721.97	4.07581	5.79265	−1.430	4.90	7.399	7.366	7.318	7.381	7.393	7.379	7.326	7.397
740.17	4.18636	5.86098	−1.500	4.16	7.423	7.399	7.355	7.411	7.415	7.408	7.361	7.423
744.30	4.18636	5.85168	−1.640	3.59	7.450	7.431	7.390	7.441	7.439	7.436	7.392	7.449
791.29	0.85900	2.42543	−4.848	4.57	7.480	7.517	7.470	7.552	7.452	7.540	7.484	7.575
829.35	3.30092	4.79547	−2.203	5.85	7.486	7.461	7.416	7.480	7.475	7.475	7.425	7.495
857.18	5.00952	6.45554	−1.110	3.17	7.499	7.489	7.452	7.495	7.501	7.496	7.457	7.505
859.88	4.38646	5.82794	−1.200	5.67	7.419	7.394	7.343	7.407	7.413	7.404	7.350	7.421
887.60	5.02028	6.41674	−1.050	3.55	7.502	7.489	7.451	7.495	7.504	7.497	7.457	7.506
890.60	5.06378	6.45554	−1.220	2.47	7.492	7.484	7.448	7.488	7.492	7.490	7.453	7.496
910.36	4.17770	5.53924	−2.190	1.92	7.481	7.479	7.444	7.487	7.468	7.479	7.441	7.489
978.66	4.60759	5.87412	−1.840	1.82	7.466	7.460	7.425	7.466	7.456	7.461	7.424	7.469
					Fe II							
441.68	2.77846	5.58477	−2.570	8.07	7.419	7.316	7.283	7.370	7.427	7.319	7.286	7.374
450.83	2.85552	5.60489	−2.420	8.85	7.488	7.382	7.346	7.434	7.498	7.386	7.350	7.440
462.05	2.82812	5.51071	−3.210	5.40	7.429	7.362	7.335	7.406	7.433	7.363	7.336	7.407
465.70	2.89102	5.55261	−3.600	3.60	7.435	7.395	7.381	7.434	7.437	7.396	7.381	7.434
523.46	3.22131	5.58920	−2.180	8.80	7.484	7.361	7.318	7.403	7.498	7.368	7.323	7.410
526.48	3.23046	5.58477	−3.130	4.62	7.496	7.438	7.413	7.469	7.499	7.439	7.414	7.470
541.41	3.22131	5.51071	−3.580	2.73	7.471	7.436	7.421	7.464	7.473	7.436	7.421	7.464
643.27	2.89102	4.81790	−3.570	4.30	7.492	7.434	7.409	7.454	7.494	7.434	7.408	7.453
651.61	2.89102	4.79324	−3.310	5.69	7.545	7.454	7.422	7.474	7.548	7.453	7.422	7.473
722.24	3.88870	5.60489	−3.260	1.87	7.455	7.419	7.406	7.436	7.457	7.420	7.407	7.436
722.45	3.88919	5.60489	−3.200	2.10	7.469	7.431	7.417	7.447	7.470	7.431	7.417	7.447
751.58	3.90342	5.55261	−3.390	1.47	7.447	7.414	7.403	7.429	7.448	7.414	7.403	7.430
771.17	3.90342	5.51071	−2.500	5.04	7.457	7.376	7.345	7.388	7.462	7.378	7.347	7.391

Appendix B: Isotopic abundances

Table B.1. Representative isotopic abundance fractions and logarithmic abundances by number ($\log \epsilon_{\mathrm{H}} \equiv 12.00$) at the time of birth of the Sun.

Z	Elem.	A	fraction %	log ϵ	Z	Elem.	A	fraction %	log ϵ	Z	Elem.	A	fraction %	log ϵ
1	H	1	99.998	12.00	24	Cr	50	4.345	4.32	41	Nb	93	100.000	1.53
1	H	2	0.002	7.22	24	Cr	52	83.789	5.61	42	Mo	92	14.649	1.11
2	He	3	0.017	7.20	24	Cr	53	9.501	4.66	42	Mo	94	9.187	0.91
2	He	4	99.983	10.98	24	Cr	54	2.365	4.06	42	Mo	95	15.873	1.14
3	Li	6	4.850	1.98	25	Mn	55	100.000	5.48	42	Mo	96	16.673	1.17
3	Li	7	95.150	3.28	26	Fe	54	5.845	6.29	42	Mo	97	9.582	0.93
4	Be	9	100.000	1.44	26	Fe	56	91.754	7.49	42	Mo	98	24.292	1.33
5	B	10	19.650	2.06	26	Fe	57	2.119	5.85	42	Mo	100	9.744	0.93
5	B	11	80.350	2.67	26	Fe	58	0.282	4.97	44	Ru	96	5.540	0.56
6	C	12	98.893	8.52	27	Co	59	100.000	5.00	44	Ru	98	1.870	0.09
6	C	13	1.107	6.57	28	Ni	58	68.077	6.10	44	Ru	99	12.760	0.92
7	N	14	99.775	7.89	28	Ni	60	26.223	5.68	44	Ru	100	12.600	0.91
7	N	15	0.225	5.25	28	Ni	61	1.140	4.32	44	Ru	101	17.060	1.05
8	O	16	99.776	8.75	28	Ni	62	3.635	4.82	44	Ru	102	31.550	1.31
8	O	17	0.036	5.31	28	Ni	64	0.926	4.23	44	Ru	104	18.620	1.08
8	O	18	0.188	6.03	29	Cu	63	69.150	4.08	44	Rh	103	100.000	0.84
9	F	19	100.000	4.46	29	Cu	65	30.850	3.73	45	Pd	102	1.020	−0.36
10	Ne	20	92.810	8.09	30	Zn	64	49.170	4.32	46	Pd	104	11.140	0.68
10	Ne	21	0.242	5.51	30	Zn	66	27.730	4.07	46	Pd	105	22.330	0.98
10	Ne	22	6.948	6.97	30	Zn	67	4.040	3.23	46	Pd	106	27.330	1.07
11	Na	23	100.000	6.28	30	Zn	68	18.450	3.89	46	Pd	108	26.460	1.06
12	Mg	24	78.965	7.51	30	Zn	70	0.610	2.41	46	Pd	110	11.720	0.70
12	Mg	25	10.011	6.61	31	Ga	69	60.108	2.86	46	Ag	107	51.839	0.74
12	Mg	26	11.025	6.66	31	Ga	71	39.892	2.68	47	Ag	109	48.161	0.71
13	Al	27	100.000	6.49	32	Ge	70	20.520	3.00	47	Cd	106	1.245	−0.19
14	Si	28	92.254	7.54	32	Ge	72	27.450	3.12	48	Cd	108	0.888	−0.34
14	Si	29	4.672	6.24	32	Ge	73	7.760	2.57	48	Cd	110	12.470	0.81
14	Si	30	3.073	6.06	32	Ge	74	36.520	3.25	48	Cd	111	12.795	0.82
15	P	31	100.000	5.47	32	Ge	76	7.750	2.57	48	Cd	112	24.109	1.10
16	S	32	94.850	7.16	33	As	75	100.000	2.35	48	Cd	113	12.227	0.80
16	S	33	0.763	5.07	34	Se	74	0.860	1.29	48	Cd	114	28.754	1.17
16	S	34	4.365	5.82	34	Se	76	9.230	2.32	48	Cd	116	7.512	0.59
16	S	36	0.016	3.38	34	Se	77	7.600	2.24	48	In	113	4.281	−0.50
17	Cl	35	75.800	5.25	34	Se	78	23.690	2.73	49	In	115	95.719	0.84
17	Cl	37	24.200	4.76	34	Se	80	49.800	3.05	49	Sn	112	0.970	0.07
18	Ar	36	84.281	6.37	34	Se	82	8.820	2.30	50	Sn	114	0.660	0.10
18	Ar	38	15.695	5.64	35	Br	79	50.650	2.24	50	Sn	115	0.340	0.38
18	Ar	40	0.024	2.83	35	Br	81	49.350	2.23	50	Sn	116	14.540	1.25
19	K	39	93.133	5.10	36	Kr	78	0.365	0.75	50	Sn	117	7.680	0.97
19	K (*)	40	0.146	2.30	36	Kr	80	2.344	1.55	50	Sn	118	24.220	1.47
19	K	41	6.721	3.96	36	Kr	82	11.686	2.25	50	Sn	119	8.590	1.02
20	Ca	40	96.941	6.35	36	Kr	83	11.573	2.25	50	Sn	120	32.580	1.60
20	Ca	42	0.647	4.17	36	Kr	84	56.895	2.94	50	Sn	122	4.630	0.75
20	Ca	43	0.135	3.49	36	Kr	86	17.137	2.42	50	Sn	124	5.790	0.85
20	Ca	44	2.086	4.68	37	Rb	85	70.875	2.24	51	Sb	121	57.210	0.80
20	Ca	46	0.004	1.97	37	Rb (*)	87	29.125	1.86	51	Sb	123	42.790	0.67
20	Ca	48	0.187	3.64	38	Sr	84	0.563	0.64	52	Te	120	0.090	−0.85
21	Sc	45	100.000	3.20	38	Sr	86	9.916	1.89	52	Te	122	2.550	0.60
22	Ti	46	8.250	3.95	38	Sr	87	6.472	1.70	52	Te	123	0.890	0.14
22	Ti	47	7.440	3.91	38	Sr	88	83.049	2.81	52	Te	124	4.740	0.87
22	Ti	48	73.720	4.90	39	Y	89	100.000	2.27	52	Te	125	7.070	1.04
22	Ti	49	5.410	3.77	40	Zr	90	51.450	2.37	52	Te	126	18.840	1.47
22	Ti	50	5.180	3.75	40	Zr	91	11.220	1.70	52	Te	128	31.740	1.70
23	V	50	0.250	1.36	40	Zr	92	17.150	1.89	52	Te	130	34.080	1.73
23	V	51	99.750	3.96	40	Zr	94	17.380	1.89	53	I	127	100.000	1.55
					40	Zr	96	2.800	1.10					
54	Xe	124	0.127	−0.61	64	Gd	152	0.200	−1.55	74	W	180	0.120	−2.07
54	Xe	126	0.113	−0.66	64	Gd	154	2.180	−0.52	74	W	182	26.500	0.28
54	Xe	128	2.216	0.63	64	Gd	155	14.800	0.31	74	W	183	14.310	0.01
54	Xe	129	27.438	1.72	64	Gd	156	20.470	0.46	74	W	184	30.640	0.34
54	Xe	130	4.346	0.92	64	Gd	157	15.650	0.34	74	W	186	28.430	0.31
54	Xe	131	21.771	1.62	64	Gd	158	24.840	0.54	75	Re	185	35.707	−0.08
54	Xe	132	26.347	1.70	64	Gd	160	21.860	0.48	75	Re (*)	187	64.293	0.18
54	Xe	134	9.743	1.27	65	Tb	159	100.000	0.37	76	Os	184	0.020	−2.28
54	Xe	136	7.900	1.18	66	Dy	156	0.056	−2.09	76	Os	186	1.597	−0.38

Table B.1. continued.

Z	Elem.	A	fraction %	log ϵ	Z	Elem.	A	fraction %	log ϵ	Z	Elem.	A	fraction %	log ϵ
55	Cs	133	100.000	1.09	66	Dy	158	0.095	−1.86	76	Os	187	1.559	−0.40
56	Ba	130	0.110	−0.62	66	Dy	160	2.329	−0.47	76	Os	188	13.294	0.54
56	Ba	132	0.100	−0.67	66	Dy	161	18.889	0.44	76	Os	189	16.216	0.62
56	Ba	134	2.420	0.72	66	Dy	162	25.475	0.57	76	Os	190	26.368	0.83
56	Ba	135	6.590	1.15	66	Dy	163	24.896	0.56	76	Os	192	40.947	1.02
56	Ba	136	7.850	1.23	66	Dy	164	28.260	0.62	77	Ir	191	37.230	0.97
56	Ba	137	11.230	1.38	67	Ho	165	100.000	0.54	77	Ir	193	62.770	1.19
56	Ba	138	71.700	2.19	68	Er	162	0.139	−1.86	78	Pt (*)	190	0.012	−2.25
57	La (*)	138	0.092	−1.86	68	Er	164	1.601	−0.80	78	Pt	192	0.782	−0.43
57	La	139	99.908	1.17	68	Er	166	33.503	0.52	78	Pt	194	32.864	1.19
58	Ce	136	0.185	−1.09	68	Er	167	22.869	0.35	78	Pt	195	33.775	1.20
58	Ce	138	0.251	−0.96	68	Er	168	26.978	0.43	78	Pt	196	25.211	1.07
58	Ce	140	88.450	1.59	68	Er	170	14.910	0.17	78	Pt	198	7.356	0.54
58	Ce	142	11.114	0.69	69	Tm	169	100.000	0.16	79	Au	197	100.000	0.97
59	Pr	141	100.000	0.81	70	Yb	168	0.126	−1.99	80	Hg	196	0.150	−1.67
60	Nd	142	27.152	0.92	70	Yb	170	3.023	−0.61	80	Hg	198	10.040	0.16
60	Nd	143	12.174	0.57	70	Yb	171	14.216	0.07	80	Hg	199	16.940	0.38
60	Nd	144	23.798	0.86	70	Yb	172	21.754	0.25	80	Hg	200	23.140	0.52
60	Nd	145	8.293	0.40	70	Yb	173	16.098	0.12	80	Hg	201	13.170	0.28
60	Nd	146	17.189	0.72	70	Yb	174	31.896	0.42	80	Hg	202	29.740	0.63
60	Nd	148	5.756	0.24	70	Yb	176	12.887	0.02	80	Hg	204	6.820	−0.01
60	Nd	150	5.638	0.24	71	Lu	175	97.180	0.15	81	Tl	203	29.515	0.45
62	Sm	144	3.066	−0.50	71	Lu (*)	176	2.820	−1.38	81	Tl	205	70.485	0.83
62	Sm (*)	147	15.384	0.20	72	Hf	174	0.161	−1.88	82	Pb	204	1.400	0.16
62	Sm	148	11.199	0.07	72	Hf	176	5.240	−0.37	82	Pb	206	24.100	1.40
62	Sm	149	13.758	0.15	72	Hf	177	18.580	0.18	82	Pb	207	22.100	1.36
62	Sm	150	7.337	−0.12	72	Hf	178	27.280	0.35	82	Pb	208	52.400	1.73
62	Sm	152	26.619	0.44	72	Hf	179	13.630	0.05	83	Bi	209	100.000	0.65
62	Sm	154	22.637	0.37	72	Hf	180	35.120	0.46	90	Th (*)	232	100.000	0.19
63	Eu	151	47.810	0.26	73	Ta	180	0.012	−4.00	92	U (*)	234	0.002	−4.73
63	Eu	153	52.190	0.30	73	Ta	181	99.988	−0.07	92	U (*)	235	24.167	−0.65
										92	U (*)	238	75.831	−0.16

Notes. The proto-solar abundances account for atomic diffusion of 0.07 dex for He and 0.064 dex for all heavier elements as predicted by Vinyoles et al. (2017), as well as radio-active decay. The elements for which no solar abundance is available are based on CI chondrites adjusted for the trend in condensation temperature between the Sun and meteories (Sect. 3.3). (*)Long-lived radio-active element.